Resonance Ionization Spectroscopy of Europium: The First Application of the PISA at ISOLDE-RILIS

von

Katerina Chrysalidis

Masterarbeit in Physik
vorgelegt dem Fachbereich Physik, Mathematik und Informatik (FB 08)
der Johannes Gutenberg-Universität Mainz
am 08. September 2016

1. Gutachter: Prof. Dr. Klaus Wendt
2. Gutachter: Dr. Valentin Fedosseev

Ich versichere, dass ich die Arbeit selbstständig verfasst und keine anderen als die angegebenen Quellen und Hilfsmittel benutzt, sowie Zitate kenntlich gemacht habe.

Mainz, den 08. September 2016

Katerina Chrysalidis
AG LARISSA
Institut für Physik
Staudingerweg 7
Johannes Gutenberg-Universität D-55099 Mainz
katerina.chrysalidis@cern.ch

Abstract

The following work has been carried out at the radioactive ion beam facility ISOLDE at CERN. A compact atomic beam unit named PISA (Photo Ionization Spectroscopy Apparatus) has been implemented as a recent addition to the laboratory of the Resonance Ionization Laser Ion Source (RILIS). The scope of this thesis work was to demonstrate different applications of the PISA, using the existing and highly developed laser setup of the RILIS installation.
In a demonstration of the suitability of PISA for ionization scheme development, a new ionization scheme for Europium has been developed. This resulted in the observation of several new autoionizing states and Rydberg series. Through the analysis of the observed Rydberg resonances a refined value of $45734.33(3)(3)\,\mathrm{cm}^{-1}$ for the ionization potential of the europium atom has been determined. In addition this thesis reports on the feasibility of the use of the PISA as a RILIS performance monitoring device during laser ion source operations.
Finally the present work outlines future applications and upgrades of the PISA. Several modifications are recommended which will help to further improve the performance, practicality and versatility of the PISA.

Contents

List of Tables

List of Figures

1 Introduction

In the scope of this work a new device, the Photo-Ionization Spectroscopy Apparatus (PISA) was added to the laboratory of the Resonance Ionization Laser Ion Source (RILIS) at the radioactive ion beam facility ISOLDE (Isotope Separator On-Line DEvice) at CERN[1]. The main goal was to enhance the productivity and scope for the development of new multi-step laser resonance ionization schemes and to provide additional means of laser performance monitoring during the setup and operation of the RILIS.

There are several different types of radioactive ion beam (RIB) facilities worldwide. One of them is the ISOL (Isotope Separator On-Line) approach. The goal to provide access to a wide range of radioisotopes, even those with lifetimes as short as several ms, is achieved through the coupling of the isotope production process with an immediate extraction and delivery to an experiment in the form of an accelerated ion beam. There are two main types of such ISOL facilities: Thick-target facilities, like ISOLDE, where a driver beam of typically 1 GeV protons is incident on the target, producing radioactive species via fission, fragmentation or spallation reactions. The products are predominantly formed as neutral atoms and are ionized separately in an attached ion source for subsequent extraction. A somewhat alternative method is the thin-target/gas-catcher facility, called IGISOL (Ion Guide Isotope Separator On-Line). In these facilities the usually less energetic driver beam is incident on a thin target, the reaction products are emitted due to the reaction recoil and are stopped in a gas cell filled with helium or argon. Here the ionic charge decreases to $+1$, so that an extraction becomes possible.
At ISOLDE, the principal ionization method in use is step-wise resonance photo-ionization. As such, the Resonance Ionization Laser Ion Source (RILIS) has become the most intensively used and versatile ion source of its type, producing e.g. more than 70% of the ion beams in 2015. The resonance ionization technique makes use of the uniqueness of ionization schemes for different elements, exploiting the specific atomic structure of each chemical element and selectively ionizing the one of interest. So far, radioactive isotopes of 36 different elements have been ionized with the RILIS. In some cases, if the spectral linewidth of the used laser radiation is sufficiently narrow, it is possible for the RILIS to resolve the hyperfine structure or isotope shifts of an atomic transition in the ionization scheme. This provides the opportunity to directly measure nuclear properties such as spins and moments and even permits for isomer separation. The laser system of the RILIS has been developed over many years, starting 1992 [SFK+92]. Since then many new optical excitation schemes have been developed, not only at CERN but also in other groups, e.g. the LARISSA-group (LAser Resonance Ionization for Spectroscopy

[1] Conseil Européen pour la Recherche Nucléaire (English: European Organization for Nuclear Research)

and Selective Applications) in Mainz or at ISAC, TRIUMF, Vancouver ([RDH+13]).
In order to keep up with the demands of the physics users for different beams, ionization scheme development is continuously required to ensure optimal performance of the RILIS for each specific experiment. Typically this begins with an extensive literature search and study concerning any available information on atomic spectroscopy. Despite the availability of conclusive information, the development of an ionization scheme always requires an experimental investigation for identification and comparison of possible ionization schemes by means of dedicated resonance ionization spectroscopy studies. Scheme development can either take place off-line, for example at the LARIS (LAser Resonance Ionization Spectroscopy) laboratory ([MBF+10]) or the off-line mass separator at CERN, with the disadvantage that the lasers used for these experiments are not the same ones as in the RILIS laboratory. Another possibility for scheme development is therefore to do it on-line. A current disadvantage is that during on-line operation when protons are readily available at CERN, it can be hard to find the time for extensive scheme development, as ISOLDE is working to capacity. The introduction of the PISA gives the possibility to use the RILIS laser setup for initial scheme development, either during the ISOLDE shut down period or even parasitically during/in-between different experiments over the year. The first steps of scheme development can help to determine new energy levels and identify autoionizing states. The final scheme development will have to take place using one of the ISOLDE targets. Extensive laser scans will no longer be necessary due to the prior scheme development, shortening the time needed to finalize the new scheme considerably.

Chemical elements which belong to the group of the lanthanides have been the first to introduce the RILIS technique but still today have not been fully explored concerning their precise ionization potential and most useful ionization schemes. Their atomic structure is very complex, as a multitude of open shells offer many possibilities for complicated coupling. One interest lies in the heavy ions in the $Z = 64$ region. Lanthanides with these masses have been extensively studied in order to precisely determine their isotope shifts, mean square charge radii and the shape transition of the nucleus in this region ([Neu85, BNN88, Ott89]).
As all lanthanides have very low ionization potentials (IP) they are easily surface ionized, so that the development for resonance ionization was initially not pursued. Nevertheless, just during the last years, lanthanides have come again into focus, as there are many applications requiring ultimate elemental selectivity as provided only by the RILIS. One example for their use is the ECHo-project. Its name stands for Electron Capture in Holmium. This experiment aims to measure the mass of the electron neutrino from the energy spectrum following electron capture of the isotope ^{163}Ho using metallic magnetic calorimeters [GBD+14]. The field of quantum computing also makes use of crystals, doped with different lanthanides. These are used for quantum memory or quantum computing ([SKZ+16, LTG+12]). The lifetimes of the investigated levels in some of these elements are ideal for using them as memory for qubits. These applications require very pure beams in order to generate the best possible results. For this reason the surface ionized beams are no longer sufficient and the scheme development for resonance ionization has become very important.

Another field of Resonance Ionization Spectroscopy (RIS) studies in lanthanides is a very fundamental one required as basis for application at RIB facilities. Determining the most basic atomic property, i.e. the ionization potential, is needed and made possible using RIS. For this purpose Rydberg levels can be excited using an appropriate scheme which offers the best chance to precisely determine the IP. They posses a highly excited valence electron with high principal quantum number and large orbit. Correspondingly their structure is quite similar to the atomic system of hydrogen as best understood and quantitatively accessible atomic structure. Assuming that the Rydberg atom obeys similar rules, investigating the IP with theoretical and numerical tools derived from the description of the hydrogen becomes possible.

2 The ISOLDE isotope separator facility

This chapter outlines the two main experimental facilities where the measurements for this work were performed. It will give an overview over the general setup and sketch the different uses. Section 2.1 is mainly based on the PhD theses by B.A. Marsh [MBF07] and U. Köster [KR99]. Further information about ISOLDE and a more thorough description of the RILIS can be found in [Mar13] and [RGF+16].

2.1 Overview

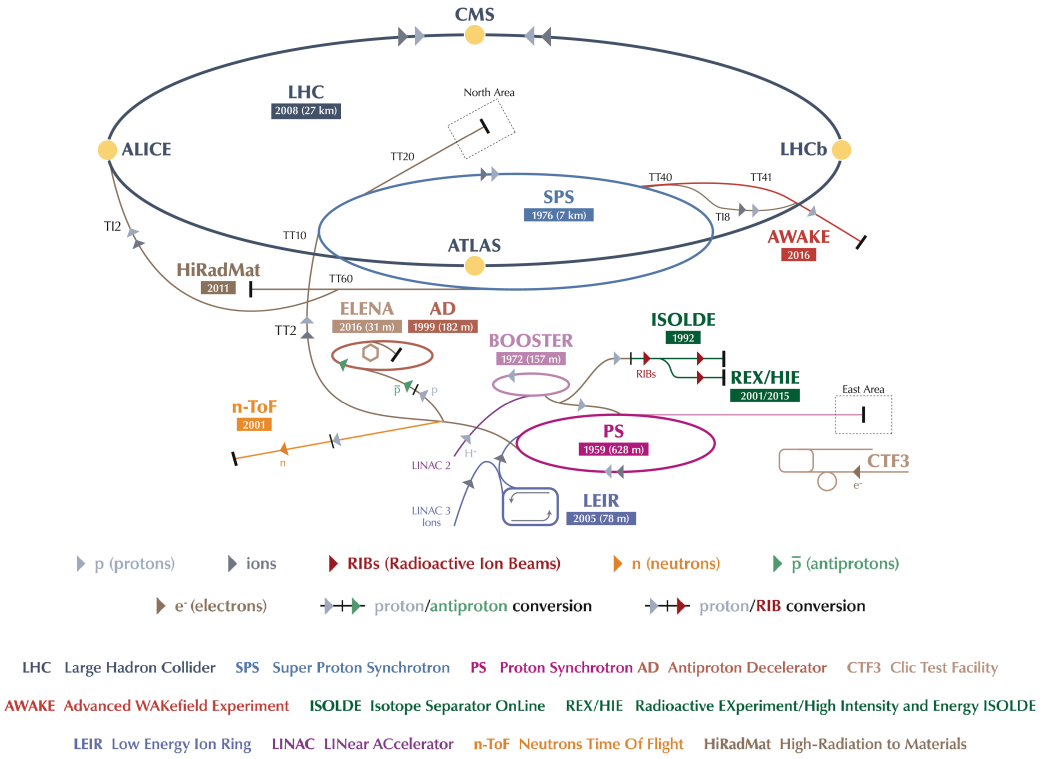

Figure 2.1: *Overview of the accelerator complex at CERN [DM16]. ISOLDE (green) is situated at the Booster (pink).*

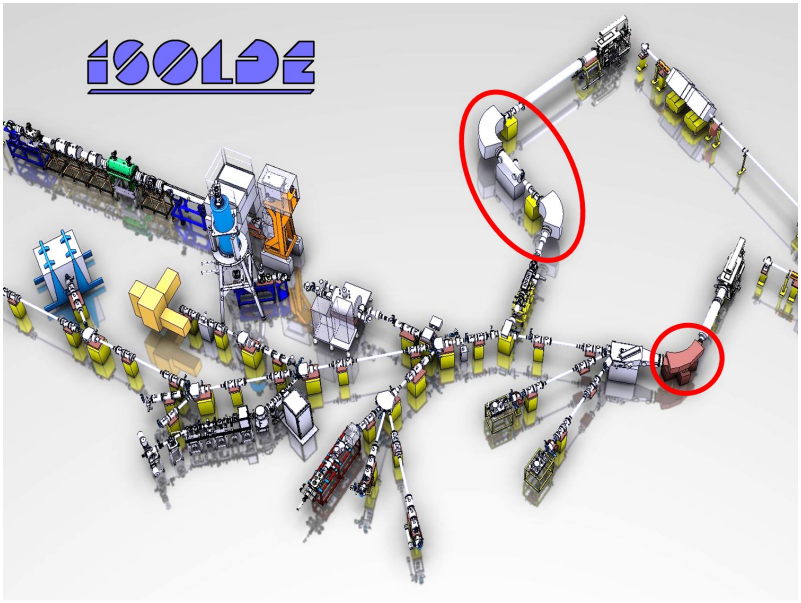

Figure 2.2: *The general layout of the ISOLDE separators (circled in red) and the beam lines leading to various fixed experiments. Towards the left the beam lines go further into the HIE-ISOLDE setup, where post acceleration of the beam takes place in order to get higher beam quality. The drawing has been downloaded from the ISOLDE web page and slightly modified [iso]*

The radioactive beam facility ISOLDE[1] at CERN, Geneva (Switzerland) is situated at the PS Booster (PSB). The PSB has a diameter of $50\,\mathrm{m}$. Protons with an initial energy of $50\,\mathrm{MeV}$ are accelerated to energies of 1.0 or $1.4\,\mathrm{GeV}$. They are released in pulses of $2.4\,\mu\mathrm{s}$ length with a repetition rate of $1.2\,\mathrm{s}$ and an intensity of up to 3×10^{13} protons/pulse. Exotic radioisotopes are produced at ISOLDE either by fission, fragmentation or spallation processes in a thick target which is irradiated by the proton beam. The production rate is proportional to the beam flux of the proton beam and also to the number of atoms in the target that are being hit by it. The ISOLDE target unit consists mainly of the target container, filled with the target material which depends on the desired production of elements and their isotopes. Connected to this is a transfer line and the ion source. If needed a mass marker with either a non calibrated sample (for example for beam tuning) or a calibrated sample of a well-defined amount of stable isotopes can be attached to the back of the transfer line. All elements are resistively heated in order to release atoms in vapor form. Once the atoms have been ionized in the ion source (either by surface, laser or plasma ionization), the ions are extracted with an extraction electrode and guided through mass separator systems after which the ion beam is further directed to one of the many experimental setups in the ISOLDE hall.

ISOLDE can offer several different beams at the same time. This is made possible by

[1] **I**sotope **S**eparator **O**n-**L**ine **DE**vice

two separator setups which both have their own target. One of the separators is called GPS (**G**eneral **P**urpose **S**eparator) and involves only one magnet with a bending angle of $70°$. An electrostatic switch yard is situated behind the separation magnet, allowing for the simultaneous extraction of three mass separated beams. The other so called HRS (**H**igh **R**esolution **S**eparator) consists of a $90°$ bending magnet and a $60°$ magnet. It offers a mass resolution of more than 5000.
There are 'stationary' and 'traveling' installations, meaning that some experiments have fixed beam lines and positions in the hall while others are only attached to a beamline for the period of the experiment and have to be taken away afterwards. There are installations for nuclear and laser spectroscopy, mass measurements, solid state and surface studies. There are also some biophysics experiments where sample collections for further e.g. medical applications are taken. An overview of the ISOLDE separators and some of the fixed installations can be seen in Figure 2.2.

2.2 RILIS

The Resonance Ionization Laser Ion Source (RILIS) is the preferred ion source used at ISOLDE. It is based on the principle of laser resonance ionization (see section 3.3) and is typically used in combination with the hot cavity surface ion source of the ISOLDE target/ion-source assembly. The main advantages are that elements with high ionization potentials as well as elements with low volatility that are hard to ionize with other ion sources are ionized efficiently and, crucially, with an unparalleled degree of element selectivity. Correspondingly it offers a reduction of isobaric contamination, combined with the possibility of beam diagnostics (laser on/off tests e.g. for yield checks). Striking advantage is the fact, that the main set up components, i.e. the lasers, are located several meters away from the target and the hostile (radioactive) environment where it is situated.
The RILIS laser laboratory is located in a closed laser protection area, realized by a Faraday cage above the junction of the beam lines emerging from the HRS and GPS in the ISOLDE hall. There are two optical paths for the laser light from the RILIS into the ion sources located $18\,\mathrm{m}$ (GPS) and $23\,\mathrm{m}$ (HRS) away.
The laser setup (see Figure 2.3) consists of three tunable dye lasers, two CREDO from Sirah Lasertechnik GmbH and one MSS from DMK Laser Microsystems, three solid state Ti:Sa lasers, designed in Mainz in the LARISSA group, two Photonics Industries DM-60 pump lasers, one pump laser from Edgewave GmbH and a Coherent/Lumera Blaze laser for non resonant ionization. The high power pump lasers are all frequency doubled Nd:YAG lasers with a wavelength of $532\,\mathrm{nm}$, with the Edgewave laser offering an additional beam with $355\,\mathrm{nm}$ light, the third harmonic of the fundamental laser wavelength. The repetition rate of all lasers is $10\,\mathrm{kHz}$ as required for efficient laser-atom interaction in the source as well as for providing the best trade of between the pulse energy and the average power. The pulse duration for the Edgewave is around $10\,\mathrm{ns}$ and for the Photonics around $150\,\mathrm{ns}$. Both lasers have been specially chosen to match the specific requirements of the tunable lasers which they pump. The pulse length of the Lumera

Blaze is 17 ns.
The dye lasers have a linewidth of around 9 GHz with the MSS offering the option of a reduced linewidth of 0.7 GHz. The high standard linewidth offers good efficiency of excitaion of atoms with broad hyperfine structures and also a reduced sensitivity to isotope shifts. This leads to an improved ion current stability should small drifts or wavelength fluctuations occur. The dye lasers can be pumped either with the 532 nm light or with the 355 nm UV light. In combination with second and third harmonic generation a wavelength range of 210 to 950 nm can be achieved. A list with the most commonly used dyes and their wavelength ranges can be found in Table 5.2.

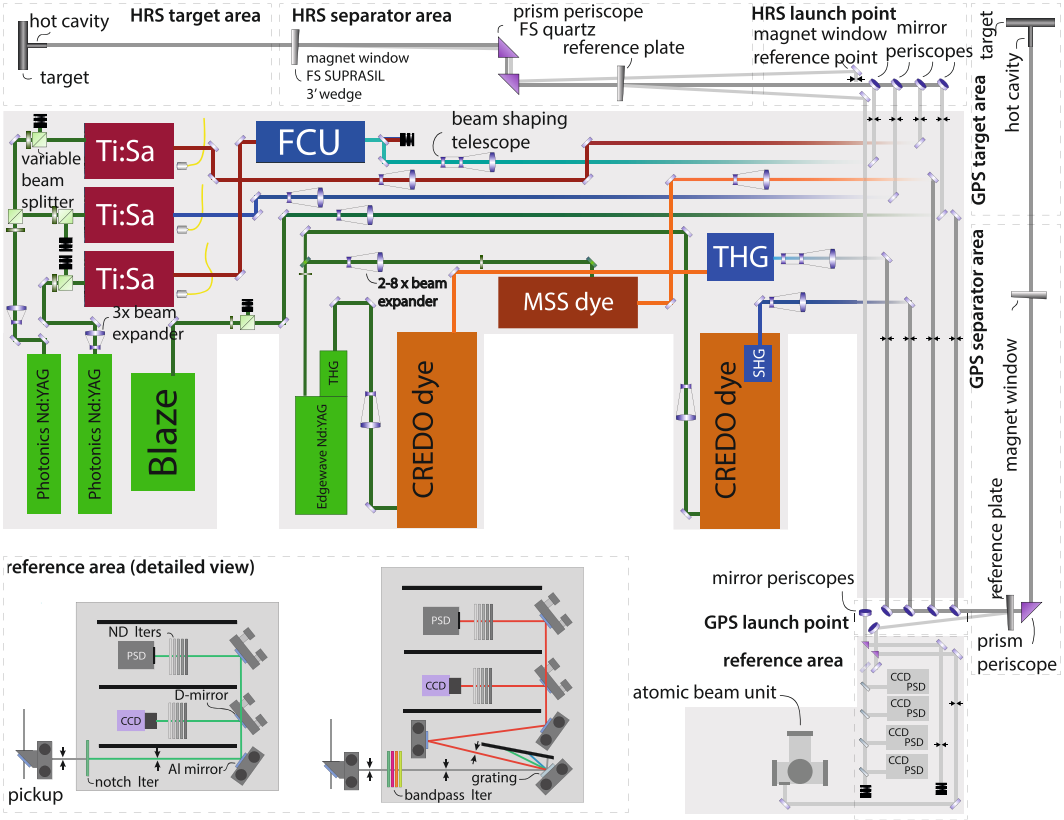

Figure 2.3: *The drawing shows all the lasers that are currently available in RILIS. The beam paths to the separators and their launch areas are schematically shown as well as the reference plates and the setup of the reference area with the PISA (section 4.1). Image taken from [RGF+16] and adjusted*

The three Ti:Sa lasers have a Z-cavity design, two of them were developed at CERN by S. Rothe [RWN12] based on the Mainz design. A scheme of this cavity design is depicted in Figure 2.4 aside the grating Ti:Sa design. The possibility to insert a second etalon into the Z-cavities exists so that the linewidth can be reduced from the usual 5 GHz to around 0.8 GHz. This can be used for in-source laser spectroscopy where a high resolu-

tion is needed or in case of need of higher selectivity (e.g. isomer separation). The third Ti:Sa is tunable via a grating which acts as the end mirror/high-reflector of the cavity. The design is similar to the Z-cavities and was made in Mainz by P. Naubereit [Nau14]. The fundamental wavelength range offered by the Ti:Sa crystal lasers is $\sim 690 - 950\,\mathrm{nm}$ (depending on the optics used). It may be frequency doubled, tripled or quadrupled, generating wavelengths as low as $210\,\mathrm{nm}$.

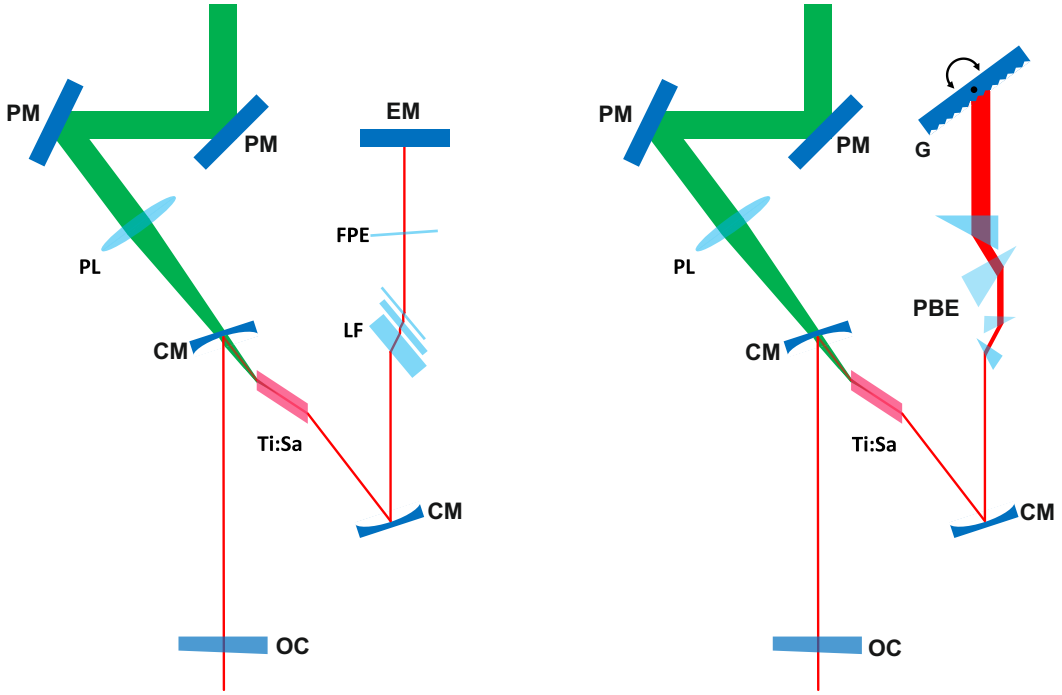

Figure 2.4: *The two different Ti:Sa designs are depicted schematically. On the left one can see the Z-cavity design, consisting of the pump mirrors (PM), a lens (PL) for focussing the pump beam (green) into the Ti:Sa crystal through the back of the concave mirror (CM) building the cavity together with the end mirror (EM) and the outcoupler (OC). Additionally the frequency selective elements are depicted, namely the Lyot filter (LF) and the Fabry-Perot etalon (FPE). The grating Ti:Sa cavity shows a similar design but the FPE and LF are replaced by a prism beam expander (PBE) and the EM is replaced by a turnable grating (G). (Drawings from [Nau14], slightly adjusted)*

This dual-RILIS system (a complete set of dye and Ti:Sa lasers) is worldwide unique and offers several advantages compared to a single dye or Ti:Sa system:

- spectral coverage with wavelengths from $210 - 950\,\mathrm{nm}$
- possibility to choose the laser which is suited best to a desired setup

- operation of dye and Ti:Sa in parallel to compare broadband and narrow linewidth operation
- possibility to perform laser setup and operation simultaneously to enable fast switching between different ionization schemes

The synchronization of the pulses of the individual lasers can be adjusted by changing the timing of the pump lasers. For this purpose they are connected to a Quantum Composers 9530 pulse generator. As the dye lasers are all pumped by the same laser sometimes delay lines for the laser beams are required in order to correct for minor timing differences in the ns range. The wavelengths can be stabilized using the software developed by R.E. Rossel [RRWR11].

The RILIS laser beam reference area

The PISA was first installed in the RILIS in October 2015. At that time the reference area was redesigned to allow space for the installation of the PISA [RGF+16]. The layout of the tables for the lasers (see Figure 2.3) allowed for the beam unit to be installed right next to the reference area.
When the laser beams are sent down to the laser ion source, they are intercepted half way down-stream by wedged fused silica plates at approximately normal incidence. Two reflections of around $4\,\%$ of the original power are sent back into the laser room, giving a reference which is essential as access to the target or separator areas during the on-line period is impossible because of the high radiation doses. There are two reflected beams generated by each laser beam coming back. One of these two beams is sent onto two broadband mirrors, reflecting the light and guiding it onto an iris. This iris acts as a specific reference point, indicating where overlap and size of the reference beams ideally mimic the beams going into the ion source. The position of the iris is set up roughly by overlapping the light emitted by the hot cavity and the laser beams on the launch mirrors. Once the overlap is given, a theodolite is used in order to get a visible beam into the ion source. Other beams are then overlapped with the first visible beam and the ion signal is optimized. Once the optimal ion signal is produced, the iris position is fixed to its final position.
A right-angle prism intercepts the second of the two reference beams and sends it to a further adjustment setup which consists of a wedged fused silica plate, a grating, two mirrors, a camera and a PSD (**P**osition **S**ensitive **D**evice). The plate once again generates two reflections (from the back and the front), which are directed towards the grating. The orders n of the grating and the angles ϕ_n with which they are reflected are depending on the wavelength λ, the grating constant d and the angle ψ with which the light is incident on the grating:

$$n \cdot \lambda = d \cdot (\sin \phi_n + \sin \psi) \tag{2.1}$$

This means that the 0^{th} order is reflected under the same angle independent of the wavelength of the light in contrast to the higher orders for which different wavelengths are

reflected under different angles. Using the first or second order reflection of the beam of interest the individual laser beams can be guided onto a mirror which reflects them onto a mirror, cut in half. One of the beams is directed onto a PSD, while the other one is reflected on the lower part of the mirror into a camera (see Figure 2.5). The PSD is connected to a stabilization unit which controls a mirror mount with piezo motors. These mounts are used in the so called 'launch area' where the full power beams are sent down to the ion source. This stabilization system, which is a commercial unit made by MRC Systems GmBH, provides 2-D stabilization of the reference beams at the reference area, ensuring that the laser beam position at the ion source remains fixed at the pre-defined optimum location. The camera is used to monitor the size and shape of the beam.

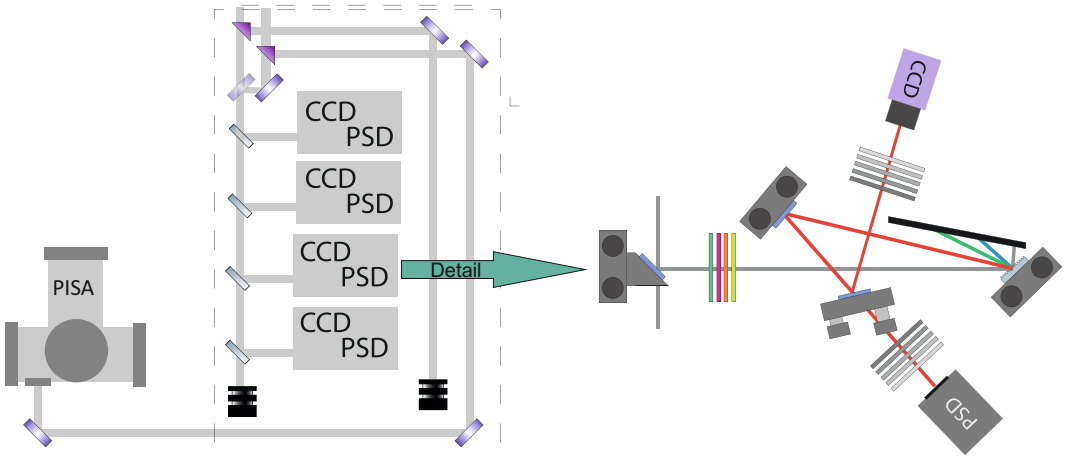

Figure 2.5: *The left side shows the general outline of the reference area with the PISA close up. The right side shows a sketch of the most commonly used layout of the reference area for the beam monitoring as described in the text above. (Image created with files provided by S. Rothe)*

3 Theoretical background for laser-atom interaction and laser resonance ionization

This chapter gives an overview over the basic theoretical concepts that are relevant for this thesis. Starting with the hydrogen atom, i.e. the most simple one electron atomic system, more complicated atomic systems and their interaction with light will be explained. An introduction into resonance ionization spectroscopy will also be given. A more detailed discussion is given in the deployed literature, please see: [Dem05], [Dem07], [Let87], [Con98], [Mes10].

3.1 Atomic structure

3.1.1 Hydrogen atom

In order to calculate the discrete energy levels of the hydrogen atom it is necessary to solve the time independent Schrödinger equation

$$H\left|\Psi\right\rangle = E\left|\Psi\right\rangle \tag{3.1}$$

for a single electron in the Coulomb-potential of the proton. The Schrödinger equation yields

$$-\frac{\hbar^2}{2m_e}\Delta_e\psi - \frac{\hbar^2}{2m_p}\Delta_p\psi - \frac{Ze^2}{4\pi\epsilon_0 r}\psi = E\psi(\boldsymbol{r}_e, \boldsymbol{r}_p) \tag{3.2}$$

with: m_e, m_p mass of the electron/proton, charge $q = Ze$, $\boldsymbol{r}_{e,p}$ radius vector of electron/proton, $\Delta_{e,p}$ Laplace operator with respect to $\boldsymbol{r}_{e,p}$. One can choose polar coordinates (r, θ, ϕ) to solve this radially symmetric problem. The use of the reduced mass μ sets the center of gravity to the point of origin of the system and the Hamilton operator becomes:

$$H = -\frac{\hbar^2}{2\mu}\Delta + V_C(r) \quad \text{where} \quad \mu = \frac{m_e m_p}{m_e + m_p} \quad \text{and} \quad V_C(r) = -\frac{e^2}{4\pi\epsilon_0 r} \tag{3.3}$$

Introducing the Laplace operator in the polar coordinates one obtains the Schrödinger equation in the following form:

$$\left\{\frac{1}{r^2}\left[\frac{\partial}{\partial r}\left(r^2\frac{\partial}{\partial r}\right)+\frac{1}{\sin\theta}\frac{\partial}{\partial\theta}\left(\sin\theta\frac{\partial}{\partial\theta}\right)+\frac{1}{\sin^2\theta}\frac{\partial^2}{\partial\phi^2}\right]\right\}\Psi(r,\theta,\phi) = -\frac{2\mu}{\hbar^2}\left\{E-V_C(r)\right\}\Psi(r,\theta,\phi) \tag{3.4}$$

As the potential is spherically symmetric, the wavefunction can be separated into a radial part R_{ln} and an angular part Y_{lm}:

$$\Psi_{nlm}(r,\theta,\phi) = R_{ln}(r)Y_{lm}(\theta,\phi) \tag{3.5}$$

$n \in \mathbb{N}$ is the principal quantum number, l is the orbital angular momentum ($0 < l < n-1$) and m is the magnetic quantum number ($-l < m < l$). l and m can take on a number of different values for a definite n but still lead to the same energy (see Equation 3.7), corresponding to a n^2 degeneracy of the energy levels. The spherical harmonics $Y_{lm}(r)$ can be solved with the help of the associated Legendre polynomials. Substituting $R_{ln}(r)$ with $u_{nl}(r)/r$ one gains the expression

$$\frac{\mathrm{d}^2u_n(r)}{\mathrm{d}r^2}+\frac{2\mu}{\hbar^2}\left[E_n+\frac{e^2}{4\pi\epsilon_0 r}-\frac{\hbar^2 l(l+1)}{2\mu r^2}\right]u_n(r)=0 \tag{3.6}$$

This gives the energy eigenvalues for $u_n(r)$

$$E_n = -\frac{\mu e^2}{2\hbar^2(4\pi\epsilon_0)^2n^2} = -\frac{\mu e^2}{8\epsilon_0^2h^2} = -R_\mu\frac{1}{n^2} \tag{3.7}$$

where R_μ is the (mass reduced) Rydberg constant. If one defines the ground state of an atom as its point of zero energy, then the ionization potential can be defined as the convergence of the states of the principal quantum number for $n \to \infty$, so that

$$E_{IP} = E_n + \frac{R_\mu}{n^2}. \tag{3.8}$$

3.1.2 Fine structure splitting

The fine structure describes the removal of the energy level degeneracy for same n. Due to relativistic effects and the coupling of electron spin and orbital momentum a splitting in the energy levels is observed, so that discrete levels can be spectroscopically resolved. The correction terms can be obtained using perturbation theory, leading to additional terms in the Hamiltonian:

$$H = H_0 + H_{rel} + H_{ls} + H_D \tag{3.9}$$

H_{rel} takes into account the relativistic treatment of the electron inside the proton's Coulomb potential. With $E = \sqrt{p_e^2c^2 + m_e^2c^4}$ (p_e: electron momentum, c: speed of light), the electron gains in mass and therefore in kinetic energy.

H_D is called the Darwin-term. It only affects the s-orbit and changes the effective potential at the nucleus. It takes into account quantum fluctuations, which make it impossible to determine the electron position more precisely than $\lambda_{compton} = \hbar/(m_e c)$. H_{ls} corrects for the spin-orbit coupling. It takes into account the magnetic moments of the electron due to the coupling of the spin s with the orbital angular momentum l. The magnetic spin moment of the electron has two discrete spatial orientations. This causes an additional energy, where spin and orbital angular momentum are coupled, giving the total angular momentum $\boldsymbol{j} = \boldsymbol{l} + \boldsymbol{s}$ (with $|l - s| \leq j \leq l + s$):

$$\Delta E \approx \frac{\mu_0 Z e^2}{4\pi m_e^2 r^3}(\boldsymbol{l} \cdot \boldsymbol{s}) \propto \frac{\hbar^2}{2}\left[j(j+1) - l(l+1) - s(s+1)\right] \tag{3.10}$$

With some further calculations which take into account the time-averaged value of r related to the probability of finding the electron at the location r and including the hydrogen wave functions, one finally obtains the total energy

$$E_{nj} = E_n \left[1 + \frac{Z^2\alpha^2}{n}\left(\frac{1}{j+1/2} - \frac{3}{4n}\right)\right] \tag{3.11}$$

with Sommerfeld's fine structure constant $\alpha = \frac{e^2}{4\pi\epsilon_0\hbar c} \approx \frac{1}{137}$.

3.1.3 Hyperfine structure and isotope shift

The hyperfine structure takes into account the specific nucleus and its resulting interaction with the electrons. The nucleus with spin $\boldsymbol{I}$ has a nuclear magnetic moment μ_K, which interacts with the magnetic field $\boldsymbol{B}_j$ which is produced by the electrons at the nucleus . This leads to a splitting of the energy levels into $(2F + 1)$ hyperfine components. $\boldsymbol{F}$ is the total angular momentum which is the sum of the total angular momentum $\boldsymbol{j}$ and the nuclear spin I. The additional energy of this hyperfine structure component is

$$\Delta E_{HFS} = \frac{A}{2}[F(F+1) - j(j+1) - I(I+1)] \tag{3.12}$$

with the hyperfine structure constant $A = g_N \mu_K B_j / \sqrt{j(j+1)}$ and the nuclear g-factor g_N. The selection rule is $|I - J| \leq F \geq I + J$ where a transition is only possible if ΔF is ± 1 or 0.
The magnitude of the hyperfine structure splitting is strongly dependent on the atomic configurations and is typically several orders-of-magnitude smaller than the fine structure splitting, as demonstrated by Table 3.1.

	cm^{-1}	eV	GHz
Fine structure	$1 - 1000$	$10^{-4} - 10^{-1}$	$10 - 10000$
Hyperfine structure	$10^{-3} - 1$	$10^{-7} - 10^{-4}$	$0.01 - 10$

Table 3.1: *Scale of the fine and the hyperfine structure*

Figure 3.1 shows the level scheme of the hydrogen atom in order to give a better understanding of the complete atomic structure in general. The structure gets more complicated for heavier atoms. When considering those atoms the ground state properties of the nucleus change between two isotopes of the same element. Aside of variations in spin and moments, this is due to mass and volume effects, that influence the energy difference of the atomic levels by changing the reduced mass of the nucleus-electron system and the size or shape of the nucleus.

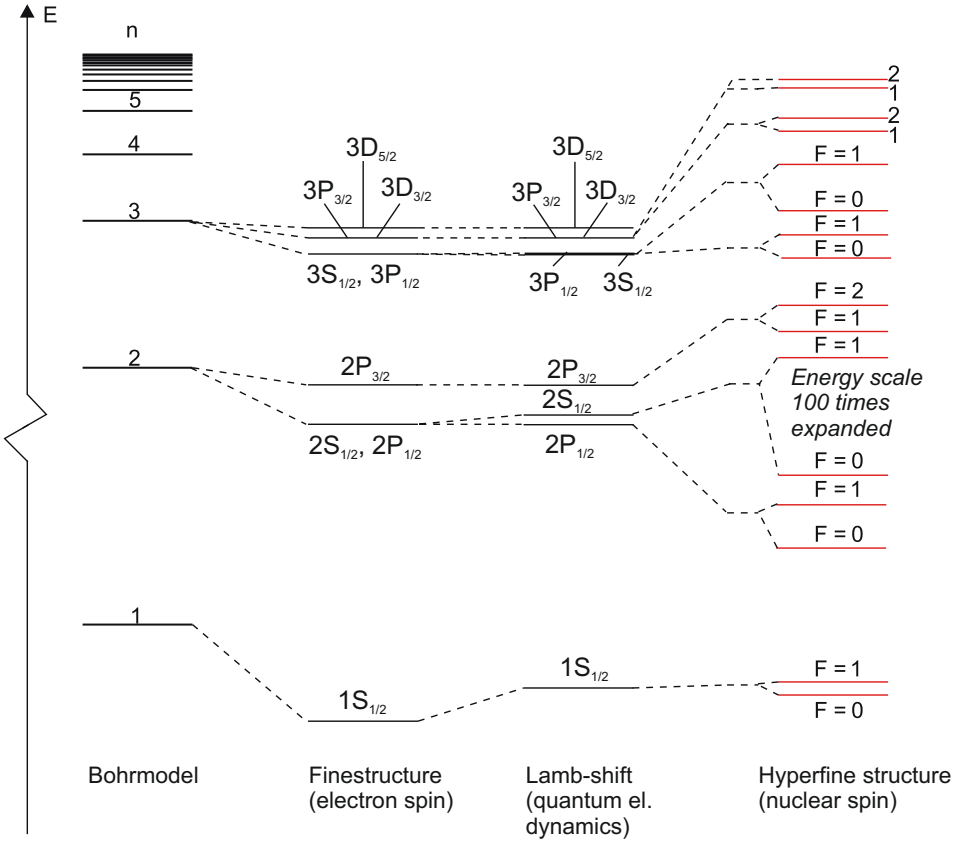

Figure 3.1: *The level scheme of the H atom is schematically shown with all interaction effects. The fine, hyperfine structure and the Lamb-shift are not drawn to scale as the splittings and shifts would be too small to depict [Dem05].*

3.1.4 Atoms with more than one electron

If an atom has more than one electron mutual electrostatic and magnetic interactions between the electrons arise. Additionally there is a new symmetry, which arises from two electrons being exchanged but indistinguishable. The simplest of such systems is the helium atom, in which two electrons interact. Many of the principles that can be deducted from this system also apply to more complex systems. One of these is the Pauli-principle, which states that the total wavefunction of a system with more than one electron is always antisymmetric with regard to the exchange of two electrons. Each state can only be described with a complete set of quantum numbers (n, l, m_l, m_s) and can only be occupied by one single electron. The orbital angular momenta and spins of the N electrons can couple to a total angular momentum $\vec{J}$. For most atoms LS-coupling occurs, where the orbital angular momenta $\vec{l_i}$ and the spins $\vec{s_i}$ of the single electrons couple to a total orbital angular momentum $\vec{L} = \sum_{i=1}^{N} \vec{l_i}$ and a total spin $\vec{S} = \sum_{i=1}^{N} \vec{s_i}$, so that $\vec{J} = \vec{L} + \vec{S}$.
Alternatively the so called jj-coupling is observed in some atomic systems, where the orbital angular momentum $\vec{l_i}$ and spin $\vec{s_i}$ of one single electron couple to the total angular momentum $\vec{j_i}$ of that electron. These then couple to the total angular momentum $\vec{J} = \sum_{i=1}^{N} \vec{j_i}$ of the atom. This form of coupling predominantly appears in heavy atoms and for higher excited states, as the coupling between different electrons gets suppressed.

3.1.5 Rydberg atoms

This section is summarizing the more extensive chapter on Rydberg atoms and Rydberg spectroscopy by V.S. Letokhov [Let87] (p. 65 ff).
Highly excited atoms often have one electron moving in an enlarged orbit far away from the nucleus and from the other electrons' orbits. Most atomic characteristics exhibit a strong and increasing dependency on the principal quantum number n. Their atomic collision cross section for example grows with n^4, their radiative lifetime with n^3 while the binding energy is reduced with $1/n^2$ and the finestructure splitting with $1/n^3$. These Rydberg atoms can reach very large diameters in the range of µm. Due to the reduction in electron binding energy and the increase in collision cross section it becomes quite easy to ionize the atom, either via collisional processes, via application of external electrical fields or just by black body radiation. This makes a spectroscopic study of these states rather easy through their identification via registration of the resulting positive ion or free electron. If ionization is achieved through the use of external electrical fields, the linear Stark coefficient, which can lead to a split in the energy spectrum, scales with a factor of n^2 and may have to be taken into account in the analysis in the Rydberg spectrum.
In a Rydberg atom the outer electron experiences the nucleus with the charge Z screened by $Z-1$ other electrons. This scenario is analogous to that of the hydrogen atom, where only a charge of $+e$ is present. A distinction between the Rydberg atom and the hydrogen atom is made by introducing the effective principal quantum number n^*. n^* comprises the quantum defect $\delta(n)$ and the energy can therefore be written as follows:

$$E_n = E_{IP} - \frac{R_\mu}{(n^*)^2} = E_{IP} - \frac{R_\mu}{(n - \delta(n))^2} \tag{3.13}$$

3.1.6 Quantum defect and perturbed Rydberg series

The quantum defect $\delta(n)$ as introduced in Equation 3.13 takes into account that the $Z-1$ electrons do not entirely screen the nucleus. The dependence of n is obvious, as for small n the distance to the nucleus is smaller and therefore the screening less complete. Correspondingly the quantum defect is not constant and therefore it is described by some orders of perturbation. W. Ritz proposed two possible expansions of the quantum defect [Rit03], one of which is as follows:

$$\begin{aligned} \delta(n) &= \delta(n) + \frac{\beta}{(n - \delta(n))^2} + \frac{\gamma}{(n - \delta(n))^4} + ... \\ &\approx \delta_0 + \frac{\beta}{(n - \delta_0)^2} + \frac{\gamma}{(n - \delta_0)^4} + ... \end{aligned} \tag{3.14}$$

In the approximation $\delta(n)$ has been substituted by a constant δ_0. The significance of this substitution is discussed in detail in [DS91]. It helps fitting experimental data, but undermines the significance of the theoretical values while decreasing the accuracy of the quantum defect method. A more accurate description, derived from quantum defect theory, is given in the paper by M.J. Seaton [Sea66] which has been taken up by J.-P. Connerade in [Con98] (p. 41).
Seaton claims in his paper, that the procedure which is usually used for determining E_{IP} (choose an initial estimate E^0_{IP}, calculate δ_0 and adjust E^0_{IP} until δ_0 shows a linear dependence on n) is in so far unsatisfactory, as it does not take into account the rapid increase of the error in $\delta(n)$ with growing n. He therefore proposes an alternative, iterative procedure which involves least-squares fitting of the experimental data resulting from a detailed quantum defect formalism. He derives the quantum defect to be as follows:

$$\delta(n) = \sum_{i=2}^{N} C_i \left(\frac{E_n - E_{start}}{R_\mu} \right)^{i-2} = \sum_{i=2}^{N} C_i \left(\frac{E_n - E_{IP} + R_\mu C_1}{R_\mu} \right)^{i-2} \tag{3.15}$$

Here E_{start} is the initially assumed value for the energy of the IP. For the final series limit one then gets:

$$E_{IP} = E_n + \frac{R_\mu}{(n - \delta(n))^2} = E_n + \frac{R_\mu}{\left[n - \sum_{i=2}^{N} C_i \left(\frac{E_n - E_{IP}}{R_\mu} C_1 \right)^{i-2} \right]^2} \tag{3.16}$$

It is easy to see, that Equation 3.16 cannot be simply solved for E_n. This would need to be done if ones wanted to implement a fitting function which can be used for the analysis of a data set. It would become necessary to first apply a fit to $\delta(n)$ and afterwards use

the obtained data to calculate E_{IP}. A propagation of errors would have to be taken into account, further complicating the procedure.
For the data evaluation in this work therefore only the simple Rydberg-Ritz formalism, as described in Equation 3.14, will be used. This gives the energy dependence on the principal quantum number n:

$$E_n = E_{IP} - \frac{R_\mu}{(n-\delta(n))^2} \approx E_{IP} - \frac{R_\mu}{\left[n - \delta_0 - \frac{\beta}{(n-\delta_0)^2}\right]^2} \tag{3.17}$$

There are further possibilities to correct for more effects, for example considering the Stark-effect. The linear Stark-effect is induced by an external electric field, such as an extraction electrode. The splitting grows proportional with n^2, but the electric field gradient in the special case of this work is too small to be significant. Additionally the laser light provides an electric (AC) field, so that for sufficiently high laser power the quadratic Stark-effect could take hold. Its splitting grows proportional with n^7, but it is not observed for the lasers in use.

If a Rydberg series shows perturbations, further corrections have to be taken into account. One of these is the correction described by U. Fano in [Fan61]. He considers a discrete perturbation level with energy E_ϕ to which the Rydberg states couple with a strength of $|V(E)|^2$. The quantum defect then becomes

$$\delta(n) \to \delta(n) - \frac{\Delta}{\pi} = \delta(n) - \frac{1}{\pi}\arctan\left(\frac{\pi|V(E)|^2}{E - E_\phi - F(E)}\right) \tag{3.18}$$

with the phase shift Δ. F represents a shift of the resonance position with respect to E_ϕ. If one defines the width of the coupling state with $\Gamma = 2\pi|V(E)|^2$ and further substitutes $E_P = E_\phi - F$ one can insert the obtained expressions into the Rydberg-Ritz formula (3.13):

$$E_n \approx E_{IP} - R_\mu \left[n - \left(\delta_0 + \frac{\delta_1}{(n-\delta_0)^2} - \frac{1}{\pi}\left(\frac{\Gamma/2}{E_{IP} - \frac{R_\mu}{(n-\delta_0)^2} - E_P}\right)\right)\right]^{-2} \tag{3.19}$$

3.2 Light-atom interaction

In order to build the foundation for the following section about resonance ionization spectroscopy, this section will give an overview of how atoms interact with photons.

3.2.1 Atomic transitions

The most fundamental theorem of physics, namely the conservation of energy, implies that the total energy of a system (here: atom-photon) must remain constant. The state of an atom can change either via emission or absorption of a photon. Due to the

conservation of energy this process can be easily described. In a two-level system with the states $|1\rangle$ and $|2\rangle$ with the according energies $E_1 < E_2$, this leads to the following three possibilities:

- **Absorption:** A photon with energy $h\nu$ is being absorbed by the atom, so that the electron goes from $|1\rangle$ into $|2\rangle$, where $E_2 = E_1 + h\nu$.
- **Spontaneous emission:** An atom spontaneously goes from $|2\rangle$ into $|1\rangle$ whereby it emits a photon of energy $E_2 - E_1$. The emission can occur in any direction.
- **Stimulated emission:** An external light field stimulates the emission of a photon, so that $|2\rangle \rightarrow |1\rangle$. The photon from the external field and the photon resulting from the emission have the same energy of $h\nu = E_2 - E_1$ and additionally the same direction of propagation.

The probability for the above mentioned processes are given by the Einstein coefficients A_{21} for the spontaneous and B_{21} for the stimulated emission. A_{21} does not depend on the radiation field w_ν, whereas B_{21} does. The absorption must be equal to the total emission while under stationary conditions the number densities $N_{1,2}$ are time independent and therefore

$$B_{12} w_\nu N_1 = (B_{21} w_\nu + A_{21}) N_2. \tag{3.20}$$

Assuming a thermal equilibrium the ratio of N_2/N_1 follows the Boltzmann distribution

$$\frac{N_2}{N_1} = \frac{g_2}{g_1} \mathrm{e}^{(E_1 - E_2)/kT} = \frac{g_2}{g_1} \mathrm{e}^{(-h\nu)/kT} \tag{3.21}$$

where $g_{1,2}$ is the statistical weight of a state with energy E and total angular momentum quantum number J. Using Planck's formula of the spectral energy density of the thermal radiation field

$$w_\nu = \frac{8\pi h\nu^3}{c^3} \frac{1}{\mathrm{e}^{(h\nu)/kT} - 1} \tag{3.22}$$

and inserting Equation 3.21 into 3.20 leads to

$$\begin{aligned} B_{21} &= \frac{g_1}{g_2} B_{12} \\ \text{and} \quad A_{21} &= \frac{8\pi h\nu^3}{c^3} B_{21} \end{aligned} \tag{3.23}$$

For a transition $E_2 \rightarrow E_1$ the wave functions $\psi_{1,2}$ of both states have to be taken into account. Therefore the transition dipole moment M_{21} is introduced and defined by

$$\boldsymbol{M}_{21} = e \int \psi_2^* \boldsymbol{r} \psi_1 \mathrm{d}\tau. \tag{3.24}$$

The M_{21} are also known as Matrix elements. If some of them are zero, the corresponding transitions cannot occur, they are forbidden. This helps to define selection rules for allowed transitions. In general the following apply:

$$\begin{aligned} &\Delta J = 0, \pm 1 \qquad J = 0 \rightarrow J = 0 \text{ is forbidden} \\ &\Delta m_J = 0, \pm 1 \qquad m_J = 0 \rightarrow m_J = 0 \text{ is forbidden if } \Delta J = 0 \end{aligned} \tag{3.25}$$

For the LS coupling $\Delta S = 0$, $\Delta L = 0, \pm 1$ and $\Delta l = \pm 1$ (for the transition electron) apply. The jj coupling obeys to $\Delta j = 0, \pm 1$ for one of the electrons and $\Delta j = 0$ for all the other electrons.
The parity π of the atomic system is preserved. This means that as one photon (negative parity) is absorbed, the parity of the final state needs to change in regard to the initial state, so $\pi_i = -\pi_f$.

3.2.2 Line shape and width

There are four main effects that affect the line shape and width[1]:

- **Natural linewidth**: It is called the natural linewidth, because it is not induced by any external effects and solely dependent on the lifetimes of the atomic states. It can be derived from Heisenberg's uncertainty principle for the energy, $\Delta E = h/(2\pi\tau)$, provided that the decay of the state follows a simple exponential.The corresponding broadening of the transition frequency is given by the spread of the transition frequency, so that

  $$\Delta\nu = \frac{1}{2\pi}\left(\frac{1}{\tau_1} + \frac{1}{\tau_2}\right). \tag{3.26}$$

  The lineshape has a Lorentzian profile and is centered around the frequency $\nu_0 = (E_2 - E_1)/h$:

  $$g(\nu) = \frac{\Delta\nu/2\pi}{(\nu - \nu_0)^2 + (\Delta\nu/2)^2} \tag{3.27}$$

- **Collision broadening:** Inelastic collisions result in transitions between atomic energy levels. Collision broadening is assumed to be negligible in the laser ion source at ISOLDE due to the insufficient vapor density. In gas cell laser ion sources it is often dominant though [RMK+12]. The energy shift is expanded simply by adding a term f_{col} which is the collision rate:

  $$\Delta\nu = \frac{1}{2\pi}\left(\frac{1}{\tau_1} + \frac{1}{\tau_2} + 2f_{col}\right) \tag{3.28}$$

- **Saturation broadening:** Once the saturation limit of populating a state is reached a homogeneous broadening takes place, building up a flat top profile on the line

[1] This section is mainly based on [ST07] and [Dem07].

shape. A detailed formalism which takes into account the energy density matrices of the different states is given in [KS48]. A slightly more simplified explanation is given in [Dem07], where the saturation broadening is specifically derived for a two level system. A more 'hands-on' explanation is given in [Rae10]:

$$I'(\nu) = \frac{S \cdot I(\nu)}{1 + S \cdot I(\nu)} \tag{3.29}$$

$I(\nu)$ is the spectral distribution without saturation broadening. S denotes the saturation parameter and is given with $S(\nu) = P(\nu)/\bar{R}$, with the pump rate $P(\nu)$ and the mean relaxation rate of the energetically higher state $\bar{R}$. The spectral resolution is therefore reduced if the laser power exceeds the saturation power for the transition. For determining the region in which saturation starts, the formula

$$W(P) = W_0 + m \cdot P + A\frac{P/P_0}{1 + P/P_0} \tag{3.30}$$

can be applied for fitting. W_0 denotes the background (surface ionization, non resonant ionization) and m the growth of the ionization volume because of the Gaussian mode profile of the laser. P_0 gives the saturation power, at which half of the maximal transition rate A via resonant ionization is reached.

The three above mentioned effects are called homogeneous broadening effects. The following one is called *inhomogeneous*, as different atoms posses differing line shape functions or center frequencies.

- **Doppler broadening:** An atom which is moving with a certain velocity $\boldsymbol{v}$ along a certain direction exhibits a spectrum that is shifted by $\pm(\boldsymbol{v}/c)\nu_0$ in regard to the central frequency ν_0 due to the Doppler effect. The sign depends on the viewing point of the observer (+ towards, - away from observer). In a thermal equilibrium atoms follow a Boltzmann distribution, so that the number of absorbed or emitted atoms in a frequency interval $[\nu, \nu + \delta\nu]$ is

$$n(\nu)\mathrm{d}\nu = \frac{c_0 N}{\nu_0\sqrt{2\pi k_B T/m_0}} \mathrm{e}^{-[c_0(\nu-\nu_0)/(\nu_0\sqrt{2k_BT/m_0})]} \tag{3.31}$$

The intensity distribution follows a Gaussian profile with a FWHM of:

$$\Delta\nu_D = \frac{2\nu_0}{c_0}\sqrt{\frac{2k_BT\ln 2}{m_0}} \tag{3.32}$$

Taking into account the fact that the distribution of the emitted and absorbed atoms follows a Lorentzian line shape due to their finite lifetime a convolution of a Gaussian and Lorentzian line shape has to be made, which gives a Voigt (intensity)

profile

$$I(\nu) = \frac{\Delta\nu I_0 N c_0}{2\pi^{3/2}\nu_0\sqrt{2k_BT/m_0}} \int_0^\infty \frac{\mathrm{e}^{-[c_0^2(\nu-\nu')^2/(\nu'^2 2k_BT/m_0)]}}{((\nu-\nu')^2 + (\Delta\nu/2)^2)} \tag{3.33}$$

with $\nu' = \nu_0(1 + v_Z/c_0)$ where v_Z is the velocity along the axis of observation.

3.3 Stepwise photo-ionization

In 1971 R. V. Ambartsumian, V. P. Kalinin and V. S. Letokhov published an article on the *two-step selective photo-ionization of rubidium atoms by laser radiation* ([AKL71]). It was one of the first experiments using the resonance ionization technique. With two or more lasers one successively excites dipole transitions in an atom so that finally the total applied energy is higher than the ionization potential. This method exploits the uniqueness of the ionization scheme required for a chosen element due to its atomic structure 'fingerprint', resulting in an element selective (and some cases isomer or isotope selective) ionization process.
There are different processes that may contribute to the ionization of a (highly excited) atom.

3.3.1 Surface ionization

One mechanism, which can lead to unwanted isobaric contamination at ISOL facilities, is surface ionization. Based on the work by J. Eggert [Egg19] M.N. Saha derived the ionization state of an element in a gas after evaporation from a surface with a certain temperature [D.S20]. This formula is e.g. used in astrophysics to classify the spectra of stars. Applying it inside a cavity with a surface which has a work function W the Saha-Langmuir equation results [Dre68] [2]:

$$\frac{n_+}{n_0} = \frac{g_+}{g_0} \exp\left(\frac{W - E_{IP}}{k_BT}\right) \tag{3.34}$$

It describes the 'degree of ionization', namely the ratio from surface ions n_+ to neutral atoms n_0. $g_{+,0}$ are statistical weights for the ionic and atomic states. The equation shows that the surface ionization depends on the work function W and the ionization potential E_{IP}. If the ionization potential is low the surface ionization is high, therefore alkalies and also lanthanides are easily surface ionized.
The Saha-Langmuir equation can only be used as an estimation of the ionization probability in a single atom/surface interaction. The actual surface ionization efficiency does also depend on the ion survival after the wall collision and the average number of atom-wall collisions per atom, so that experimental data is needed for better assessment.

[2] as mentioned in the paper by M. Dresser there is a paper by I. Langmuir & K. Kingdon [KL23] that is often cited for the Saha-Langmuir equation but does not truly give it in the form in which it is generally known today

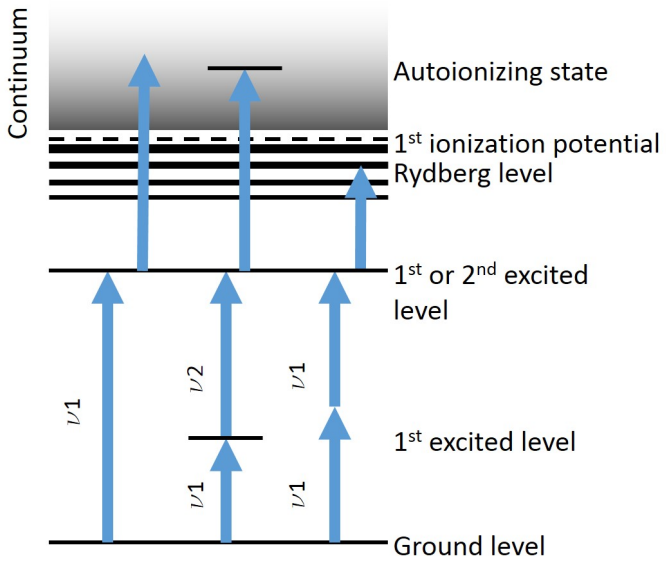

Figure 3.2: *In this sketch the different possibilities of laser ionization are shown. Depending on the ionization scheme two or three lasers are needed for the ionization process.*

3.3.2 Laser-light induced ionization

The three possibilities for laser-light induced ionization are the following (schematically depicted in Figure 3.2):

- **Resonant ionization via autoionizing states:** An AIS is an electron configuration with a total excitation energy that exceeds the ionization energy of the atom. Ionization occurs as a prompt non-radiative decay of this state. The typically short lifetime of an AIS is responsible for its characteristically broad linewidth. The cross section for this process can be up to three orders of magnitude higher than for non resonant ionization, therefore needing less laser power to achieve saturation.
  Usually autoionizing states show a very typical line shape, namely the one described by U. Fano in [Fan61]. The cross section results from the coupling of a discrete state with the underlying continuum and the cross section can be described with

$$\sigma(q,\epsilon) = \frac{(q+\epsilon)^2}{1+\epsilon^2} \quad \text{with} \quad \epsilon = \frac{E-E_R}{\Gamma/2}. \tag{3.35}$$

  The parameter q is the so called skewness of the line and can have either a positive or negative sign. For $q < 0$ the abscissa in Figure 3.3 has to be reversed. The reduced energy ϵ gives the energy difference to the position of the resonance in units of the half width $\Gamma/2$.

- **Non-resonant ionization:** For non resonant ionization the last step is provided by

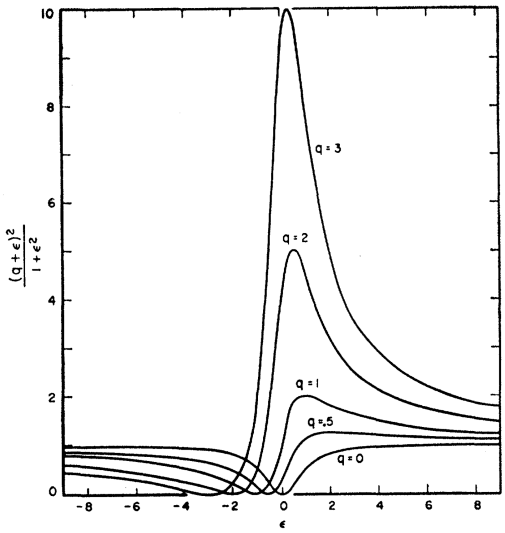

Figure 3.3: *Typical Fano lineshapes for different values of q [Fan61]*

a laser operating at a wavelength that corresponds to a photon energy that exceeds the difference between the IP and the upper state energy of the excitation scheme. Usually high power frequency doubled Nd:YAG ($532\,\text{nm}$) lasers with Gaussian beam profile are used. The fluence condition

$$\sigma_{ni}\Phi_i\tau_l > 1 \tag{3.36}$$

must be met [Mar13]. As the cross section σ_{ni} is usually low for this process ($10^{-19} - 10^{-17}\,\text{cm}^2$) the photon flux Φ_i must be high. With utilization of pulsed lasers with pulse length τ_l in the nanosecond range an average power of the order of around $100\,\text{W}$ at $10\,\text{kHz}$ repetition rate would have to be met. This is not achieved in the current RILIS setup (see [RGF+16]), so that those transitions are normally not saturated and the ion current dependency on power is linear.

- **Ionization via Rydberg states:** The concept of Rydberg atoms has been discussed in detail in subsection 3.1.5. As stated there the binding energy reduces with $1/n^2$ so that once the electron is in the excited Rydberg state it becomes easy to ionize either by applying an electric field, collision with other atoms/ions or just simply via the absorption of black body radiation inside the hot cavity.

3.3.3 Applications of resonance photo-ionization

One of the experimental applications for the photo-ionization is resonance ionization mass spectrometry (RIMS). Mass selectivity can be achieved using a mass filter dispersive element, realized e.g. by a sector field magnet, a quadrupole mass filter or a time of flight apparatus. The RIMS technique is for example used for the ultra trace analysis of rare isotopes in environmental samples. This is done in the working group LARISSA in

Mainz. The preparation of clean samples for the ECHo project is another recent usage [Sch16]. There is no scanning of the mass, but a chemically produced sample with long lived isotopes which can be purified using resonance ionization in combination with a mass separator.
The combination of using a mass separator with a resonance ionization laser ion source is also used at ISOLDE. At ISOLDE it is possible to extract samples of short lived isotopes as extraction of isotopes occurs immediately after production, with a target/ion-source and ion beam delivery system combined in a single machine (see section 2.1). Using the aforementioned combination of separator for mass selectivity and laser ionization another application, the resonance ionization spectroscopy (RIS) is possible. For RIS the wavelength of the lasers is scanned in order to determine nuclear or atomic properties of different elements or across an isotope chain for a single element. Nowadays, thanks to the development of very narrow linewidth lasers and geometries that make Doppler free ionization possible, a sub-Doppler resolution can be achieved in experiments where RIS is applied. With the special case of in-source spectroscopy where the ionization is happening directly in the ion source, isotope shifts can be measured with enough precision to give insight into the variation of the nuclear structure with varying number of neutrons (see e.g. [MAA+13]).

4 The compact Photo-Ionization Spectroscopy Apparatus (PISA)

This chapter provides a technical description of the PISA along with details of its performance characterization after installation in the ISOLDE RILIS laboratory. A summary of the first tests of the device and an overview of its intended applications are also given.

4.1 PISA: Setup

The PISA has been designed by T. Kron during his diploma thesis [Kro11]. The basic setup can be seen in Figure 4.1. The PISA is a vacuum chamber in T-shape and contains an oven (vaporization of sample), ion optics and an ion detector. There are three optical windows, through which laser beams can be directed into the cell either in parallel to the atomic beam or perpendicular to it. As a laser linewidth dependent resolution can be achieved in the perpendicular setup, it is the preferred mode of operation. The compact volume and small footprint of the PISA facilitate its implementation in existing laboratories where available space for new equipment may be limited. The ion optics are kept minimalistic, so that only three power supplies are needed for operation.

Figure 4.2 shows the results of a ion trajectory simulation. The complete ion optics consist of three electrodes:

- **Surface ion repeller:** This improves the laser-ion signal to background ratio by repelling surface ions generated from the hot oven before they can reach the extraction region. It is a positively charged electrode typically held at a potential of $9\,\mathrm{V}$.
- **Plate:** The Plate creates a potential which bends the ions that are produced just behind the repeller away from the back of the PISA. It is situated opposite the repeller. It also has a positive voltage of $66\,\mathrm{V}$. During the optimization process of the ion optics no significant influence of this electrode could be seen.
- **Lens:** The Lens helps to extract the ions from the chamber and focuses the ion beam into the SEM. It is on a negative potential between $300 - 400\,\mathrm{V}$ depending slightly on the potential of the secondary electron multiplier (SEM).

The detector is a secondary electron multiplier (SEM) of the model MC-217 from the company MasCom Technologies GmbH. A negative voltage of $1.75 - 1.90\,\mathrm{kV}$ is applied, depending on the desired detector gain. An exact number for the multiplication factor

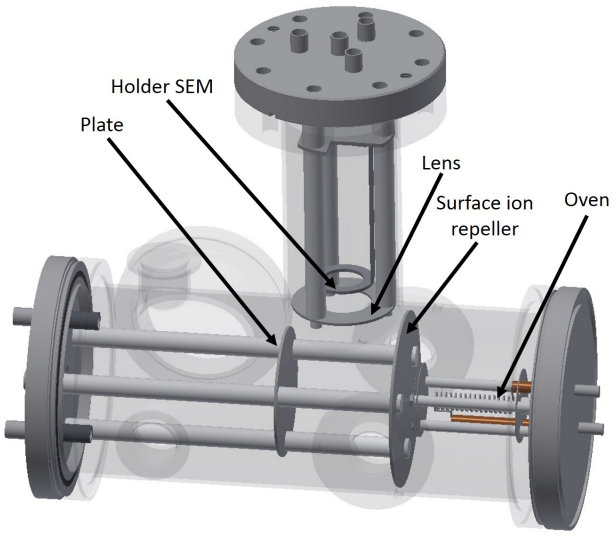

Figure 4.1: *Simplified drawing of the PISA. The device is very compact (footprint around* $30\,cm \times 17\,cm$*) and the interior minimalistic, composed of only three electrodes, a detector and a small oven assembly. A description of the components can be found in the text below. The drawing was created with Autodesk Inventor by T. Kron [Kro11].*

cannot be given but according to the data sheet provided by the company the gain at $1.8\,\text{kV}$ is $> 10^6$ (see appendix Figure 8.1). The power supplies that were used for the setup are CEAN N1471A. They have a current limit of $310\,\mu\text{A}$ and can supply a voltage of up to $10\,\text{kV}$. A short description of how to operate the PISA can be found in the appendix in section 8.3.

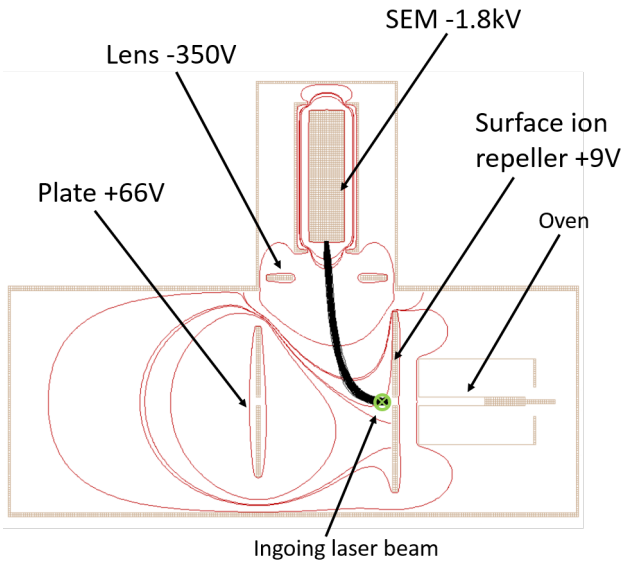

Figure 4.2: *Ion trajectory simulation of the PISA, created by T. Kron, using SimIon. The different electrode potential lines (red) are shown with the resulting path the ions would take (black) to get into the detector [Kro11].*

4.2 General requirements for the PISA

In order to fully integrate the PISA into the RILIS setup and to achieve convenient and reliable operation some general requirements will have to be met:

- **Sample switching:** For the PISA to become a viable tool for RILIS performance monitoring during standard RILIS operation, the time required to obtain a suitable ion signal (including sample change, pumping, ion signal optimization) should not exceed 1 hour.

- **Temperature:** Ideally, the PISA oven should be able to generate an atomic beam of any element that can be released as an atomic vapor from the ISOLDE target. The achievable temperature will have to be high (e.g. > 1400°C for Cr), enabling scheme development for non-volatile elements as well as for volatile ones. This requires a cooling system which makes sure that less heat resistive parts are not damaged (cables, vacuum seals or others) and which ensures that the room temperature is not affected by a high oven temperature.

- **Selectivity:** In order to further improve the capabilities for ionization scheme development a mass selective element, e.g. a rest gas analyzer, should be included in the design. It would be able to suppress background that is either ionized by high-energy first/second ionization steps or by collisional ionization. In addition the isotope shift of multiple stable isotopes could be measured as well as possible differences in the hyperfine structure. This would provide a viable tool during the

application of the PISA as a reference cell for in-source spectroscopy, as single mass resolution is needed for elements with more than one stable isotope.

- **Detection efficiency and dynamic range:** The SEM needs to be able to operate in two different modes, namely single ion counting and current (analogue) mode. In single ion counting mode a detection threshold can be set, increasing the signal-to-noise ratio. Using an oscilloscope with the possibility of storing this information into histograms, the signal can be accumulated over several laser shots. A gate can be set for the ion arrival time, further increasing the signal-to-noise ratio. The signal can also be measured in current mode if it is well above the background. Here a continuous readout of the ion current takes place. An easy switch should be possible, with a possibility of data collection for both modes. For a more specific description of the working principle of an SEM see section 8.2.

4.3 Overview over possible applications

The PISA can be mainly used for three different applications (as suggested first in [Rot11]). These will be described in the following section along with details of the specific performance requirements that each application demands.

4.3.1 Optimization and tests during setup for RILIS on-line applications

During the on-line period at ISOLDE both mass separators are used to capacity with typically more than two experiments scheduled per week. In order to use the given time to optimum, fast setup of the lasers and of the target is required.
The PISA provides an opportunity to test and optimize several aspects of the RILIS setup for application to particular chemical elements prior to the availability of the ISOLDE infrastructure:

- optimization of the laser wavelength
- optimization of the pulse timing
- possibility of laser linewidth assessments (e.g. test if hyperfine structure is resolved or not)

4.3.2 Ionization scheme development

Another application for the PISA is ionization scheme development. The primary advantage of PISA for this application is that, since it is located in the RILIS room, the array of RILIS lasers can be used for this purpose. Since the same lasers are used for scheme development and for eventual ion beam production at ISOLDE, the suitability of the resulting ionization scheme in terms of the achievable laser performance is not under question. An example for scheme development on the element europium can be found in chapter 5.

4.3.3 Reference cell

One major application foreseen for the PISA is its use during in-source spectroscopy. During the in-source experiment, scans of the stable isotope need to be carried out regularly in order to have a reference for potential drifts of the wavemeter or changes in laser performance. Recording the ion current measured in the PISA and the ion signature on one of the detectors used for the in-source spectroscopy experiments will provide a reference scan of the stable isotope for each radiogenic one. In addition the orthogonal laser and atom beam geometry results in an experimental spectral line which is dominated by the laser linewidth.

4.4 Commissioning and current status of the PISA

The PISA was installed in the RILIS laboratory in October 2015. The results of the initial testing and characterization of this device are provided here, along with an assessment of the degree of suitability of the PISA for the various applications that have been described in section 4.2.

4.4.1 Characterizing the PISA

4.4.1.1 Temperature calibration

After the installation in the RILIS laboratory a temperature calibration of the oven was made. The oven temperature was gradually increased by applying more electrical current to the heating coil. During this process the temperature was monitored using an optical pyrometer (IS 8 pro from LumaSense Technologies), which had line-of-sight to the oven surface through a fused silica vacuum window.
The uncertainty in the temperature measurements was determined by the range of the values obtained from the pyrometer at a constant heating current value. This is reflected in the error bars in Figure 4.3. The temperature calibration was performed twice to assess the reproducibility of subsequent heating cycles. The two curves are shown in Figure 4.3. From the linear fits two curves resulted. from which the following curve was calculated using the mean values for the slope and the intercept:

$$y[\text{°C}] = 52\,[\text{°C/A}] \cdot x[\text{A}] + 236\,[\text{°C}] \tag{4.1}$$

This curve should not be considered as a reliable temperature calibration. Its purpose is to enable a rough temperature estimation during PISA operation.

It should be noted at this point that heat shields were added to the oven after the temperature calibration took place. As the heat shields prevented a direct line-of-sight of the oven, it was not possible to use the pyrometer for a new calibration. The temperature should be higher for the same current settings now, as much of the heat is reflected by the heatshields and therefore contained. For more accuracy it is therefore necessary to

redo the calibration using a thermo couple. Due to changes that have to be made in the design of the PISA to allow for the insertion of such a thermo couple, this remains as a future task.

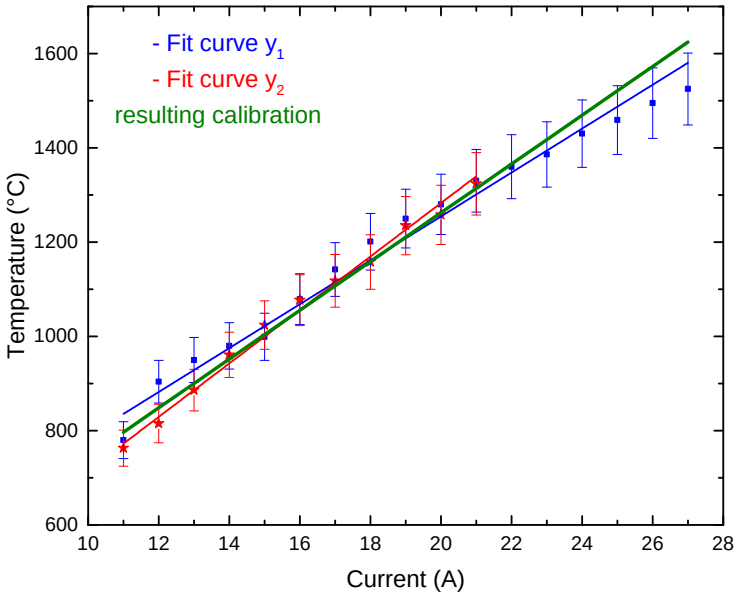

Figure 4.3: *Measurements taken with the pyrometer and the fitted data. The calibration curve resulting from the mean of the two data sets is also displayed.*

4.4.1.2 SEM behavior

The SEM that is being used as detector in the PISA has so far been used in current (analogue) mode[1]. It shows only slight fluctuations in the ion signal, due to dark current caused mainly by temperature effects (spontaneous emissions of electrons at high temperatures can lead to dark counts of around $1/\mathrm{s}$ that are registered by the detector). When no laser ion signal is generated the ion signal fluctuates around $0\,\mathrm{A}$. The readout is done with a Keithley 6487 picoammeter. This is read out remotely by a computer via a RS232 connection. The current can then be plotted over time or other parameters of interest, e.g. the wavenumber during a wavelength scan.

The SEM, although specified for working in ion counting mode, initially did not show a signal, when connected to an oscilloscope. In ion counting mode, with the detector output connected directly to an oscilloscope ($50\,\Omega$ impedance), each ion generates a $8\,\mathrm{ns}$ wide negative pulse. The pulse height depends, amongst other factors, on the detector gain, which can be increased by increasing the voltage applied to the front of the detector. The detector gain should be adjusted to maximize the proportion of ion pulses that have

[1] for a more detailed description of the working principle of a SEM, see section 8.2

a pulse height higher than the signal noise. This way, a discriminator threshold can be set that eliminates the background, without losing the registration of real ion events. If this is not possible then a fast pre-amplifier should be attached, (as close as possible to the detector output), to preferentially amplify the ion signal and facilitate the discrimination of the detector noise.
During the tests the voltage of the lens was increased from the usual value around $-300\,\mathrm{V}$ up to $-1.4\,\mathrm{kV}$. The ion current detected by the picoammeter scaled linearly with the applied voltage. While a low voltage is applied on the lens, the ions are slow and might therefore be attracted to the positively charged lens, without getting to the detector. The higher the voltage on the lens, the faster the ions become, escaping the positive potential and hitting the SEM. It needs to be tested, if the same behavior can be observed with laser ionized particles.
It can be concluded from the tests, that high currents on the picoammeter need to be observed (nA- to µA-range) in order to obtain a significant signal with the oscilloscope. If a current this high can be observed though, there is no need for the single ion counting mode of the SEM. Further investigations into the matter will have to be made, as the typical currents that have so far been detected lie in the pA-range. Increasing the oven temperature and releasing more atoms can increase the current. At this moment though, high temperatures lead to a background in the pA- to nA-range, because of a temperature dependent charging effect of the surface ion repeller (for more details see section 4.5).

4.4.2 Suitability tests for the different applications

In order to determine the suitability of the PISA for all aforementioned applications, different tests were performed. They include scheme development and the use of the PISA as reference cell for different cases.

4.4.2.1 Scheme development for europium

A wide range of wavelength scans (ca. 544 to $910\,\mathrm{nm}$, vacuum wavelength) has been made with the PISA for europium scheme development in order to find new autoionizing states. The details can be found in chapter 5. Additionally these scans showed a wide array of Rydberg states which were used to determine the first ionization potential of europium (see chapter 6). The scans were performed using the full power laser beams. The secondary electron multiplier was used in current mode and read out remotely using the RILIS laser scan recorder. The background during the measurements was negligible, as all surface ions were suppressed by the repeller.
The measurements for the europium scheme development showed, that there is the need for different oven materials: According to [RS95] europium should need a temperature of about 620 °C for a vapor pressure of $1.3 \times 10^{-2}\,\mathrm{mBar}$, graphite, tungsten and molybdenum are specified as suitable crucible materials for the oven/hot cavity. Nevertheless, no signal could be observed at low temperatures using a graphite oven. The heating current needed to obtain a first signal was $18\,\mathrm{A}$ which, according to the temperature calibration in Figure 4.3, corresponds to a temperature of $> 1160\,°\mathrm{C}$. Since the rare-earth elements

are known to readily form carbides the graphite oven was identified to inhibit the release of atomic Eu. Correspondingly the test was repeated with a tantalum foil liner-tube placed in the graphite oven. This way the europium could be evaporated without getting into direct contact with the graphite. Using this configuration, an Eu ion signal was obtained once the heating current reached $10\,\mathrm{A}$ ($\approx 750\,^{\circ}\mathrm{C}$). Based on this validation of the Eu/carbon incompatibility, an all-Ta oven was constructed, and should be used for any future rare-earth scheme development.

4.4.2.2 Reference cell during standard RILIS operation

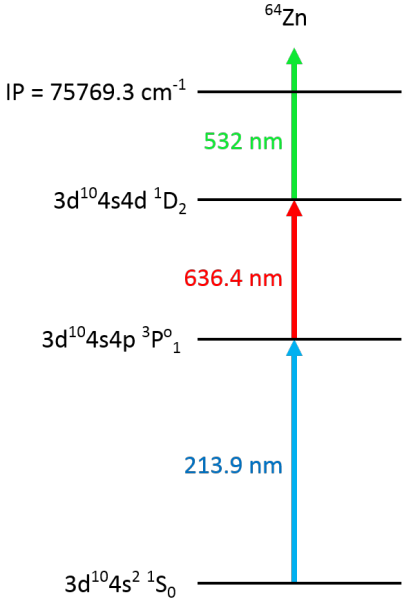

Figure 4.4: *Ionization scheme for Zn with a non resonant last step, the wavelengths are given for vacuum.*

During the first HIE-ISOLDE run in November 2015 a quick test has been carried out using stable zinc in the PISA. A sample of zinc (solution on titanium foil) was inserted into the oven (made of graphite), which was then heated with a current of $7\,\mathrm{A}$ ($\approx 590^{\circ}\mathrm{C}$). The laser reference beams were directed into the cell, using two different mirror sets in order to divide the UV first step from the second and last step. This method ensured a better overlap in the cell, as the UV beam had the smallest spot size and was otherwise no longer overlapping with the other two steps. It took about $3\,\mathrm{h}$ to set up the beam path and the readout of the detector, as this was the first time this was done for the PISA after its integration into the RILIS infrastructure. For the case of Zn it was possible to use the reference beams after the reference iris, as they were not needed. It must be noted though, that some ionization schemes with either very weak reference beams or

two steps with nearly identical wavelength cannot be monitored and stabilized in the way described in section 2.2. For these schemes the reference beams behind the iris are used either for the x/y-stabilization or for monitoring them on the camera.
After a first (laser dependent) signal was observed an optimization of the electrodes was performed. The best voltage of the surface ion repeller was determined to be $+9\,\mathrm{V}$. In accordance with [Kro11] the voltage of the plate was kept at $+66\,\mathrm{V}$. The lens and the SEM were also kept at the voltages found in the thesis [Kro11].
Once the signal was optimized, a wavelength scan of the first step, as depicted in Figure 4.5, was made. The fit which was applied in oder to determine the exact peak position gave a value of $11686.40(3)\,\mathrm{cm}^{-1}$. This corresponds to the value of the fundamental laser wavelength and therefore needs to be multiplied by 4 in order to get the real value for the transition. The transition energy therefore is $46745.60(12)\,\mathrm{cm}^{-1}$ which corresponds reasonably well to the value of $46745.413\,\mathrm{cm}^{-1}$ obtained from previous works ([KYRa15]). The wavelength scan of the second step was recorded in parallel measuring the current of the electron multiplier in the PISA, as well as the current of the Faraday cup FC490, situated in the focal plane of the GPS beamline. Both scans are shown in Figure 4.6. The fits of the peaks give $15713.13(3)\,\mathrm{cm}^{-1}$ for the scan on the SEM and $15713.12(3)\,\mathrm{cm}^{-1}$ for the scan on FC490. The values perfectly agree with each other within their errors and also agree with the value of $15713.15\,\mathrm{cm}^{-1}$ given by former measurements. As the third step is non resonant there was no scan performed for it.
This first test showed, that it is possible to use the reference laser beams for ionization if their power is high enough to induce a measurable ion current. In addition the flexibility of the data acquisition system to enable simultaneous acquisition of a Faraday cup and the PISA SEM data during a laser scan has been demonstrated.

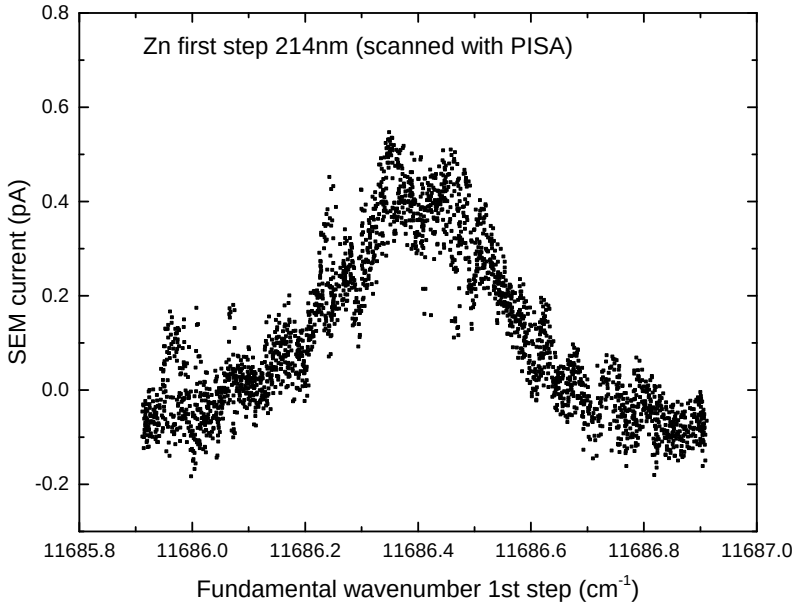

Figure 4.5: *Wavelength scan in the first step. The fundamental wavenumber is given as the abscissa while the wavelength for the transition was produced by frequency quadrupling. The peak center lies at* $11686.40(3)\,cm^{-1}$.

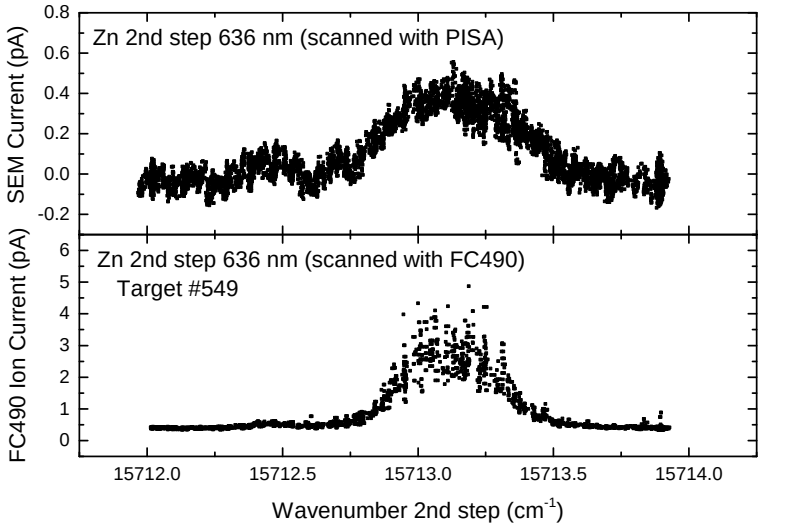

Figure 4.6: *The graph shows the simultaneously taken data during the wavelength scan of the second step. As can be seen the peak forms and positions agree well with each other. The center of the peaks are at* $15713.13(3)\,cm^{-1}$ *and* $15713.12(3)\,cm^{-1}$ *respectively.*

4.4.2.3 Reference cell during in-source spectroscopy with RILIS

The first tests that were performed with the PISA using bismuth had the purpose of verifying the feasibility of using it as reference cell for in-source spectroscopy in June 2016. For this reason the PISA was loaded with bismuth, which was initially ionized using the full power of the laser beams. In Figure 4.7 the ionization scheme of bismuth is depicted. One can see the splitting of the hyperfine structure (F). There are six transitions in total from the ground state into the first excited state. Only the splitting of the excited state, which is around $24\,\mathrm{GHz}$, can be observed (see Figure 4.8) due to the resolution which depends on the laser linewidth. This means that both peaks in Figure 4.8 include three peaks that are not resolved.

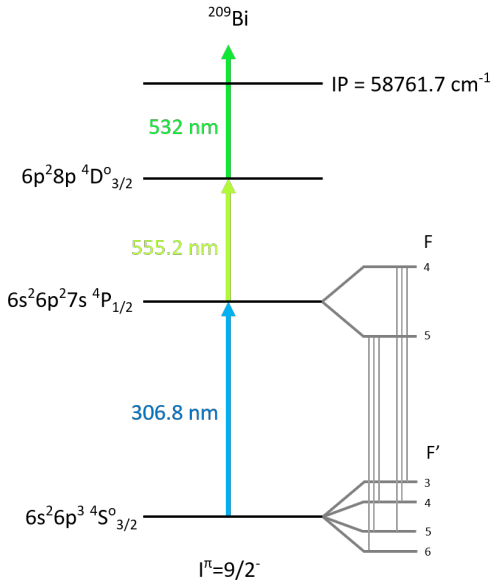

Figure 4.7: *Bi ionization scheme, including the hyperfine splitting of the first step, the wavelengths are given for air.*

The wavelength scans of the first step in Figure 4.8 showed that the first tests on bismuth in the PISA were able to verify some key aspects. A clear difference in the scans of the first ionization step in broadband and narrow linewidth mode was observed. This was an expected effect that could be observed using the PISA[2]. The asymmetry of the peaks which can be seen in the scan resulted from the fact that the automatic timing stabilization had not yet been set up. This shows how crucial timing stabilization is during

[2]Note: In Figure 4.8 the peak widths are around $23\,\mathrm{GHz}$ for the dye laser and around $3-4\,\mathrm{GHz}$ for the NB Ti:Sa. As the Ti:Sa is narrower than the linewidth of the transition (which is around $4\,\mathrm{GHz}$), it is not possible to deduct the laser linewidth from the measurement. As the full power laser beams were used, the dye laser scan is broadened not only due to the laser linewidth ($> 8\,\mathrm{GHz}$) but also by saturation.

scans, in particular as an asymmetry could shift the centroid of the peaks, altering the measurements while also distorting the peak shape which makes a proper fit impossible. The above mentioned measurements were recorded in current mode. When switching from the full power laser beams to the reference beams, the signal was too weak to be detected in current mode. Tests were deducted during which the power of the first step was slowly decreased. While in broadband mode a power of at least 1 mW is needed in order to still get a distinct signal in current mode.

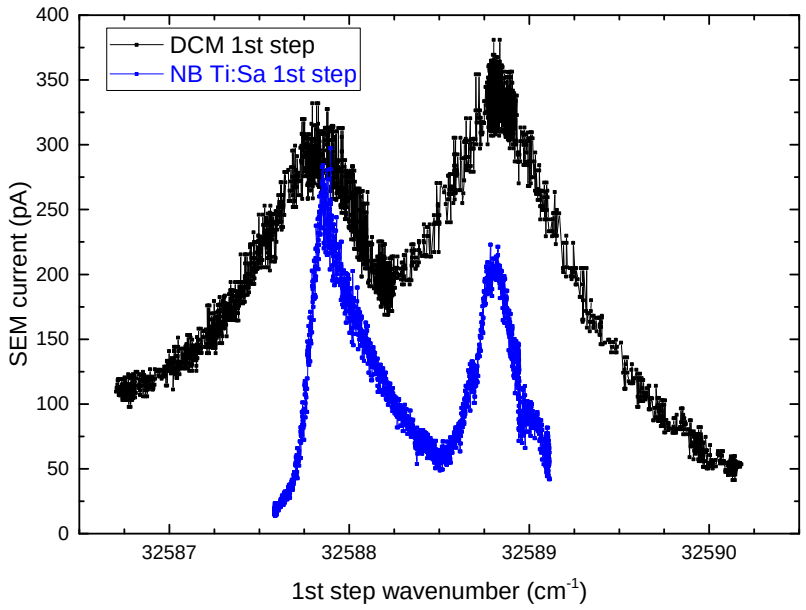

Figure 4.8: *Scans of two different first step excitations using the broadband dye laser with DCM (black) or the narrow band Ti:Sa (blue). For a better overview the x-axis represents the absolute wavenumber of the atomic transition.*

4.5 Conclusion

As outlined in section 4.2 some general demands were imposed upon the PISA. Some of them cannot yet be met. The reasons for this and some possible improvements are given below.

Achievable temperatures

Presently the temperature requirements for non-volatile elements cannot be met. During various tests with the PISA it was noted that there is a charging/electron emission effect on the surface ion repeller with electron currents in the µA-range (measured on the power supply). This effect is temperature dependent and was reproducible over several

measurements. It renders the PISA unusable for too high temperatures, as this effect is coupled to an increasing background detected with the SEM. As it was not possible to clearly determine the source for this effect, two different approaches were attempted to solve the problem.
The first attempt was to install a second repeller on a negative potential. This should suppress those electrons that are ejected by surface ionization and were possibly accelerated towards the surface ion repeller by its positive potential. The introduction of the second repeller on negative potential should hinder the electrons from getting into the main part of the chamber where they can ionize rest gas via collisions. Unfortunately tests with this second repeller were not successful. Temperature dependent effects that could not be specified led to a short circuit between the two repellers, so that the temperature dependent background could not be suppressed.
Another approach to tackle the cause for this temperature dependent effect was to decrease the diameter of the surface ion repeller. The diameter of the repeller was nearly equal to the diameter of the vacuum chamber in which it is situated. The vacuum pump sits about $20\,\mathrm{cm}$ behind it. When the oven is heated, many atoms and/or ions are released which could lead to space charge effects. The outer diameter of the repeller was therefore decreased by $2\,\mathrm{cm}$, leaving a wider gap between the vacuum chamber and the repeller, allowing better evacuation of the volume. Tests showed that an initial charging effect can still be detected. In comparison to former measurements though, the increase in current is not as fast and starts settling after $5 - 10$ minutes. After that it starts decreasing, although a value of $0\,\mathrm{A}$ cannot be reached anymore. The decrease in diameter and therefore increase in gas flow seems to dampen the charging effect. It might be advisable to try to decrease the diameter as much as possible, while still being able to repel the surface ions. Introducing a grid or mesh instead of the solid repeller might also lead to a further decrease in the charging effect. Further investigations are needed in order to completely solve this problem.

New oven design

With the current design of the oven, the housing and the power feed throughs of the PISA are reaching high temperatures (90°C or more) once it is operated for either a long time or at very high temperatures. The addition of a few simple heatshields had already proven that higher temperatures are in reach without the necessity of external cooling. In order to further expand possibilities of heating, a new heatscreen and water cooling shall be installed soon. This would decrease the heat dissipation and make the room temperature of the RILIS laboratory more stable.
The water cooling could be connected to the power feed throughs (see Figure 4.10). Pictures were taken with a thermal imager (see Figure 4.9), showing that the feed throughs are one of the hottest parts of the PISA. The new heatscreen will consist of a copper block enclosing the oven. The connection to the flange, which is connected to the cell and therefore to the table, ensures a temperature conduction which takes off most of the heat. Additionally the heatscreens which are currently used will be kept, as there is still

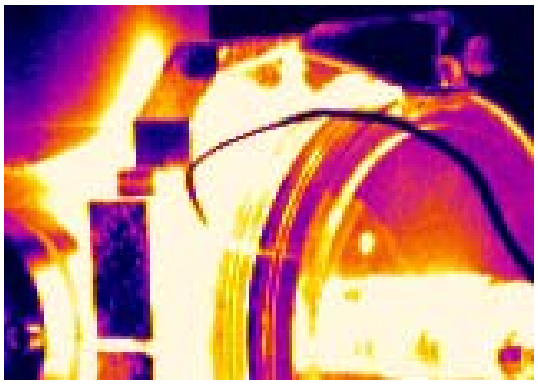

Figure 4.9: *Photo taken with a thermal imager (Optris PI). One can see clearly the power feed throughs, radiating a lot of heat which leads to heating of the flange. Additionally the area where the oven is situated can be seen, as it also has quite a white glow.*

enough space available.
Another feature included in the new design is the mechanism for sample switching. Instead of opening up the whole flange (see section 8.3), only the sample holder will need to be taken out. The tip of the sample holder will be screwed onto an insulating material. Different materials for the actual container of the sample can be used and switched whenever the need arises. This feature has been included, because the tests with the Eu showed that, depending on the element of interest, a switch in oven material is needed. There will be two extra feed throughs on the flange, which can be used in order to insert for example a thermo couple. As long as the feed throughs are not needed, they can remain closed for possible future applications. The feed throughs for the power will no longer be welded into the flange, but attached with CF16 connectors. This gives the possibility of an easy exchange of the power feed throughs.
All of these features make the oven more versatile for future applications, giving also the perspective of re-using the design for other experimental setups should this be necessary. The current design study for the new oven-flange assembly is depicted in Figure 4.10

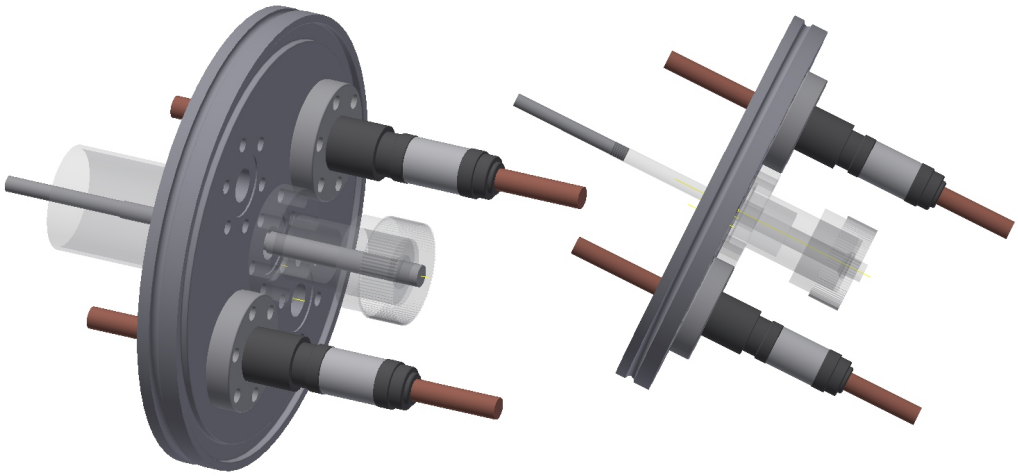

Figure 4.10: *The graphic shows the current status of the oven design. On the left the outside can be seen, in the center of the flange a compression port is situated, which can be screwed open or closed by hand. Once it is open the oven sample holder construction can be removed. This construction can be better seen in the figure on the right. The tip can be unscrewed and changed,so that a switch in oven material is possible, while the rest of the structure remains the same. The tip screws into an insulating material, so that a maximal heating effect can be achieved. A heatsink is added on the inside, attached to flange for thermal conduction to the outside. The power feed throughs use up two of the four holes in the flange. The remaining two holes can be closed with CF16 flanges or used e.g. for thermo couples. CAD drawings for the compression port and the feed throughs downloaded from http://www.pchemlabs.com & http://www.mdcvacuum.eu/*

5 Europium scheme development

The following chapter will give an overview over the scheme development that has been made using the PISA. A short introduction will deduce the necessity of this scheme development, followed by a detailed analysis of the measurements and the new spectroscopic data.

5.1 Motivation

The first resonance ionization schemes for europium were developed in 1982 as described in [ABB+84]. Using a three step scheme leading to an autoionizing state these schemes have been successfully used to study isotopic variations in the charge radii of europium isotopes [ABB+83] as well as to determine many other nuclear characteristics such as nuclear spins I, magnetic dipole moments μ and electric quadrupole moments Q_s [ABD+84, LMS+92, BFI+04] .
In the following years further atomic spectroscopy has been carried out in order to find more autoionizing states [ZLMF87]. Many autoionizing transitions leading to even parity states have been found in the total energy between 45738.3 and $53270.8\,\mathrm{cm}^{-1}$. In addition new schemes using only two steps with a high lying first intermediate excited level have been developed. This can be achieved for example by using a pump laser with $308\,\mathrm{nm}$ which enables the use of laser dyes that emit light in the blue to green spectral range. Different first steps with $\lambda_1 = 459.4\,\mathrm{nm}$, $\lambda_2 = 462.7\,\mathrm{nm}$ and $\lambda_3 = 466.2\,\mathrm{nm}$ have been used by [NRBA96]. Scans have been made in a wavelength range of $459 - 522.5\,\mathrm{nm}$ in order to find new odd parity levels, where the second step also serves as non resonant last step for ionization. In addition scans in the wavelength range of $408 - 461\,\mathrm{nm}$ have been made in order to find further Rydberg and autoionizing states (see [AN99] and [NRCA00]).
Like all the rare earths europium is easily surface ionized. Its ionization potential lies at $= 45734.74(4)\,\mathrm{cm}^{-1}$ $(5.67\,\mathrm{eV})$ [NRCA00]. Therefore it has initially been produced at ISOLDE with yields in the range of 10^8 atoms/s from a tantalum foil target with a tungsten surface ion source [Klu86]. The yields are highly dependent on the target material; e.g. ^{152}Eu with a half-life of $13.3\,\mathrm{y}$ has yields varying from 8.3×10^4 (uranium carbide target & tungsten surface ion source) to 3.2×10^8 atoms/s (gadolinium-lanthanum alloy target & tungsten surface ion source). The RILIS has so far not been used to produce europium beams since the expected surface-ionization efficiency of Eu in a Ta cavity at 2000°C is in the order of $0.38\,\%$ [1]. For indium, which has a similar IP of $5.79\,\mathrm{eV}$, the surface-ionization efficiency is around $0.05\,\%$ and the enhancement from surface to

[1] calculated using the analytical model of the Saha-Langmuir equation as described in [SAB+15]

resonance laser ionization that has been observed is in the order of > 500 ([log]). This leads to the conclusion that an enhancement of a factor > 50 might be expected for Eu under the same conditions. It is therefore reasonable to expect that the application of an efficient RILIS scheme for Eu would enhance the overall ionization efficiency, whilst also providing a convenient laser on/off signal identification tool. In addition, once available, a RILIS scheme for Eu can then be used in combination with the existing or soon to be developed surface ion suppression methods such as LIST ([FRB+15]), VADLIS ([GBC+16]), ToFlis ([MMM09]), low work function cavities and fast beam gating ([RGF+16]).
Radioisotopes of europium are of interest in the solid state physics experiments for Moessbauer spectroscopy as they are used as a semi conductor material in silicon (here at ISOLDE ^{149}Eu would be of interest [2]). It can also be used to measure the topical properties of doped materials, which is important as some properties might change if the Eu is no longer present in its pure form. It is also used as specific doping material in crystals that can be used for quantum memory or quantum computing (see e.g. [LTG+12, SKZ+16]). These beam requests have motivated the scheme development RIS of europium in order to efficiently produce these beams in pure form.

The existing two step schemes need UV ($308\,$nm, as in [AN99]) pumped dyes for the two steps, while the three step schemes need three dye lasers. The existing two step schemes could be realized with the current RILIS setup using $355\,$nm instead of $308\,$nm for pumping the dye. This approach is impractical for routine and round-the-clock RILIS operation since it is known that the UV pumped dyes typically have a significantly shorter lifespan and lower efficiency than commonly used $532\,$nm pumped dyes. A scheme better suited to RILIS and its available lasers would make the setup time faster and enhance the usefulness of the scheme. An alternative and convenient first step that has enough energy to reach the IP with a second step of $532\,$nm or more was determined. Convenient in this context means that the wavelength is easy to reach by frequency multiplications with either a Ti:Sa or a commonly used $532\,$nm pumped dye and a good A-value (order of $10^7\,1/$s or more), which is proportional to the transition strength. For more information see Table 8.4

[2] Private discussion with Karl Johnston, ISOLDE physics coordinator

5.2 Scans with the PISA

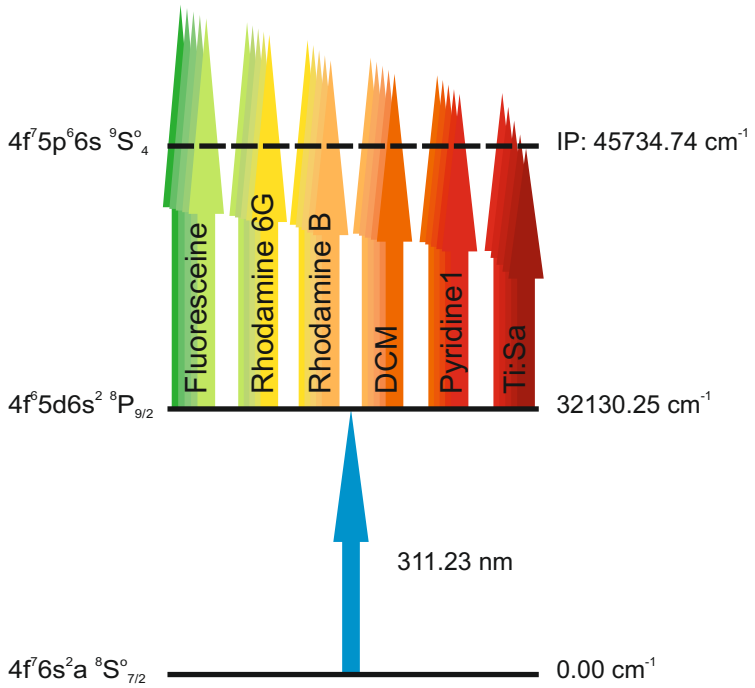

Figure 5.1: *First step as chosen for the scheme development, the wavelength is given for vacuum. Scans of six overlapping dye and Ti:Sa laser ranges, spanning from* 544 *to* $918\,nm$ *were carried out.*

Using the NIST database of energy levels ([KYRa15]), a new first step was chosen. In order to make a two step scheme possible, a high lying level with a good transition rate was chosen. This first step is a transition from the ground state ($0\,\mathrm{cm}^{-1}$) $4f^7 6s^2\, a^8S^o_{7/2}$ to the $4f^6 5d 6s^2\, ^8P_{9/2}$ excited state with an energy of $32130.25\,\mathrm{cm}^{-1}$ and a transition rate A of $3.2 \times 10^7\,1/\mathrm{s}$. This corresponds to a wavelength of about 311.23 nm (in vacuum[3]) which can be reached by frequency doubling a dye laser, using DCM dye. In order to get above the ionization potential an additional energy of $13604.49\,\mathrm{cm}^{-1}$ is needed. This corresponds to a wavelength of $735\,\mathrm{nm}$ or less. Scans beneath this wavelength should reveal autoionizing states whereas scans just above this wavelength (so below the IP) should show some Rydberg states. Finding an optimal AIS transition as second resonant step would complete the scheme development, yielding a scheme which is well adapted to the RILIS capabilities. The scheme (first step transition and scans) is shown in Figure 5.1.
Figure 5.2 shows scans of the first step. They were done with either a ND (neutral density) 1.3 ($5\,\%$ transmission), a 0.3 ($50\,\%$ transmission) or no filter, where the power

[3]Note: Wavelengths given in nm were calculated for vacuum and should only be used as an estimate for determination of the appropriate optics and/or laser dye.

Filter	Peak position [cm^{-1}]	Width [cm^{-1}]
ND 0.3	$16065.146(3)$	$0.319(4)$
ND 1.3	$16065.137(2)$	$0.319(3)$
no filter	$16065.127(3)$	$0.444(5)$

Table 5.1: *Eu first step scans, peak position and width*

without filter was around 100 mW. The resulting peak positions are listed in Table 5.1, giving a weighted mean value of $16065.137(2)\,cm^{-1}$. This corresponds to a transition wavenumber of $32130.274(3)\,cm^{-1}$. As can be seen in the graphs the linewidth for the peak with full power is about 30 % broader. This effect is ascribed to power broadening, which is removed once the ND 0.3 filter is inserted. There is nearly no difference in linewidth between the two different power reduced peaks, leading to the conclusion that they are both no longer saturation broadened.
The difference in the height of the peaks stems from the fact that they were not performed in the same set of measurements. The scan with the ND 0.3 filter inserted took place during the first set of measurements with the Ta-foil lined oven at a much higher oven temperature while the scans with the ND 1.3 and no filter were performed one after another after a decrease in temperature and the change to the full Ta oven (see subsubsection 4.4.2.1 for further information).

5.2.1 Lasers used for the scans

Using a commercial Credo Dye laser from Sirah with different dyes a wavelength range from 544 to 730 nm could be covered in the spectroscopy of the second step excitation. In addition a grating Ti:Sa was used for a wavelength range of 714 to 918 nm making scans above and below the IP possible. This corresponds to a total energy range from approximately 43023 to $50512\,cm^{-1}$. The spot size (diameter) of the laser beams in the interaction region was $\sim 3-4$ mm.
The dyes that were used in particular are listed in Table 5.2 together with the wavelengths which can be generated and the approximate peak powers. The wavelength overlap for all the used dyes was big enough to ensure that there were no gaps in the spectrum, so that after each dye change the same experimental conditions could be regained. In addition the wavelength overlap gives the possibility to compare the positions of the AIS, which can be found in more than one spectrum.

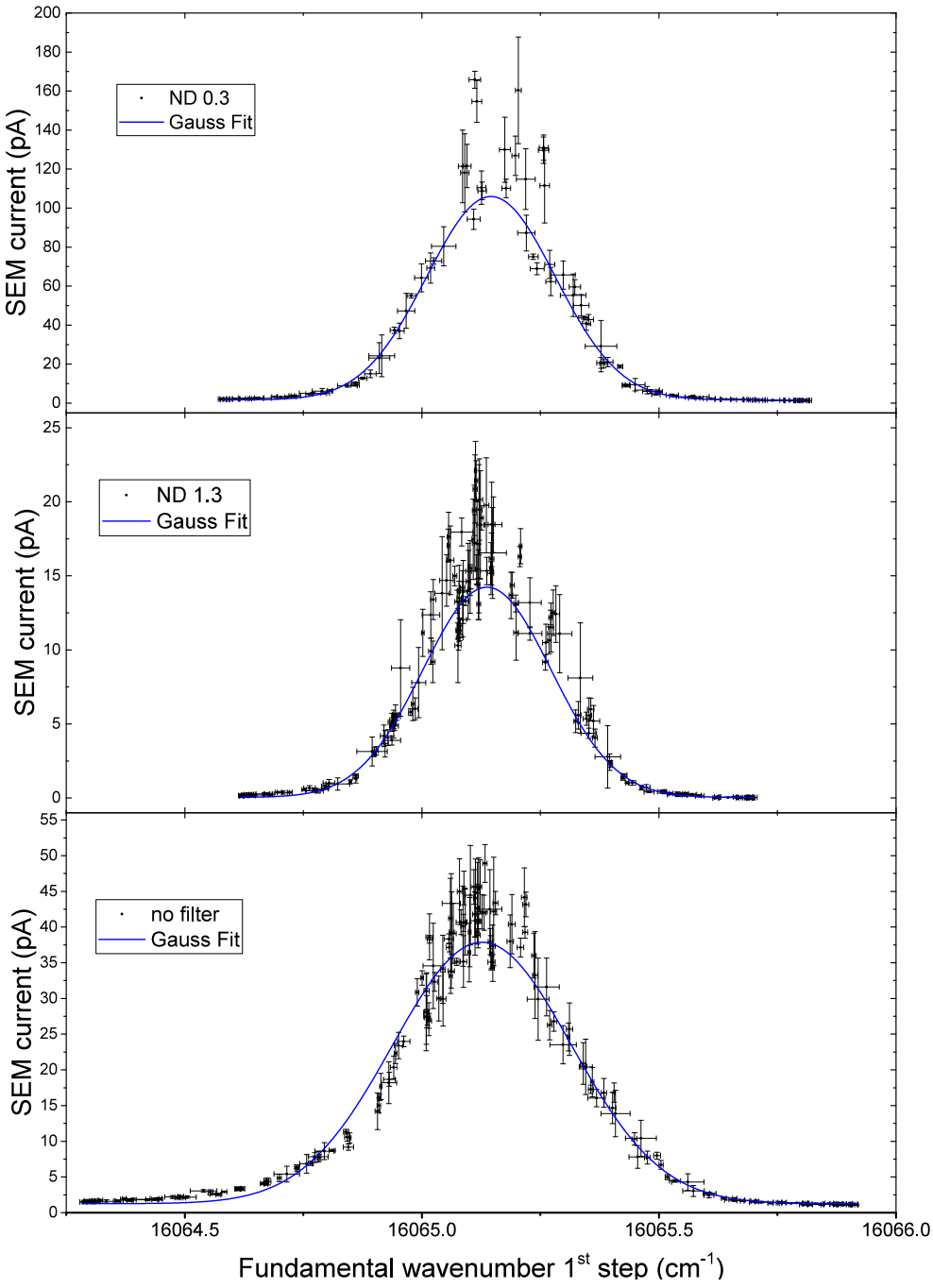

Figure 5.2: *Scans of the first step for Eu for different laser powers are displayed together with the corresponding Gaussian fits. The laser wavelength used for the second step was* $13655.25\,cm^{-1}$. *The positions and widths can be found in Table 5.1*

Dye name	Wavelength range [nm]	Peak power [W]
Pyridin 1	$660 - 730$	2.7
DCM	$610 - 670$	3.7
Rhodamine B	$586 - 627$	3.5
Rhodamine 6G	$557 - 588$	6.1
Fluorescein 548	$544 - 559$	4.8

Table 5.2: *Dyes used for second step scans in europium*

5.2.2 Peak fitting considerations and error analysis for atomic resonances and AI states

The estimated error of the WS7 wavemeter that was used is $\Delta_{WM} = 0.03\,\mathrm{cm}^{-1}$. The first step scans were fitted with normal Gaussian curves using the data analysis program *OriginPro 2015*. The centroids of the fits were then compared to the literature value of $32130.25\,\mathrm{cm}^{-1}$. Assuming that the biggest deviation from the literature value is also the maximal error of the wavemeter, the error of $\Delta_{WM} = 0.03\,\mathrm{cm}^{-1}$ resulted (see Figure 5.2).
Δ_{WM} was then added to the error of each peak resulting from the fits, where the energy was fitted without adding the first step. The final peak position $\bar{x}$ was calculated using the weighted arithmetic mean of the two peaks resulting from the two scans of each spectrum.

$$\bar{x} = \frac{\sum_{i=1}^{n} x_i \cdot \frac{1}{\Delta x_i}}{\sum_{i=1}^{n} \frac{1}{\Delta x_i}} = \frac{\frac{x_1}{\Delta x_1} + \frac{x_2}{\Delta x_2}}{\frac{1}{\Delta x_1} + \frac{1}{\Delta x_2}} \tag{5.1}$$

Here x_i is the value of one peak weighted with its error Δx_i. As the errors differ between the spectra the peak with the smaller error weighs more than the peak with the bigger one. The final error was calculated using the propagation of uncertainty:

$$\Delta\bar{x} = \sqrt{\sum_{i=1}^{n} \left(\frac{d\bar{x}}{dx_i}\right)^2 \cdot \Delta x_i^2} = \sqrt{n} \cdot \left(\sum_{i=1}^{n} \frac{1}{\Delta x_i}\right)^{-1} \tag{5.2}$$

Onto the values derived for the peaks by calculation of the weighted mean value, the energy of the first step was added together with the wavemeter error. In total the wavemeter error is accounted for twice: its size is assumed to be the biggest deviation from the measured wavenumber of the first step to the literature value. Every peak gets assigned this error as systematic error in addition to its fit error. When calculating the final position of energy, the energy of the first step needs to be added, which also contains the error of $0.03\,\mathrm{cm}^{-1}$. Finally this gives $E_{\mathrm{total}} = (32130.25 \pm 0.03)\,\mathrm{cm}^{-1} + (\bar{x} \pm \Delta\bar{x})\,\mathrm{cm}^{-1}$.

As mentioned before each range was scanned in two directions. This method ensures that if there is a 'lacking behind' of the data acquisition (DAQ) compared to the speed of the scan this shift can later on be cleared from the data. In order to take this acqui-

sition error into account both scans were evaluated. The peak positions were tabulated and the differences between the peak positions of the two scan directions calculated. If there is a shift of the peak positions caused by the DAQ this difference should be either always negative or always positive. For all scans the sign of the difference was changing constantly. Therefore a correction was deemed unnecessary.
In addition each spectrum was adjusted as follows: All points giving $0\,\mathrm{cm}^{-1}$ as wavenumber were eliminated. Those points are clearly wavemeter readout errors. To account further for wavemeter readout errors the scanned wavenumber was plotted over time. If there are no errors in the acquisition a line should emerge with the gradient corresponding to the scan speed. Points not lying on that line must therefore be wrong readouts of the wavemeter and can be taken out of the data.
In contrast to the wrong wavemeter readouts stand values stemming from secondary modes in the resonator. A very good example for this case is given in the scan with the Fluorescine dye. Here the MSS was used for the scan. As can be seen in Figure 5.3 there are two parallel lines when one plots the scanned wavenumber over time. This is a result of the laser jumping between two different modes with an offset of $\sim 2\,\mathrm{cm}^{-1}$ between the main and the secondary mode. It is evident that only one of the two modes should be taken into account as otherwise perturbations in the actual spectrum will result. The data of the secondary mode was therefore not used for plotting and evaluating the final spectrum. Some small fluctuations where a second mode appeared were seen in other scans as well and treated the same way as the scan with the MSS.

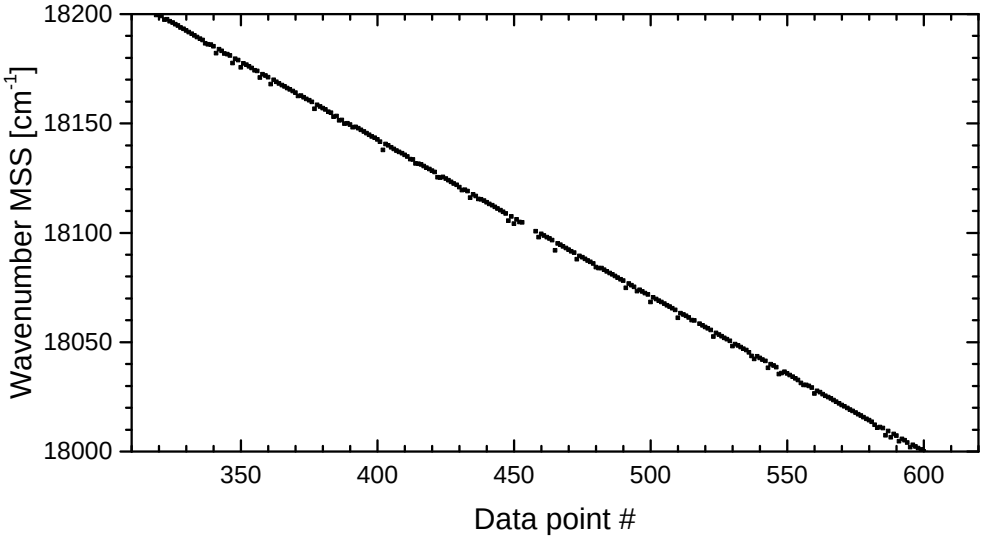

Figure 5.3: *The wavenumber is plotted over time (represented by the number of the measurement). Only a part of the scan is depicted, as the two lines of the different modes lie near to each other (offset $\sim 2\,cm^{-1}$) and can otherwise not be resolved. The lower of the two lines visible in the plot has been neglected for the scan, as it was the weaker mode.*

Because of time restrictions it was not possible to make saturation measurements during the scanning phase. For each new dye range the laser needed to be re-optimized and the circulators cleaned and refilled. Therefore no normalization of the spectra can be performed.

5.2.3 Autoionizing states

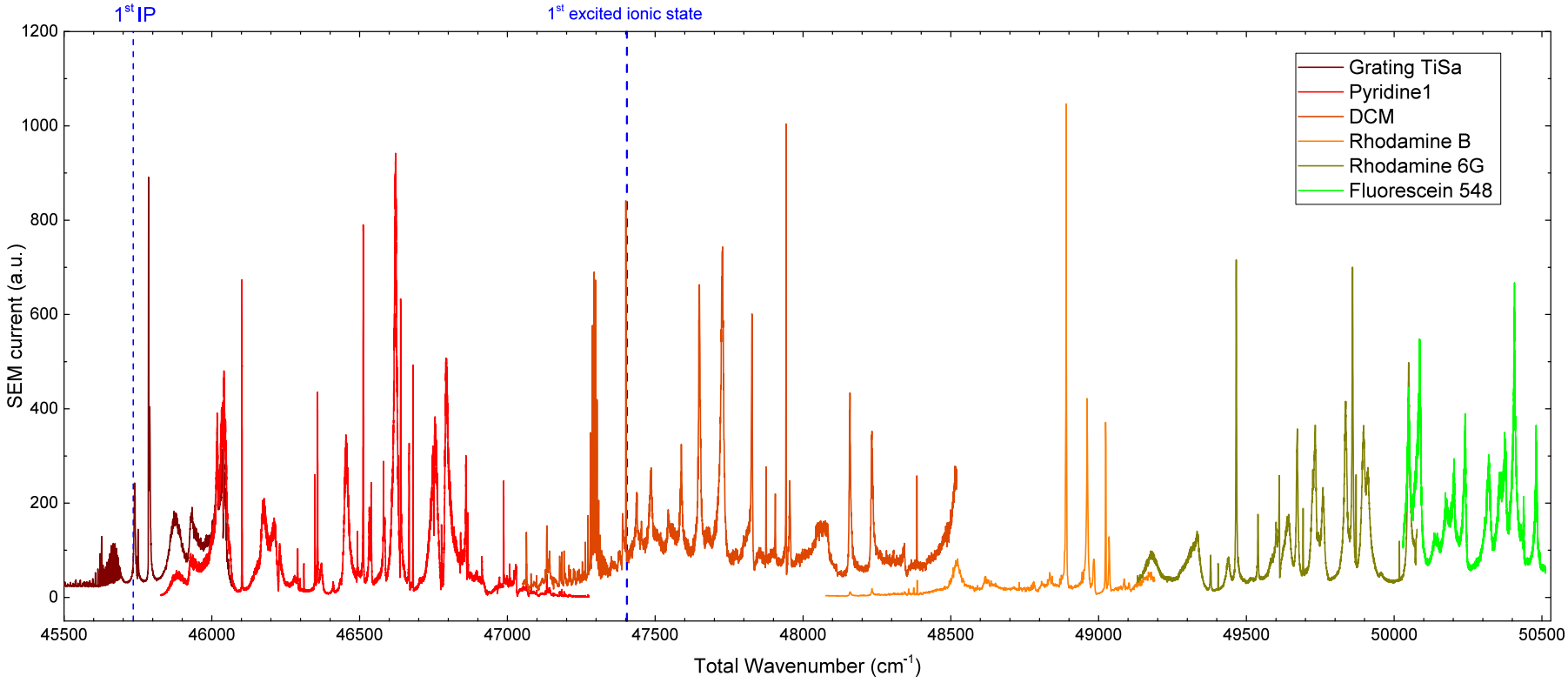

Figure 5.4: *Full spectrum for the second excitation step of europium. The different colors indicate the differing scan ranges taken with either varying dyes or the solid state Ti:Sa laser.*

Figure 5.4 shows an overview over all the AIS that have been found. The height of the peaks has been scaled for the different measurement sets in order to be able to show them in a single plot. For a better scaling of the x-axis the scan taken with the grating Ti:Sa is not fully displayed as it will be discussed in greater detail in chapter 6. The ionization potential is indicated in the plot in order to get a better estimate of the scanned range. The more detailed graphs for all the other scans can be found in figures 8.3 to 8.9 in the appendix. Table 8.2 lists all the AIS that have been found. For the estimation of the errors please see subsection 5.2.2.
During the scans many new autoionizing states were observed.They show the typical Fano profile one would expect for the autoionizing states (see Figure 3.3). The sign of the skewness of the states changes along the scan range. This effect arises due to (broad) interlopers which can weakly couple to a channel of autoionizing resonances. The symmetry reversal occurs near the energy of the interloper, if several channels of autoionizing resonances are strongly coupled to each other but only weakly coupled to the interloper [J.-92]. The paper by J.-P. Connerade and A.M. Lane [CL88] discusses the q-reversal effect in more detail, using a formalism derived from K-matrix theory for a Rydberg manifold perturbed by a broad intruder as basis for their discussion. They try to answer the question how many q-reversals one might expect in a spectrum and if they all arise from the same intruder or from different ones throughout the spectrum. They come to the conclusion that in the general case in photo-ionization "as many as six q reversals can occur" ([CL88], p.1465) but they do not give any specifications about the width of the spectra, which makes this prediction not very useful for practical applications. The number of q-reversals is not easy to determine for most of the europium spectrum, which is due to overlapping resonances that render it impossible to tell if there was a 'real' q-reversal or if the neighboring AIS peaks extend into each other, changing the skewness due to interference effects between them. Wherever the peaks were well separated but changed the sign in q, it was assumed that the coupling to the continuum gave the reason for this change.
As can be observed in the spectrum from the scan of the grating Ti:Sa there is even an AIS rising up right where the ionization potential is located. A closer look at the profile reveals that the side towards lower energies is the lower dipping side of the Fano-profile. The theory of the coupling between the continuum and the autoionizing state would suggest that there might be more factors that would need to be considered for a proper analysis. A conclusive discussion cannot be given, as the theory does not specify a case exactly like the one observed here. Due to the fact that the spectrum is not independent and the distance between the Rydberg states and the AIS is rather small, it cannot be ignored, that there might be interferences, too. The coupling effects are hard to describe even for isolated, single AIS, so that a proper analysis of these states at locations where the continuum, an AIS and a member of a Rydberg series interfere with one another is at this moment not possible.

5.3 Finalization of the scheme development

To validate the PISA scheme development, a comparison of the schemes from the PISA with the same schemes at the standard hot-cavity RILIS system should be made. Such a validation ideally requires the following tests to be performed:
Saturation curves for the first step and different AIS will have to be measured. A comparison between the available non resonant last step and different autoionizing states through relative efficiency measurements will be made as not only the achievable overall ion current determines the decision which scheme to use: A scheme with a resonant last step might yield a lower ion current but might still be preferred. This is due to the ionizing effect that the powerful non resonant laser can have on e.g. interfering molecules with the same mass as the desired element, therefore contaminating the ion beam. In addition the surface to laser ionized particles ratio will have to be investigated. Once these steps have been taken and the best possible scheme has been determined, an efficiency test using a calibrated mass marker should be done, as well as yield checks of radiogenic Eu beam production.
On-line tests are foreseen to be made with an tantalum foil target with a tantalum-cavity, as the tests with the PISA have shown that tantalum seems to work well for extracting the europium.

Proposed ionization schemes

For each scanned range the two strongest AIS have been chosen for a possible ionization scheme. They will need to be compared regarding their ionization efficiencies and the laser to surface ionization enhancement. Even in case of little time and no comparison though, the RILIS will be able to provide an Eu beam, no matter the setup. As all scanned wavelength ranges will yield at least two possible schemes, the setup time will be fast and can be realized with each of the available lasers. The following ionization schemes are therefore proposed, with an indication of which laser (dye) would provide the desired wavelength. The first step can be either realized using doubled DCM dye or tripling a Ti:Sa laser. If there are time restrictions the doubling provides the faster method.

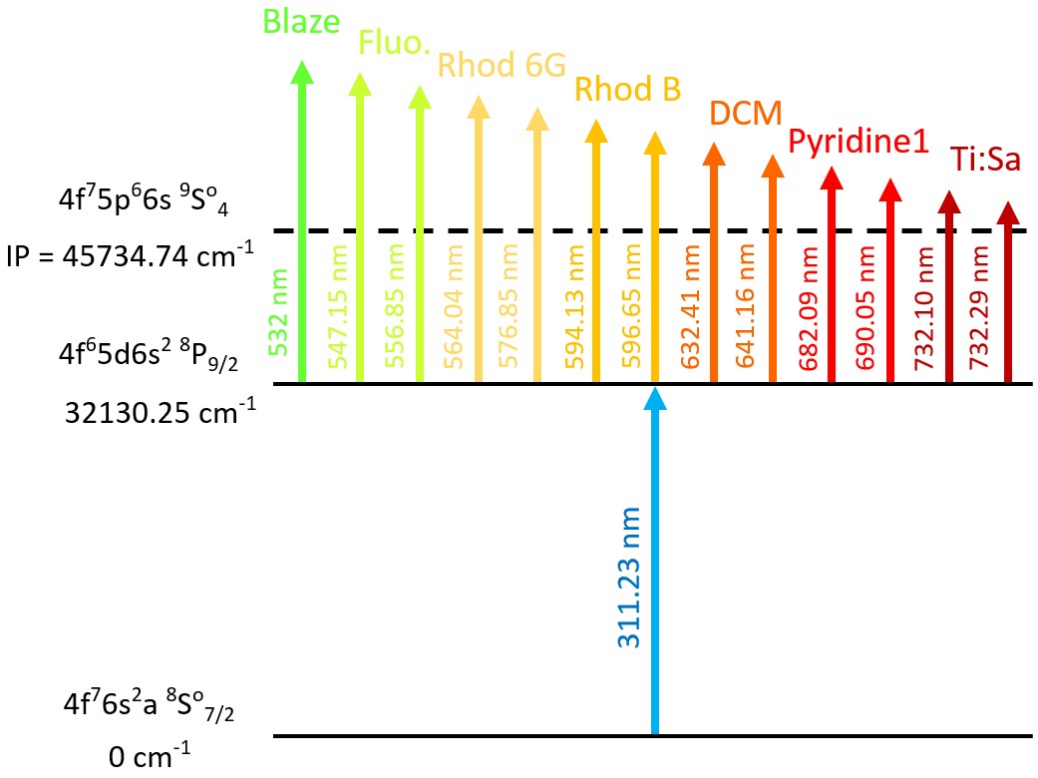

Figure 5.5: *Proposed ionization schemes for europium*

6 Determination of the first ionization potential of europium

The first ionization potential of europium has been determined to be $45734.74(4)\,\mathrm{cm}^{-1}$ by Nakhate et al. (see [NRCA00]), following up on earlier works by Smith and Tomkins ([ST75, ST76]), who published $45734.92\,\mathrm{cm}^{-1}$. As can be seen in the spectra of the scans with the grating Ti:Sa and the DCM dye (Figures 8.3 to 8.6) a large number of Rydberg states converging to the first ionization potential as well as to an ionic excited state were observed in this work.
An analysis has been made of the Rydberg series leading to the first ionization potential in order to compare the recorded data from this work with the literature. The analysis can be found in section 6.1 In addition an analysis of the Rydberg series converging to the ionic excited state has been done. The detailed analysis can be found in section 6.3.

6.1 Rydberg analysis

In order to verify the literature value of the IP for Eu a complete Rydberg analysis was performed on the data depicted in Figure 5.4. The peaks in the Rydberg spectra were fitted using the analysis program OriginPro 2015. For the peaks a Gaussian fit was chosen, as this reproduces the observed peak shape sufficiently well. Two different scans with slightly differing scan speeds were made, the first one during the measurements for the scheme development and the second one in order to get a better resolution and more precise values for the Rydberg states. The direction of the second scan was reversed in order to be able to account for potential shifts caused by the data acquisition. Both spectra were fitted but due to the scanning speed, the second scan has a better resolution, exhibiting a number of peaks that were not observed in the first scan. The found levels were tabulated and compared. Wherever the same levels were found in both spectra the weighted mean value (see subsection 5.2.2) was calculated. The final values that are given in Table 8.3 are a mixture between peaks that were only found in one of the two spectra (here the error is the fit error + the wavemeter error) and values that resulted from calculating the weighted mean between two peaks from the different spectra (here the error is the error of the weighted mean value + the wavemeter error).
For an overview of all the formulas that have been used for the Rydberg analysis see subsection 3.1.5. The mass corrected Rydberg constant for Eu is $R_\mu = 109736.9195\,\mathrm{cm}^{-1}$. The values for the quantum defect δ and the effective principal quantum number n^* were calculated according to Equation 3.13. Then the significant figures of δ were plotted over n^* for different values of E_{IP}. These plots gave a first graphical starting point for the analysis. Once a value had been determined for which a good trend towards linear values

for δ was obtained, the values for the quantum defect and the ion signal were plotted over n^*. This plot is given in Figure 6.1, with the data from the second recorded dataset. The purpose of this plot is to graphically determine which series might belong together by looking at the shape as well as their position in the spectrum. This makes it easier to determine some of the patterns. For example a triplet of peaks that gets more and more separated the further one goes down in energy, can be distinguished. Patterns like these help in the series identification.

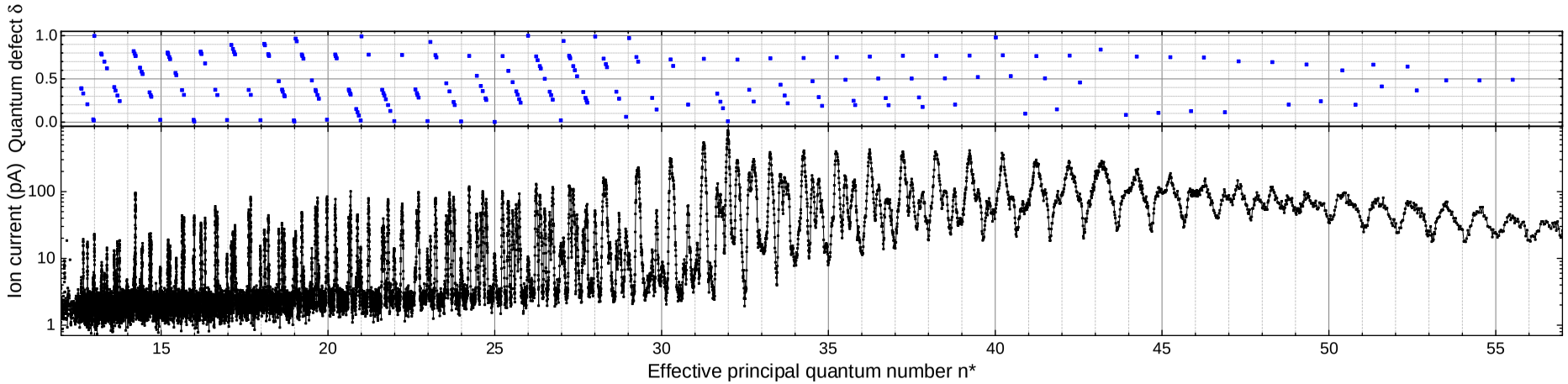

Figure 6.1: *The plot shows δ and the ion current over n^*. It was used in order to assign the different series. The shapes and relative positions of the peaks were taken into account, in order to determine the series members.*

U. Fano et al. calculated the quantum defect for different series (f, d, p, and s) for all elements up to the atomic number $Z = 102$. The result of these calculations is depicted in Figure 6.2. For europium with $Z = 63$ the following quantum defects were extracted from this plot:

Table 6.1: *Theoretically calculated quantum defects for europium [FTD76]*

Series	Quantum defect δ
f-wave	1.00
d-wave	2.78
p-wave	3.75
s-wave	4.24

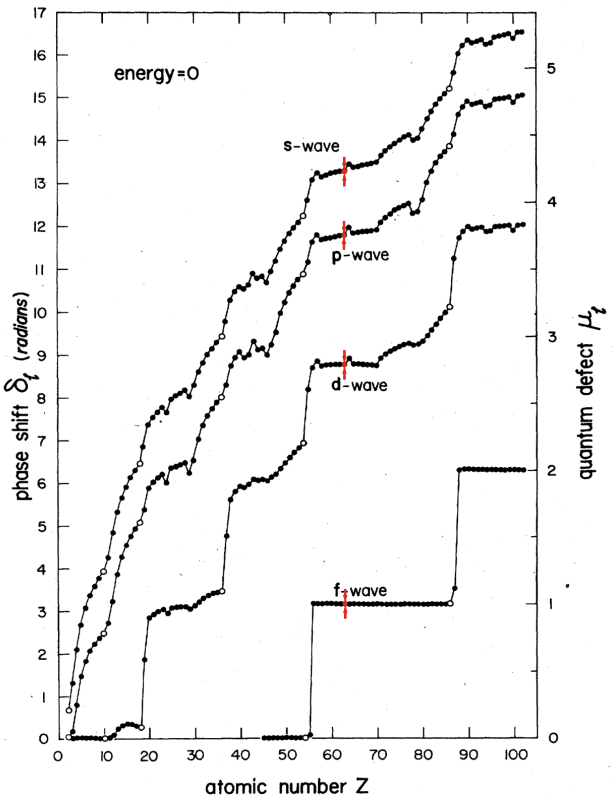

Figure 6.2: *Quantum defects for different series depending on the atomic number Z. The data points for Eu are marked with red dots, the data for δ was extracted using OriginPro 2015 [FTD76]*

It can be assumed that s- and d-series, as listed in Table 6.1, might be observed, as the possible configurations accessible from the excited state ($4f^6 5d6s^2\,{}^8P_{9/2}$) are:

$4f^7 6s(^9S_4^o)\,ns$ with $J = 7/2$ or $9/2$

$4f^7 6s(^9S_4^o)\,nd$ with $J = 7/2,\ 9/2$ or $11/2$

Other possible series might stem from transitions, where the f-electron stays in an excited state, e.g. $4f^6 6s^2 nf$. These possible series would most likely lead to a final state which lies above the IP.

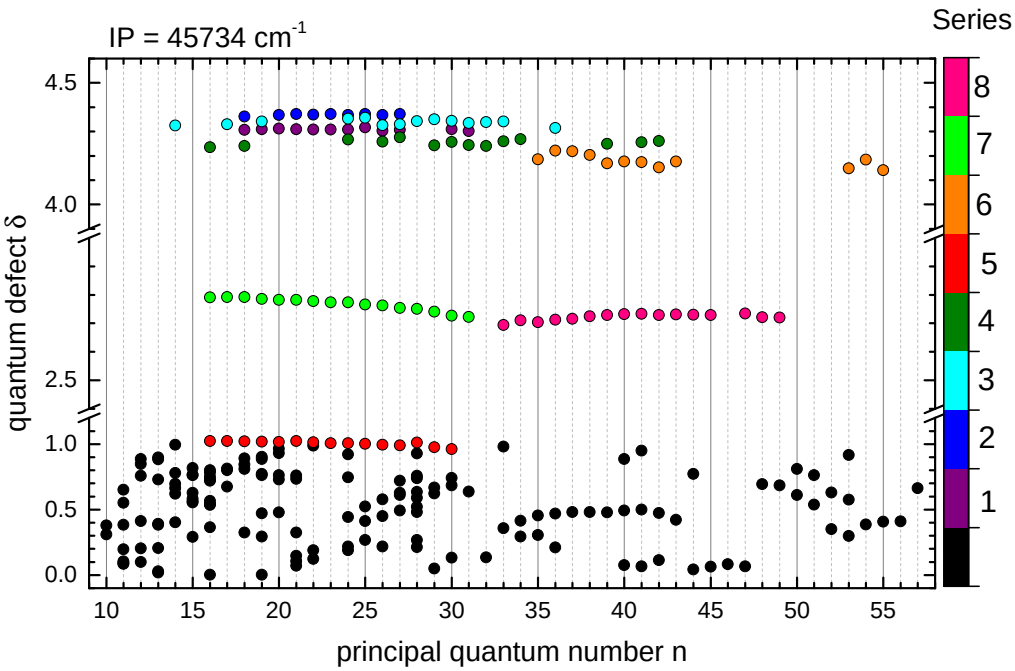

Figure 6.3: *The quantum defect is plotted over the principal quantum number n for an assumed series limit of $E_{IP} = 45734.00\,cm^{-1}$. The different series that have been chosen for fitting are marked in different colors. The black point belong to levels that have bot been assigned to either of the series.*

Figure 6.3 shows the quantum defect over the principal quantum number n for an assumed series limit of $E_{IP} = 45734.00\,\mathrm{cm}^{-1}$. This limit was chosen as a starting point from which to do the fitting, as the values for the quantum defect showed good convergences towards constant values. Individual series that were identified in a certain range of the plot and were chosen for fitting are marked in different colors, indicated on the color scale on the right hand side of the plot. The fit was done according to Equation 3.17. The two most prominent of the fitted series are depicted in Figure 6.5 and 6.4 while the rest of the series can be found in the appendix (section 8.6). An overview over the fitting

parameters and the derived ionization potential can be seen in Table 6.2. For series 6 β was in the order of 10^{-10}, so that it was negligible for the fit.

Series No.	No. of peaks	δ_0	β	IP [cm^{-1}]
1	12	0.33 ± 0.01	-2.88 ± 1.40	45734.24 ± 0.14
2	9	0.41 ± 0.01	-7.17 ± 1.36	45734.51 ± 0.16
3	14	0.35 ± 0.01	-2.13 ± 0.59	45734.05 ± 0.12
4	14	0.26 ± 0.01	-4.09 ± 1.45	45734.01 ± 0.11
5	15	1.05 ± 0.01	-4.09 ± 2.33	45734.62 ± 0.14
6	12	0.23 ± 0.02		45734.19 ± 0.10
7	16	0.806 ± 0.005	-0.96 ± 0.92	45734.77 ± 0.07
8	16	0.88 ± 0.03	-140.93 ± 21.81	45734.19 ± 0.05
Weighted mean				45734.33 ± 0.03

Table 6.2: *Values for the fit parameters of the chosen series. For series 6 the first order expansion was not used, as the errors for β were larger than the values themselves.*

Series 1, 2, 3 and 4

The value for the IP is IP$_{fit} = 45734.24(14)\,\text{cm}^{-1}$ and the fractional part of the quantum defect for series 1 is $\delta_0 = 0.33(1)$. Looking at the theoretical values for the quantum defect, the nearest one would be the one of the s-series at $\delta_s = 4.24$. It could therefore be assumed that the members of this series belong to an s-series.
The value for the IP is IP$_{fit} = 45734.51(16)\,\text{cm}^{-1}$ and the fractional part of the quantum defect for series 2 is $\delta_0 = 0.41(1)$. Looking at the theoretical values for the quantum defect, the nearest one would be the one of the s-series at $\delta_s = 4.24$. It could therefore be assumed that the members of this series belong to an s-series but the deviation is rather large.
The value for the IP is IP$_{fit} = 45734.05(12)\,\text{cm}^{-1}$ and the fractional part of the quantum defect for series 3 is $\delta_0 = 0.35(1)$. Looking at the theoretical values for the quantum defect, the nearest one would be the one of the s-series at $\delta_s = 4.24$. Once again a concrete assignment cannot be made as the deviation from the theoretical value is too big.
The value for the IP is IP$_{fit} = 45734.01(11)\,\text{cm}^{-1}$ and the fractional part of the quantum defect for series 4 is $\delta_0 = 0.26(1)$. Looking at the theoretical values for the quantum defect, the nearest one would be the one of the s-series at $\delta_s = 4.24$. Series 4 exhibits a very small deviation from the theoretical value for the s-series, making it a likely candidate for this assignment.

The determination of the series members was difficult in the case of these series, as it is a dense region with at least four overlapping series. It cannot be conclusively determined, if the Rydberg levels belong to the same series but are split or if they are different series

that are just closely spaced. All of theses series therefore show gaps, where it was not possible to unambiguously assign the observed levels as members to one of either series.

Series 5

The value for the IP is $\mathrm{IP}_{fit} = 45734.62(14)\,\mathrm{cm}^{-1}$ and the value of the quantum defect for series 5 is $\delta_0 = 1.05(1)$. Looking at the theoretical values for the quantum defect, the nearest one would be the one of the f-series at $\delta_f = 1.00$. The deviation is small enough to assume that the series at hand is indeed a f-series.
For series 5 not the fractional part of δ is given, because plotting the fractional part of δ over n^* revealed, that a shift of $+1$ was necessary for values of δ near zero. For these energy levels the difference between the n^* was around $\Delta n^* \approx 0.9$, so that the resulting values for the fractional part are either slightly bigger than 0 or slightly smaller than 1. Due to the way that these values were calculated no value $\delta < 0$ could be reached, but as the continuity in the n^* is given, it can be assumed that the energy levels belong to the same series. When shifting the values near 0 up by $+1$, this continuity is preserved and therefore the applied shift is justified.

Series 6

The value for the IP is $\mathrm{IP}_{fit} = 45734.19(10)\,\mathrm{cm}^{-1}$ and the fractional part of the quantum defect for series 6 is $\delta_0 = 0.23(2)$. Looking at the theoretical values for the quantum defect, the nearest one would be the one of the s-series at $\delta_s = 4.24$. This is the smallest deviation from the theoretical value, hinting that the series is an s-series.
Series 6 is missing the most members of all series. It has high numbers for n and is therefore in the region of the energy spectrum , where different series members are hard to distinguish. In addition there seems to be a global perturbation around all the quantum numbers > 40. Even the apparently strong series 8 is affected by this, which leads to the exclusion of the level with $n = 46$. It is doubtful that all existing members of series 6 have been determined, making the derived value for the series unreliable.

Series 7

The value for the the IP is $\mathrm{IP}_{fit} = 45734.77(7)\,\mathrm{cm}^{-1}$ and the fractional part of the quantum defect for series 7 is $\delta_0 = 0.806(5)$. Looking at the theoretical values for the quantum defect, the nearest one would be the one of the d-series at $\delta_d = 2.78$. Compared to the other series (as displayed in Figure 6.3) it can be seen that the tail of this series is indeed not converging into a constant value but bending down towards higher members of n. Like all the other values in this work it has been considered for the weighted mean value.

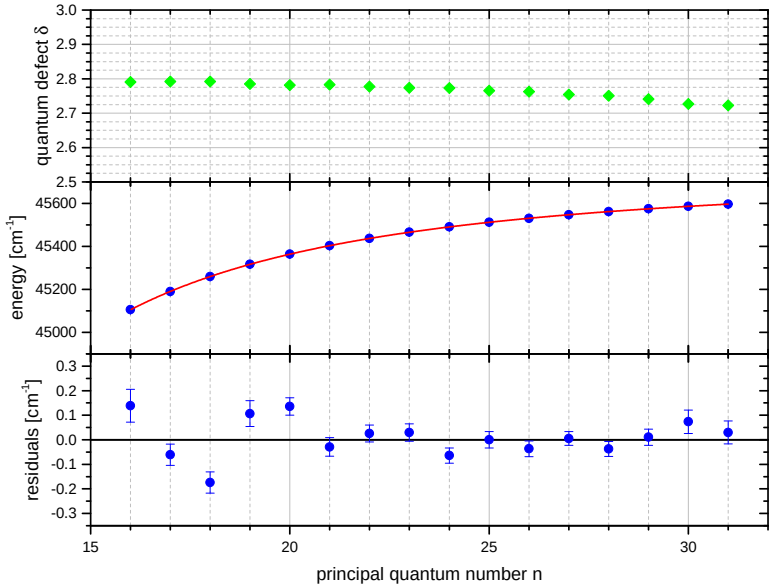

Figure 6.4: *Series 7,* $IP_{fit} = 45734.77(7)\,cm^{-1}$

Series 8

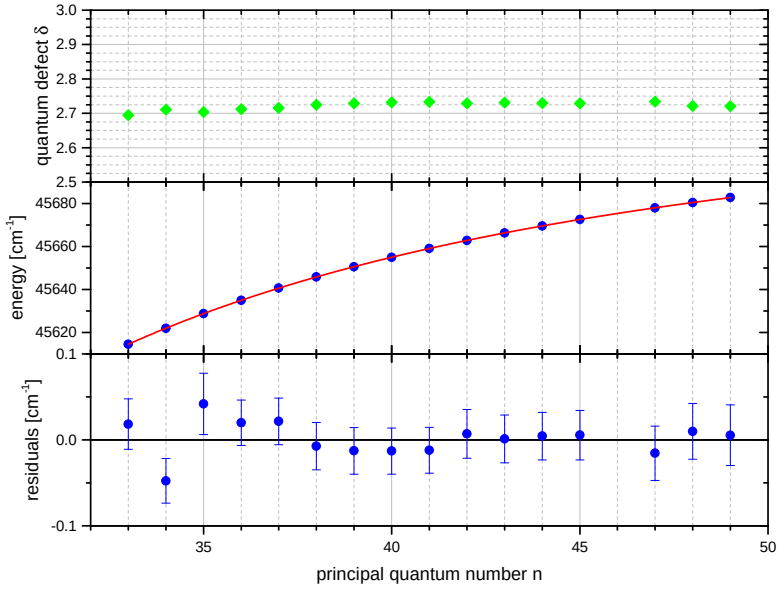

Figure 6.5: *Series 8,* $IP_{fit} = 45734.19(5)\,cm^{-1}$

The value for the IP is $IP_{fit} = 45734.19(5)\,cm^{-1}$ and the fractional part of the quantum defect for series 8 is $\delta_0 = 0.88(3)$. Looking at the theoretical values for the quantum

defect, the nearest one would be the one of the d-series at $\delta_d = 2.78$. The value for $n = 46$ has been left out of the fit. The value for δ deviates from the other levels, as it was not possible to properly fit it. It is part of a triplet of peaks that could not be resolved well enough in this case, so a reliable value could not be given.

There have been no fits performed using the formula derived for a perturbed series as there was no clear signature of a perturbing interloper state that should have been treated with the method described in subsection 3.1.6. It was problematic to properly assign some of the peaks to a series, as in particular peaks near the IP could not be resolved well enough to distinguish positions precisely. From the overall trends there are clear indications that some series disappear/merge into other ones so that the extracted values for the peak positions are shifted for some series or even missing completely. For low series members it became equally hard to assign peaks, as the intensity was shrinking too rapidly well below the IP.

Table 6.3: *Possible bandheads for the Rydberg series ([KYRa15])*

Configuration	Term	J	Energy [cm^{-1}]	quantum defect δ
$4f^7(^8S^o)6s(^9S^o)7s$	$e\,^{10}S^o$	$9/2$	28763.82	4.46
	$e\,^{8}S^o$	$7/2$	29517.86	4.40
$4f^7(^8S^o)6s(^9S^o)6d$	$e\,^{10}D^o$	$7/2$	34440.50	2.88
		$9/2$	34466.80	2.88
		$11/2$	34505.55	2.87
$4f^7(^8S^o)6s(^9S^o)8s$	$g\,^{8}S^o$	$7/2$	36659.31	4.52
	$f\,^{10}S^o$	$9/2$	37195.76	4.42
$4f^7(^8S^o)6s(^9S^o)7d$	$f\,^{10}D^o$	$7/2$	39284.73	2.88
		$9/2$	39306.13	2.87
		$11/2$	39332.68	2.86
	$h\,^{8}D^o$	$11/2$	39486.20	2.81
		$9/2$	39491.49	2.81
		$7/2$	39496.56	2.81

Due to the not fully conclusive assignment of the series (mainly no assignment of j-values), it was not possible to unambiguously assign so called bandheads for extrapolation to small principal quantum numbers that might belong to one of the fitted series. These bandheads are energy levels listed in the NIST database ([KYRa15]) that have known configurations and posses the lowest possible values of n. Due to the selection rules a possible state would need to be odd and have $J = 7/2$, $9/2$ or $11/2$. The states fitting the selection rules that are converging to one of the states with a configuration as

described in the previous text, are listed in Table 6.3. The values for the quantum defect have been calculated using $E_{IP} = 45734.74$. A further investigation into these low lying series members will need to be done in order to better evaluate the identified series.
Figure 6.6 shows a two dimensional contour plot of the experimental data (as introduced in [RWN12]) in which the color code is determined by the ion current. It is a further valuable tool for the interpretation of the data, exhibiting the intensity of the individual peaks and visualizing any limitations induced by the limited resolution of the spectra. In addition is serves as tool for graphical indication for the proper extraction of the IP. Figure 6.6 therefore gives a comparison between the trends of the quantum defect for the literature value and the weighted mean value derived in this work. It is clear from these plots that some of the series seem to be converging towards the literature value while others show a trend towards a lower value of the ionization potential. Towards higher principal quantum numbers the quantum defects are expected to converge towards a constant value. In 6.6 this can be well observed in the lower plot, where the intensities clearly indicate a horizontal trend. The two most dominant structures in the region of $\delta \approx 0.8$ are the two series depicted in Figure 6.5 and 6.4.

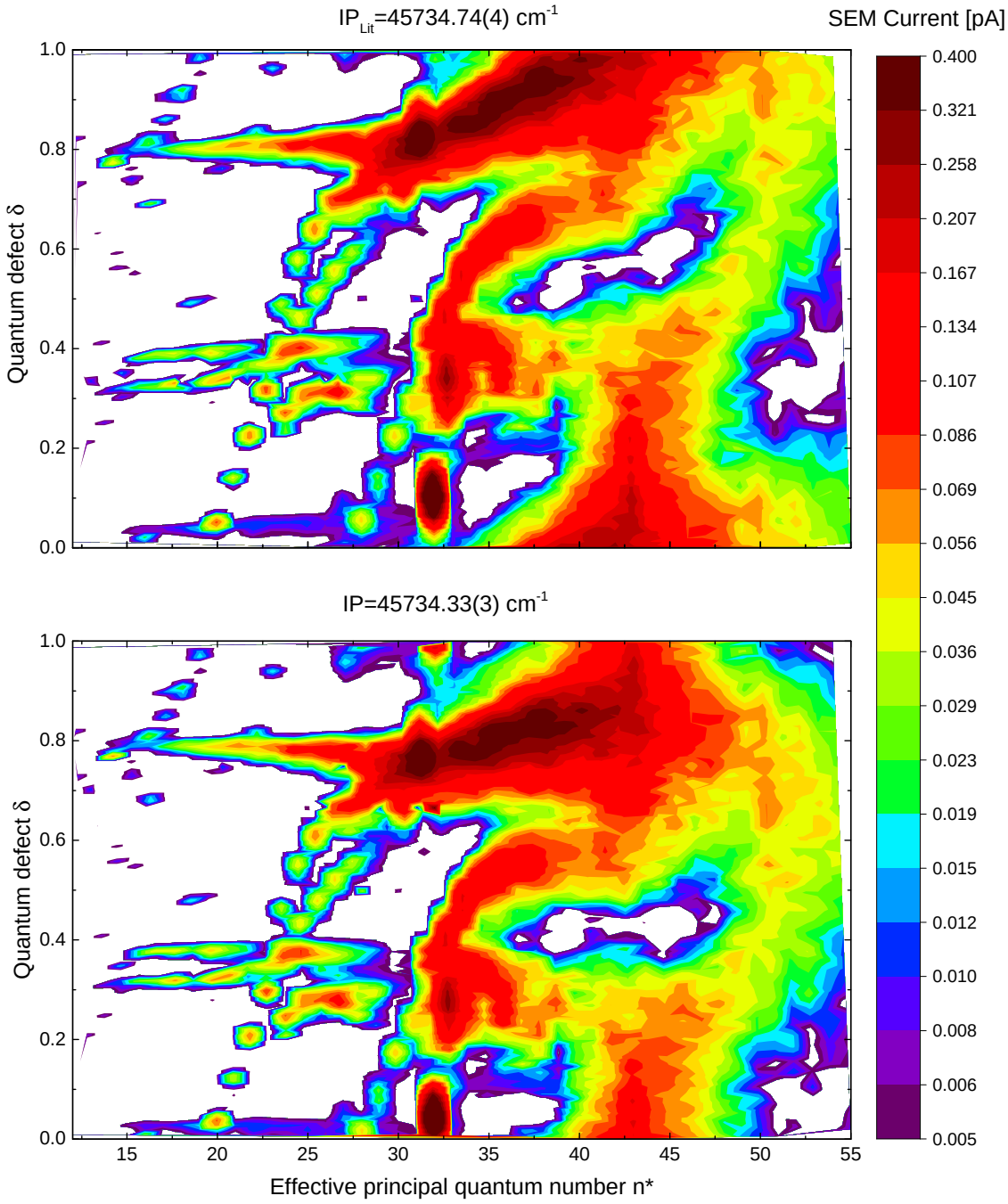

Figure 6.6: *The contour plot shows the fractional values for δ over n^* for the literature value of the IP with $E_{IP} = 45734.74(4)\,cm^{-1}$ and the value determined in this work $E_{IP} = 45734.33(3)\,cm^{-1}$. The convergence of the series towards constant values for δ can be better observed for the lower value, indicating that a correction of the current value for the IP might be needed.*

6.2 Ionization potential

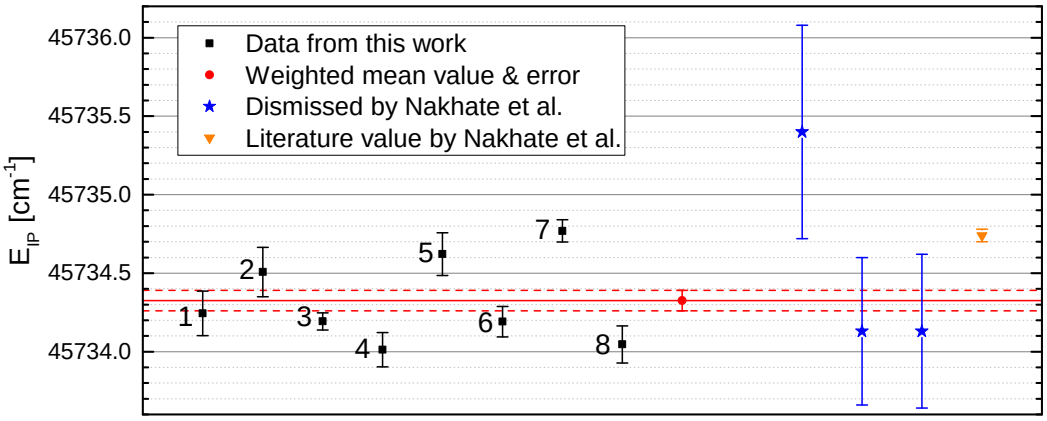

Figure 6.7: *Fitted IP values from this work, from left to right series 1 to 8 are given. The weighted mean value is indicated with the red line. The dotted red line gives the error of the mean value together with the wavemeter error, so that* $E_{IP} = 45734.33(3)(3)\,cm^{-1}$. *All values for the IP derived in [NRCA00] are indicated in the plot for a better overview.*

Using the data given in the work by Nakhate et al. in [NRCA00] a comparison between the current literature value and the value for the ionization potential derived in this work was made. Displayed in Figure 6.7 are the values of the series which have been determined from the data in this thesis and the values that were determined in [NRCA00]. It includes the data points that were dismissed by Nakhate et al. as they seem more perturbed. The comparison of these values show that in both works the value leading to the current literature value can be found. On the other hand nearly all other points that are shown deviate from the literature value towards a lower limit. Figure 6.7 includes the weighted mean value derived in this work with the corresponding error of the weighted mean and the wavemeter error ($E_{IP} = 45734.33(3)(3)\,\mathrm{cm}^{-1}$). Clearly the values of series 3 and 7 count most into the resulting value as they exhibit the smallest errors. Series 7 shows the biggest deviation from the weighted mean and lies far away from the confidence band, while all other series deviate less than $0.1\,\mathrm{cm}^{-1}$ from the weighted mean value. The reason for the big deviation of series 7, which agrees well with the current literature value, cannot be determined. It appears that the value for the ionization potential is dependent on the chosen Rydberg series and its exact limit. This is apparently not constant for the given data.
According to Nakhate et al. six strong Rydberg series should have been observed in their studies. As they used different first steps, J-values of $3/2$, $5/2$, $7/2$, $9/2$ and $11/2$ were possible according to the selection rules. Considering the ionization scheme applied for this work, only configurations with $J = 7/2, 9/2$ or $11/2$ were possible. In contrast to this earlier work no comparison between different states was possible in the present work

as only one ionization scheme was explored, so that the assignment was not possible by assigning the J-values. The evaluation of the data in [NRCA00] shows that it is advantageous to assign the J-values, which is why additional measurements should be made to complement the current status of this thesis. Not only would this method yield additional data points but the already obtained ones could be re-evaluated according to their J-value, which should lead to a more thorough analysis.
Figure 6.8 and Figure 6.9 show the data from the paper from Nakhate et al. The values for the quantum defect are plotted over the effective quantum numbers for the IP value determined in the previous work and for the IP determined in this work (see Table 6.2). In the older data there are clearly two trends that lead to two different values for the IP. The thesis at hand shows that there is a need for a clarification for the value of the first ionization potential of europium. A future task will therefore be to choose an adequate, different first step for additional Rydberg series measurements that could complement the current data.

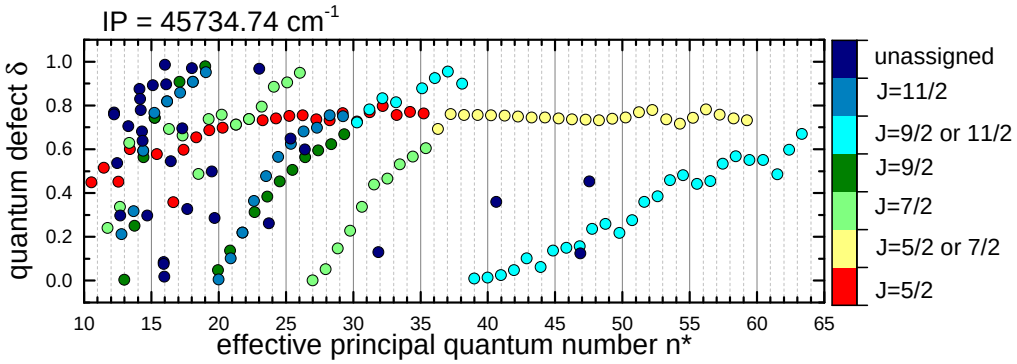

Figure 6.8: *The plotted data was extracted from [NRCA00]. It has been plotted here using the IP determined in the same paper. A clear trend can be seen for the $J = 5/2$-series.*

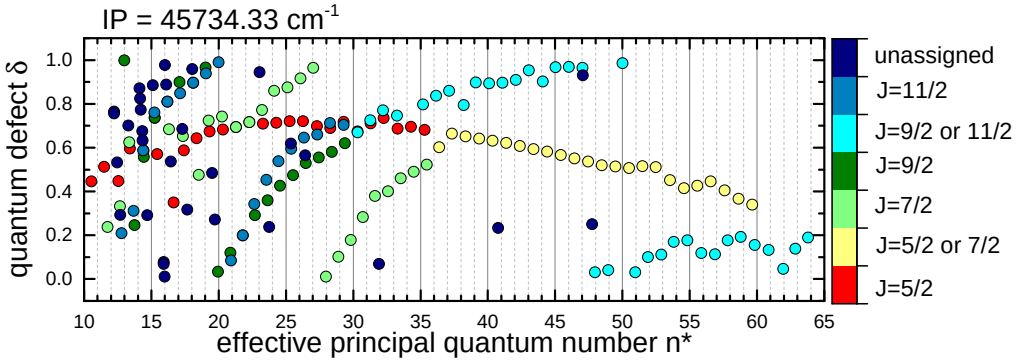

Figure 6.9: *The plotted data is the same as in Figure 6.8. It has been plotted for the newly determined value for the europium IP (see Table 6.2). The long $5/2$-series is dropping down here, indicating that it is not converging, whilst the other series (light blue $J = 9/2$ or $7/2$) show a trend towards a constant quantum defect.*

6.3 Rydberg series to a higher lying state of Eu II

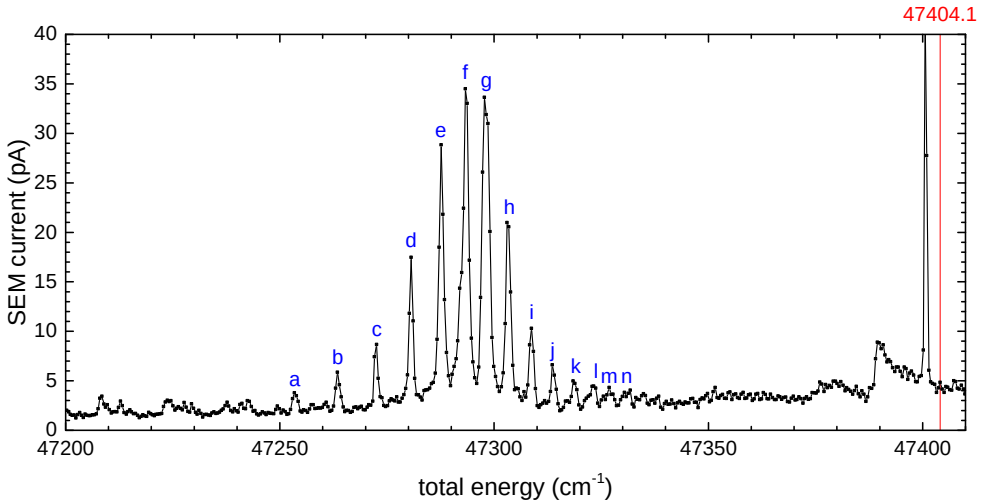

Figure 6.10: *Rydberg series to high lying state of EU II. The peaks that have been fitted are indicated by the letters a to n.*

As mentioned in the beginning of chapter 6 a second structure which resembles a Rydberg series (see Figure 6.10) was observed in the spectrum at about $1700\,\mathrm{cm}^{-1}$ above the IP. In NIST ([KYRa15]) a higher lying member of the ground state configuration, i.e. $4f^7 5p^6 6s\ {}^7S^o$ with $J = 3$, is tabulated at $1669.21\,\mathrm{cm}^{-1}$ together with the members $43 < n < 68$ of the Rydberg series $4f^7 6s\,np$ leading to it. Because of the parity restriction, the series observed in this thesis cannot belong to the np-series tabulated in the NIST database. In the paper [BDRR03] by S. Bhattachryya et al. some of the same energy levels as observed in this thesis were found. According to the evaluation of S. Bhattachryya et al. this leads to the conclusion that the levels observed here belong to a $J = 9/2$-series. Additionally many more levels were identified in [BDRR03]. The structure in [BDRR03] as well as the structures observed in this thesis look strongly perturbed. The quantum defect which has been calculated for a limit of $E_{\mathrm{limit}} = 47404.1\,\mathrm{cm}^{-1}$ (as observed e.g. in [ST76]) does not give a constant value but changes by $\Delta\delta > 1$ between the different energy levels (see Figure 6.11). A slight convergence towards a value with the fractional part of $\delta_{\mathrm{fractional}} \approx 0.2$ can be observed, so that it might be assumed that the series at hand is a s-series (with $\delta_s \approx 4.24$). This would then mean that the series members observed here have values of n lying in between $n = 28$ to 41. A fit was not attempted as the limited number of data points together with the strong perturbations would not lead to a conclusive result. The value of the first excited state of the Eu ion could therefore not be confirmed.

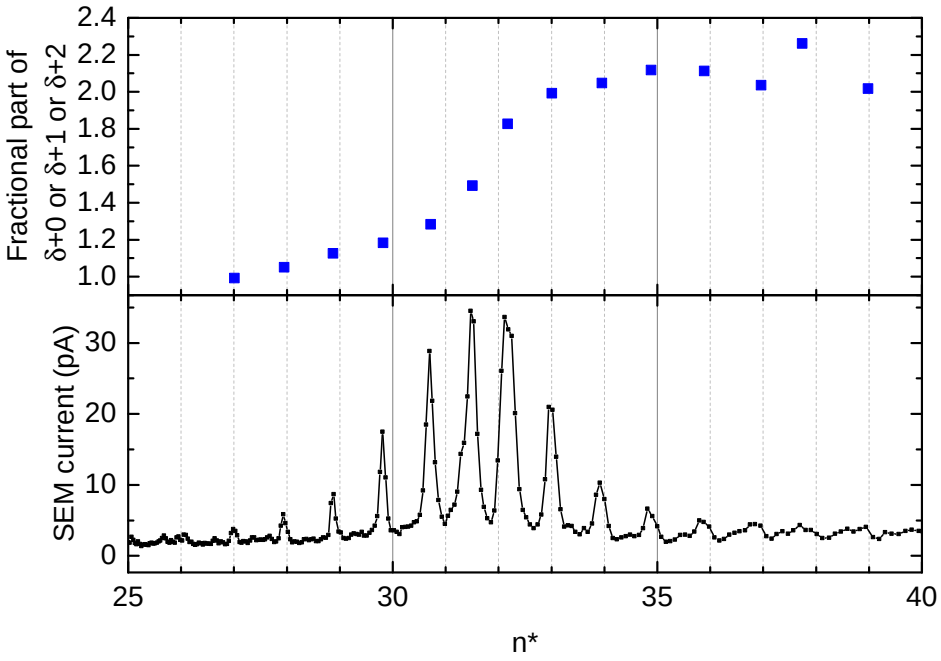

Figure 6.11: *Fractional part of δ, $\delta+1$ and $\delta+2$ over n^* for excited state of Eu I together with the ion current.*

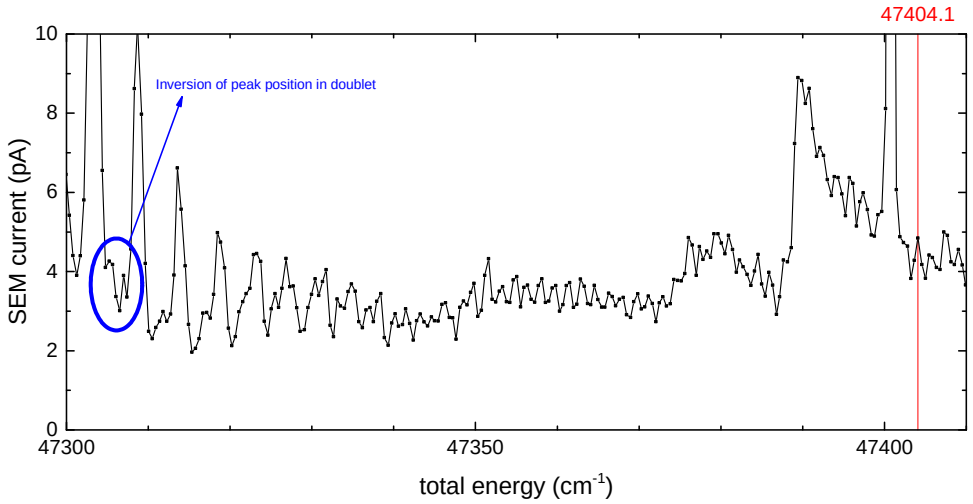

Figure 6.12: *Rydberg series to high lying state of EU II in more detail.*

In Figure 6.12 one can see that not only one but two series have been observed. There is

a doublet with one series being a lot stronger than the other one. A perturbation seems to invert/shift the strong series while going upwards in energy, so that it starts out as the left peak of the doublet and then changes to being the right peak in the doublet. This second interfering Rydberg series might be one of the reasons for the perturbations.

7 Conclusion and outlook

Overall the project was successful. The PISA was installed and fully integrated into the RILIS setup. Its future use will mainly include scheme development and monitoring during runs. As a long shut down is scheduled for the accelerators and therefore also ISOLDE in 2019, the RILIS lasers will be used for extensive scheme development. The PISA should be indispensable during this period. Developments towards two-photon spectroscopy (a high resolution, Doppler-free spectroscopy method) will be attempted, therefore new schemes for this method will have to be prepared and tested. The PISA offers the unique possibility of being transported easily, so that the tests might also be carried out using the lasers of other groups at ISOLDE with slightly different properties for additional tests.

The europium scheme development was fruitful. Many new autoionizing states were found, providing an ideal basis for finalizing the scheme development. Time for this finalization has been requested and will ideally take place during the beginning of 2017. Once the scheme development will be finalized, a very efficient scheme will be at hand, should the need arise. Tests together with ISOLTRAP (Penning trap setup at ISOLDE) will be carried out in order to fully determine the best scheme possible, regarding the efficiency as well as the contamination of the ion beam. Comparisons between resonant and non-resonant last steps will be made, leading to the best possible scheme not only for the RILIS set up but also for the users that will be provided with clean beams.

The Rydberg analysis of europium revealed some discrepancies between the literature value of the ionization potential ($45734.74(4)\,\mathrm{cm}^{-1}$) and the value of $45734.33(3)(3)\,\mathrm{cm}^{-1}$ derived in this work. As discussed in section 6.1 the characterization of the observed Rydberg series was difficult due to the lack of J-assignments. In order to resolve this difficulty, a further measurement, using an alternative ionization scheme, is anticipated. A comparison of the data obtained with each ionization scheme will enable J-assignments according to the selection rules for electric dipole transitions.

The use of the PISA as a reference cell for in-source spectroscopy experiments will remain as a future task. A more detailed analysis will have to be made regarding the detector performance and the low ion signal that was observed. The temperature restrictions will have to be eliminated for this cause, so that higher vapor pressures and accordingly higher ion signals will become feasible.

Further developments of the PISA are going to take place. The re-design of the oven has already started and will be build as soon as it is finalized. A new design of the ion optics is foreseen, making use of the Kimbal system, which provides easy tools for building such optics. The new design will be more versatile and adaptable, giving more possibilities on including different detectors and more refined optics.

8 Appendix

8.1 SEM data sheet

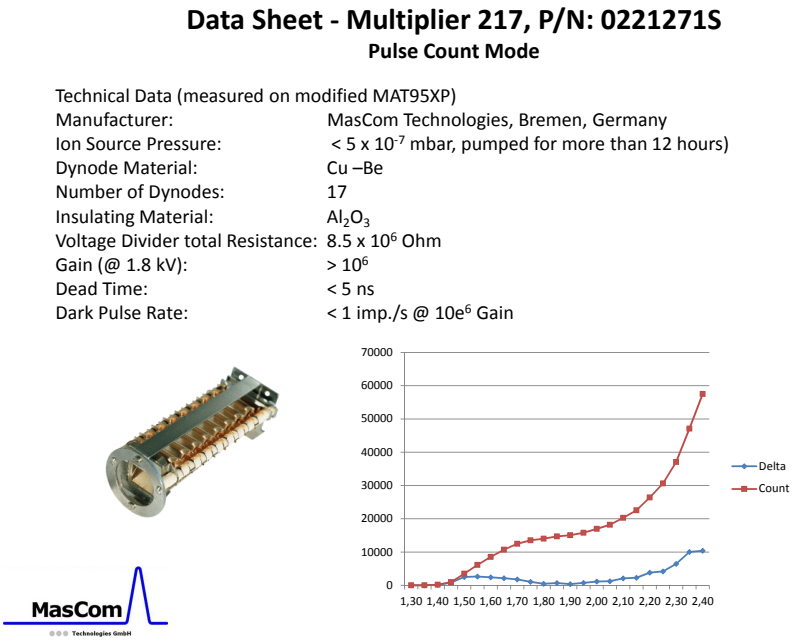

Figure 8.1: *The data sheet for the MC-217 from MasCom, from a private correspondence with Dr. H. Müller (executive director MasCom).*

8.2 Working principle of a secondary electron multiplier

A secondary electron multiplier is a detector with which single ions can be detected[1]. The front of the SEM sits on a high negative potential while the back is grounded. A singly charged particle is accelerated towards the front of the detector. When the first plate of the detector is hit, electrons are released. Those are accelerated by the high potential of the SEM towards more dynodes sitting between the front and end plate of the SEM. Each dynode acts as one amplification stage as every electron hitting it releases

[1] This section is based on [Leo94].

another multitude of electrons. This leads to an increase in current for each dynode, with electrons cascading towards the end plate comparable to an avalanche. Depending on the voltage applied to the SEM the gain differs. The higher the potential, the more the electrons are accelerated. This increase in kinetic energy leads to a higher release of electrons each time one of the electrons hits a dynode.

The equivalent circuit for an SEM is an ideal current source as depicted in Figure 8.2.

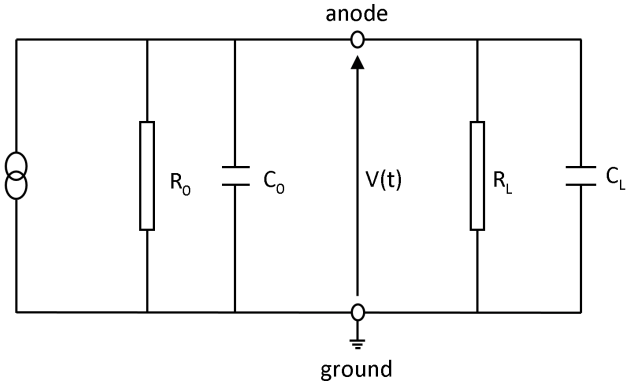

Figure 8.2: *Model of an ideal current source, representing the circuit for a secondary electron multiplier.*

The output voltage or current depends on the load resistance R_L and capacitance C_L in combination with the parallel output resistance R_0 and capacitance C_0. The time constance τ of the circuit is equal to $R \times C$ where

$$R = \frac{R_0 R_L}{R_0 + R_L} \qquad \text{and} \qquad C = C_0 + C_L \tag{8.1}$$

Assuming that the number of ions is N, the electronic charge e and the electron multiplier gain G, then the output current is defined by

$$I(t) = \frac{NeG}{\tau_s} \exp(-t/\tau_s) \tag{8.2}$$

and the output voltage by

$$V(t) = \frac{NegR}{\tau - \tau_s}[\exp(-t/\tau_s) - \exp(-t/\tau)] \tag{8.3}$$

For current mode operation $\tau \ll \tau_s$ is required, while voltage (single ion) mode requires $\tau \gg \tau_s$. The time constant τ needs to be adjusted according to the desired mode of the detector. This can normally be done externally via the resistance which can be adjusted in order to change the timing constant.

8.3 How to operate the PISA

As discussed in section 4.1 the setup of the PISA is a simple one which is more or less intuitive to use. Some basic steps for operating it are described here:

Sample switching

- turn off vacuum pump and let it spin down completely
- open the pressure valve (opposite to vacuum pump)
- open up the flange on which the oven assembly is mounted
- extract old sample and put in the new one
- if the oven material is supposed to be changed: remove thin metal plate holding oven tip, take out oven and replace; screw the metal plate back on, the oven should be fixed by the hole in the center of the plate
- put flange back on
- close vacuum valve
- start the pump and wait for pressure to go down to at least 10^{-6} mBar before operating the PISA

Finding the right settings

- check pressure, if not in order of 10^{-6} mBar wait for it to go down
- switch on the power supplies for the electrodes and the SEM
- start the readout program for the Keithley from the RILIS shortcuts (gives ion current over time)
- check if the vacuum gauge is on: there should be a negative current read out by the Keithley as soon as all electrodes have reached their setpoints
- heat the oven by slowly ramping up the current on the power supply (first estimation about the required temperature should be made using the data on vapor pressures provided in [RS95]; the temperature calibration for the oven can be found in subsubsection 4.4.1.1)
- switch off vacuum gauge once desired temperature has been reached: If there is no laser ionization yet, the signal of the SEM should go down to 0 A
- heat the oven in small steps ($0.5 - 1$ A steps); after each step the system should be given approx $5 - 10$ minutes to settle
- scan laser beam positions until first signal is seen
- first signal detected: optimize laser beam position
- then optimize the electrodes (steps of 10 V), leave repeller at 9 V (optimal setting for all tests), do not go above 2 kV with SEM (unless pressure is $< 10^{-5}$ mBar)

8.4 Possible first step transitions for Eu ionization scheme

The table shown here includes all possible first step transitions found in literature for an Eu ionization scheme. The first horizontal line indicates that for all first steps above it, no scans for AIS could have been performed with the available lasers. The second horizontal line indicates that for all steps below it scans would have been very difficult, as the available lasers would have to be frequency doubled, making a wavelength scan very complicated. All steps in the middle section are possible first steps where scans for AIS can be performed with the available lasers. Steps where the A-value (proportional to the transition strength) was below 10^7 1/s were not considered, as well as steps that have a transition of J-1, as those are considered to be less efficient ([FY84]). From the remaining first steps the only transition with a J+1 was chosen.

WI (nm)	A-value (1/s)	J_{lower}	E_{upper} (cm^{-1})	J_{upper}	comments	to IP (cm^{-1})	to IP (nm)
237.28	$2.07E+07$	3.5	42130.72	2.5	J-1	3603.28	2775.24
237.53	$2.24E+07$	3.5	42087.02	3.5		3646.98	2741.99
237.74	$5.64E+06$	3.5	42048.40	4.5	A-value$< E+07$	3685.6	2713.26
237.96	$2.14E+07$	3.5	42010.25	4.5		3723.75	2685.46
238.92	$3.00E+06$	3.5	41841.47	4.5	A-value$< E+07$	3892.53	2569.02
241.84	$5.13E+06$	3.5	41335.67	3.5	A-value$< E+07$	4398.33	2273.59
242.50	$2.96E+06$	3.5	41223.58	3.5	A-value$< E+07$	4510.42	2217.08
244.05	$1.77E+06$	3.5	40962.39	4.5	A-value$< E+07$	4771.61	2095.72
244.64	$7.83E+05$	3.5	40862.41	3.5	A-value$< E+07$	4871.59	2052.71
246.05	$5.72E+06$	3.5	40629.82	2.5	A-value$< E+07$	5104.18	1959.17
246.17	$5.28E+06$	3.5	40609.30	3.5	A-value$< E+07$	5124.7	1951.33
247.11	$1.04E+07$	3.5	40455.51	4.5		5278.49	1894.48
256.49	$1.22E+06$	3.5	38975.14	4.5	A-value$< E+07$	6758.86	1479.53
256.87	$8.15E+05$	3.5	38917.74	3.5	A-value$< E+07$	6816.26	1467.08
258.06	$7.99E+05$	3.5	38738.78	2.5	A-value$< E+07$	6995.22	1429.54
260.25	$5.89E+05$	3.5	38411.83	3.5	A-value$< E+07$	7322.17	1365.71
260.60	$3.14E+05$	3.5	38360.67	4.5	A-value$< E+07$	7373.33	1356.23
261.92	$7.77E+05$	3.5	38167.16	4.5	A-value$< E+07$	7566.84	1321.55
262.57	$5.78E+05$	3.5	38072.67	3.5	A-value$< E+07$	7661.33	1305.25
263.16	$5.39E+05$	3.5	37988.09	4.5	A-value$< E+07$	7745.91	1291.00
263.71	$5.37E+05$	3.5	37908.94	4.5	A-value$< E+07$	7825.06	1277.94
264.10	$4.76E+05$	3.5	37851.77	3.5	A-value$< E+07$	7882.23	1268.67
264.38	$6.67E+05$	3.5	37812.80	3.5	A-value$< E+07$	7921.2	1262.43
265.94	$1.28E+06$	3.5	37591.21	4.5	A-value$< E+07$	8142.79	1228.08
268.25	$1.36E+06$	3.5	37266.36	2.5	A-value$< E+07$	8467.64	1180.96
269.27	$4.40E+05$	3.5	37126.08	4.5	A-value$< E+07$	8607.92	1161.72
269.50	$6.09E+05$	3.5	37093.81	2.5	A-value$< E+07$	8640.19	1157.38
270.99	$1.45E+07$	3.5	36889.62	4.5		8844.38	1130.66
272.39	$1.26E+07$	3.5	36700.39	3.5		9033.61	1106.97
273.13	$3.40E+06$	3.5	36600.83	3.5	A-value$< E+07$	9133.17	1094.91
273.26	$4.05E+06$	3.5	36584.31	2.5	A-value$< E+07$	9149.69	1092.93
273.52	$5.13E+06$	3.5	36548.88	4.5	A-value$< E+07$	9185.11	1088.71
273.85	$1.35E+06$	3.5	36504.61	4.5	A-value$< E+07$	9229.39	1083.49
274.32	$1.13E+07$	3.5	36441.77	2.5	J-1	9292.23	1076.16
274.56	$5.43E+06$	3.5	36410.96	2.5	A-value$< E+07$	9323.04	1072.61
274.78	$5.65E+06$	3.5	36381.51	3.5	A-value$< E+07$	9352.49	1069.23
277.29	$1.15E+06$	3.5	36052.65	2.5	A-value$< E+07$	9681.35	1032.91
277.65	$7.78E+05$	3.5	36005.73	3.5	A-value$< E+07$	9728.27	1027.93

287.77	$8.37E+05$	3.5	34738.82	4.5	A-value$< E+07$	10995.18	909.48
287.88	$3.02E+06$	3.5	34725.81	4.5	A-value$< E+07$	11008.19	908.41
289.25	$1.12E+07$	3.5	34561.87	3.5		11172.13	895.08
289.30	$1.05E+07$	3.5	34555.82	2.5	J-1	11178.18	894.60
289.38	$1.59E+06$	3.5	34546.06	4.5	A-value$< E+07$	11187.94	893.81
290.89	$7.52E+06$	3.5	34366.13	4.5	A-value$< E+07$	11367.87	879.67
295.08	$6.08E+05$	3.5	33879.16	4.5	A-value$< E+07$	11854.84	843.53
295.88	$1.73E+06$	3.5	33786.55	2.5	A-value$< E+07$	11947.45	836.99
305.89	$4.14E+06$	3.5	32681.13	3.5	A-value$< E+07$	13052.87	766.11
306.69	$9.65E+05$	3.5	32596.31	4.5	A-value$< E+07$	13137.69	761.16
308.56	$1.39E+05$	3.5	32398.25	3.5	A-value$< E+07$	13335.75	749.86
310.61	$6.07E+06$	3.5	32184.65	4.5	A-value$< E+07$	13549.35	738.04
311.14	$\mathbf{3.20E+07}$	**3.5**	**32130.25**	**4.5**	**J+1**	**13603.75**	**735.09**
316.82	$7.97E+05$	3.5	31553.76	4.5	A-value$< E+07$	14180.24	705.20
318.55	$6.27E+05$	3.5	31382.61	4.5	A-value$< E+07$	14351.39	696.79
321.05	$1.23E+07$	3.5	31138.11	3.5		14595.89	685.12
321.28	$3.16E+07$	3.5	31116.38	3.5		14617.62	684.10
321.37	$1.98E+07$	3.5	31107.28	2.5	J-1	14626.72	683.68
323.51	$1.12E+06$	3.5	30901.84	4.5	A-value$< E+07$	14832.16	674.21
324.13	$2.47E+06$	3.5	30841.99	3.5	A-value$< E+07$	14892.01	671.50
324.60	$1.60E+06$	3.5	30798.06	2.5	A-value$< E+07$	14935.94	669.52
324.75	$2.56E+06$	3.5	30783.64	3.5	A-value$< E+07$	14950.36	668.88
326.24	$3.00E+05$	3.5	30642.61	4.5	A-value$< E+07$	15091.39	662.62
332.22	$3.78E+06$	3.5	30091.34	2.5	A-value$< E+07$	15642.66	639.27
333.43	$3.76E+07$	3.5	29982.50	2.5	J-1	15751.5	634.86
335.04	$1.56E+06$	3.5	29838.59	4.5	A-value$< E+07$	15895.41	629.11
335.37	$5.89E+05$	3.5	29809.23	3.5	A-value$< E+07$	15924.77	627.95
343.25	$4.51E+05$	3.5	29124.78	2.5	A-value$< E+07$	16609.22	602.07
345.70	$8.98E+05$	3.5	28918.17	3.5	A-value$< E+07$	16815.83	594.67
346.78	$1.10E+06$	3.5	28827.83	3.5	A-value$< E+07$	16906.17	591.50
358.92	$7.69E+05$	3.5	27852.90	2.5	A-value$< E+07$	17881.1	559.24
459.40	$1.52E+08$	3.5	21761.26	4.5	2nd steps exist	23972.74	417.14
462.72	$1.49E+08$	3.5	21605.17	3.5	2nd steps exist	24128.83	414.44
466.18	$1.43E+08$	3.5	21444.58	2.5	2nd steps exist	24289.42	411.70
564.57	$7.80E+05$	3.5	17707.42	2.5	A-value$< E+07$	28026.58	356.80
576.51	$1.17E+06$	3.5	17340.65	3.5	A-value$< E+07$	28393.35	352.19
601.81	$9.42E+05$	3.5	16611.79	4.5	A-value$< E+07$	29122.21	343.38
626.69	$6.71E+04$	3.5	15952.31	3.5	A-value$< E+07$	29781.69	335.77
629.13	$2.03E+05$	3.5	15890.53	2.5	A-value$< E+07$	29843.47	335.08
686.45	$7.99E+05$	3.5	14563.57	4.5	A-value$< E+07$	31170.43	320.81
710.64	$2.91E+05$	3.5	14067.86	3.5	A-value$< E+07$	31666.14	315.79

Table 8.1: *Possible first steps for Eu ionization scheme from literature (Kuruzc database [kur]).*

8.5 Wavelength scans for Eu AIS

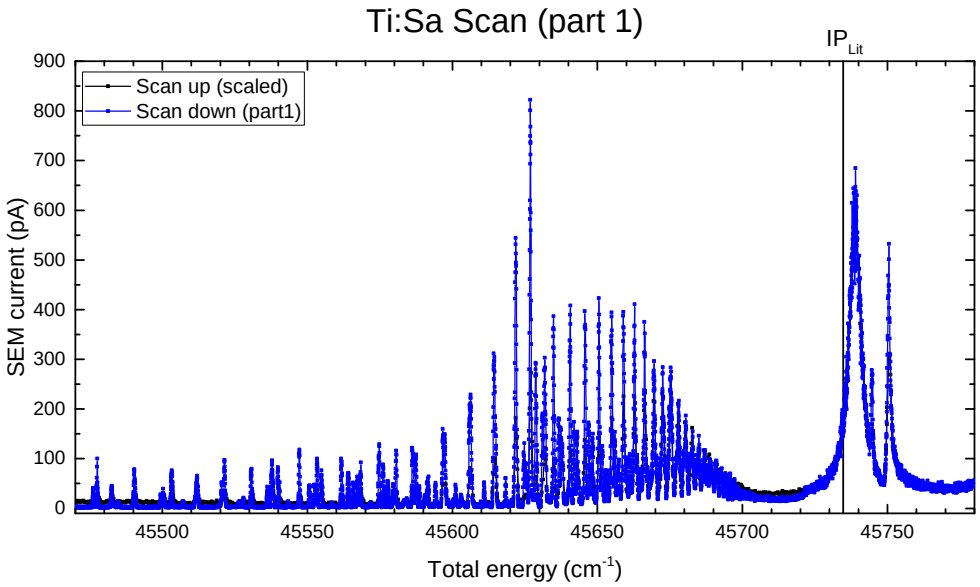

Figure 8.3: *Ti:Sa scan with a scan range of* $733 - 750\,nm$*, the scan has been parted in two graphs for better depiction*

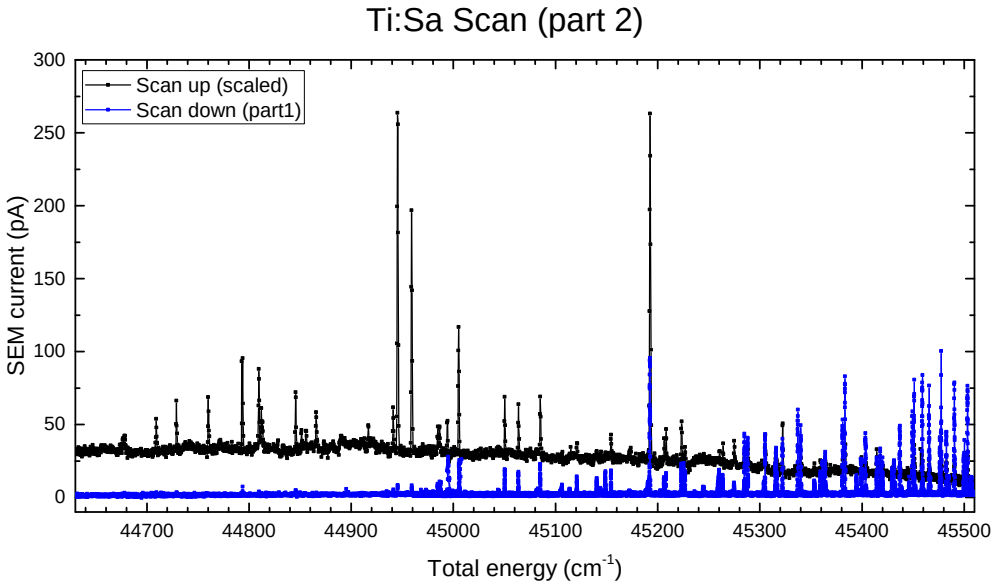

Figure 8.4: *Ti:Sa scan with a scan range of* $747 - 800\,nm$

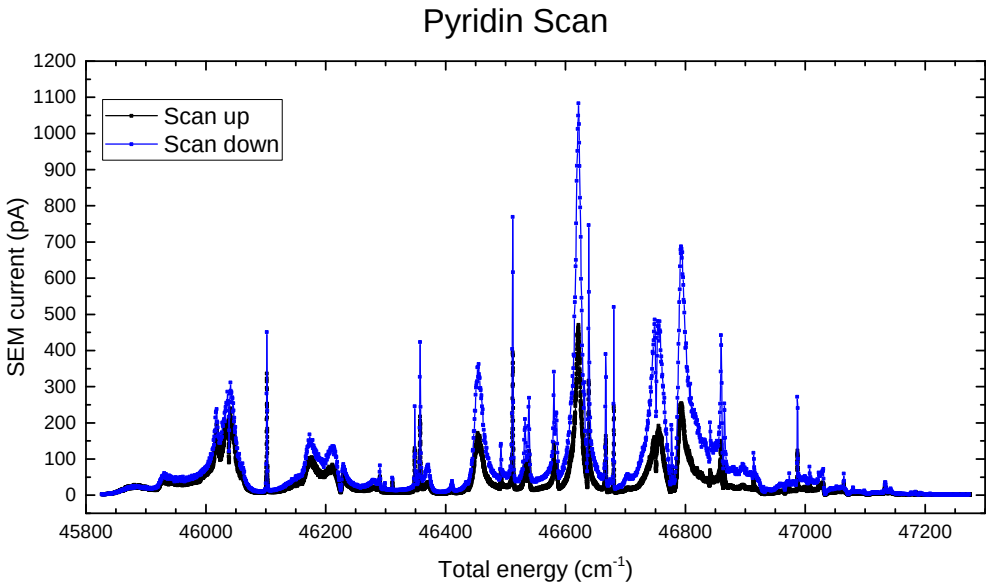

Figure 8.5: *Pyridin 1 scan with a scan range of* $660 - 730\,nm$

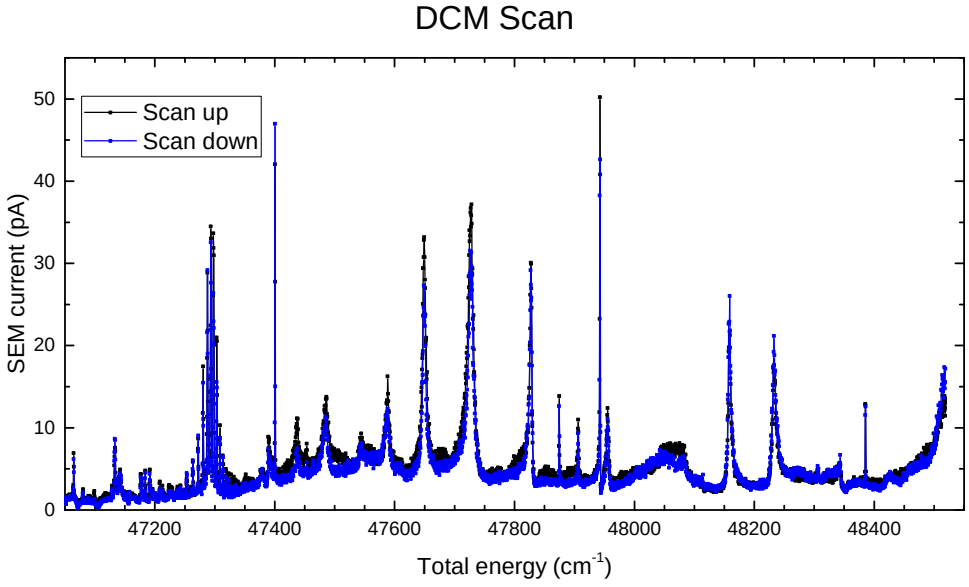

Figure 8.6: *DCM scan with a scan range of* $610 - 670\,nm$

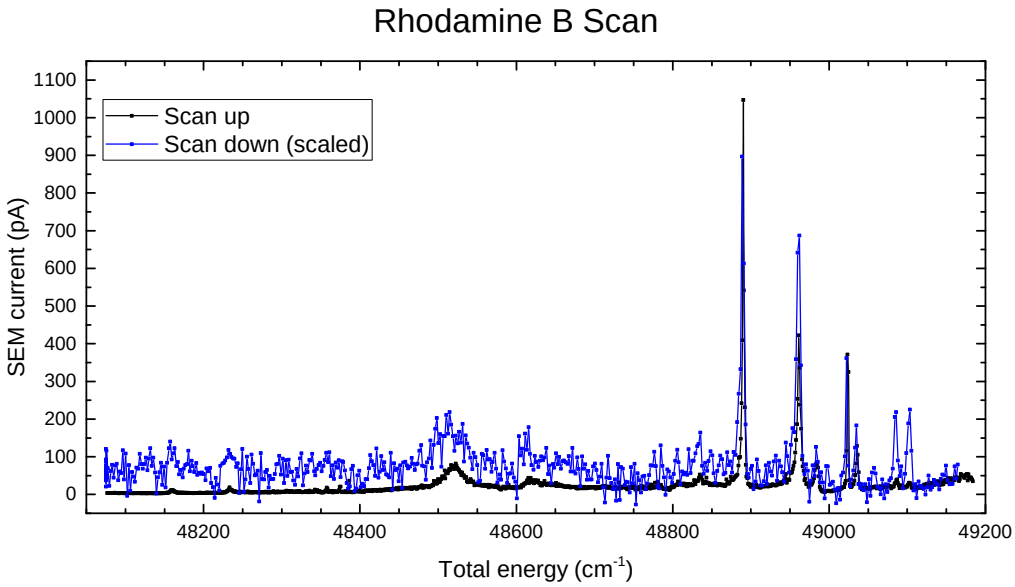

Figure 8.7: *Rhodamine B scan with a scan range of* $586 - 627\,nm$

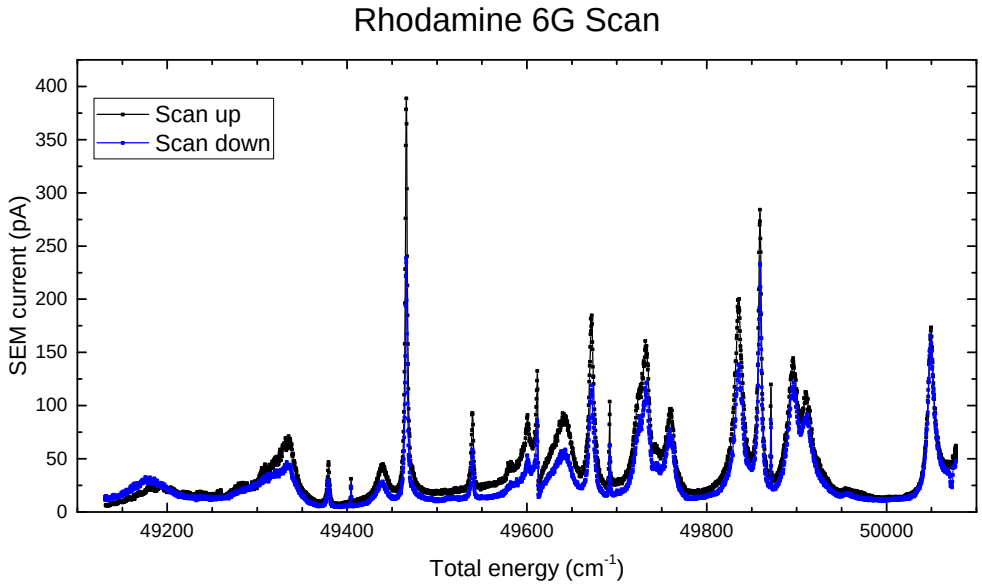

Figure 8.8: *Rhodamine 6G scan with a scan range of* $557 - 588\,nm$

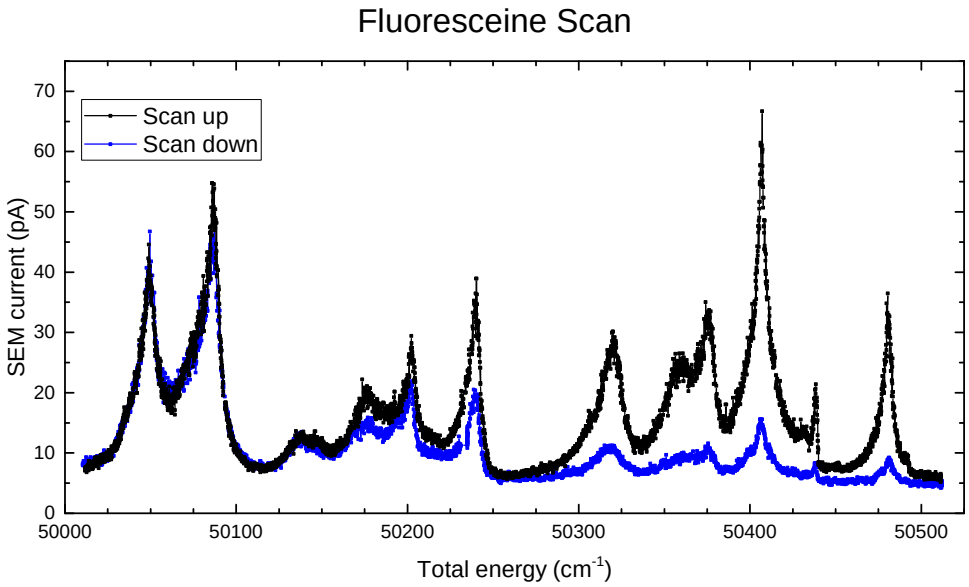

Figure 8.9: *Fluoresceine 548 scan with a scan range of* $544 - 559$ *nm*

Table 8.2: *Autoionizing states of europium. The bold characters indicate that the AIS were found in two different spectra.*

Total energy [cm^{-1}]	Error [cm^{-1}]
45738.64	0.08
45744.97	0.09
45750.38	0.07
45786.10	0.15
45788.17	0.11
45789.56	0.11
45870.47	**0.37**
45926.76	**0.31**
46017.26	**0.31**
46037.23	**0.54**
46041.45	1.01
45867.84	**0.85**
45924.11	**0.30**
46017.30	**0.21**
46038.78	**0.21**
46102.01	0.06

46170.83	0.23
46220.14	0.30
46227.75	0.20
46290.72	0.07
46298.87	0.05
46311.52	0.06
46348.62	0.05
46351.24	0.06
46357.66	0.05
46371.43	0.23
46453.20	0.11
46492.17	0.08
46512.17	0.04
46532.63	0.13
46539.20	0.07
46580.78	0.11
46585.57	0.19
46621.96	0.11
46631.93	0.07
46638.69	0.06
46667.48	0.06
46680.78	0.05
46751.81	0.32
46750.80	0.76
46776.98	0.06
46790.66	0.10
46841.21	0.07
46860.40	0.07
46865.19	0.06
46913.81	0.06
46987.08	0.05
47007.38	0.07
47030.96	0.12
47064.66	**0.06**
47080.20	**0.08**
47133.47	**0.06**
47064.64	**0.08**
47080.12	**0.11**
47128.78	0.06
47133.46	**0.12**
47142.79	0.32
47154.16	0.10

47184.27	0.07
47191.67	0.14
47196.78	0.10
47253.65	0.08
47263.63	0.07
47272.47	0.06
47280.68	0.07
47287.80	0.08
47293.56	0.08
47298.08	0.10
47303.38	0.09
47308.90	0.09
47313.91	0.09
47318.90	0.15
47323.78	0.14
47400.86	0.08
47437.39	0.16
47485.28	0.24
47588.44	0.23
47649.53	0.10
47727.03	0.14
47828.02	0.14
47874.77	0.15
47906.28	0.12
47942.89	0.07
47955.48	0.13
48158.51	**0.11**
48232.61	**0.12**
48385.72	0.14
48159.19	**0.34**
48232.77	**0.40**
48357.74	0.22
48375.09	**0.10**
48386.38	0.23
48518.74	0.89
48890.40	0.08
48961.62	0.12
48985.61	0.34
49024.06	0.08
49035.70	0.14
49085.44	0.32
49103.50	0.21

49379.32	0.10
49404.55	0.07
49437.88	0.22
49465.86	0.09
49539.51	0.08
49600.31	0.18
49611.97	0.08
49642.45	0.36
49671.94	0.09
49691.98	0.08
49724.45	0.96
49734.51	0.22
49760.92	0.17
49835.60	0.14
49859.53	0.08
49871.43	0.09
49895.05	0.21
49913.49	0.35
50048.16	**0.11**
50049.23	**0.10**
50088.40	0.11
50139.35	0.25
50175.26	0.21
50203.37	0.12
50240.71	0.11
50320.45	0.17
18222.99	0.03
50375.86	0.16
50406.94	0.10
50438.91	0.09
50481.33	0.11

8.6 Rydberg states and series fits

Total energy [cm^{-1}]	Total energy [cm^{-1}]	Total energy [cm^{-1}]
44548.29 ± 0.04	45417.78 ± 0.04	45594.27 ± 0.07
44561.79 ± 0.08	45418.54 ± 63407.32	45596.76 ± 0.05
44565.06 ± 0.11	45419.91 ± 0.04	45597.30 ± 0.08
44677.09 ± 0.24	45420.38 ± 0.06	45597.72 ± 2.26
44678.44 ± 0.09	45429.47 ± 0.06	45600.40 ± 0.04
44709.24 ± 0.05	45429.96 ± 0.19	45601.15 ± 0.04
44729.00 ± 0.04	45431.20 ± 0.07	45603.06 ± 0.05
44760.43 ± 0.05	45432.22 ± 0.04	45603.87 ± 0.08
44793.70 ± 0.04	45437.01 ± 0.03	45605.82 ± 0.05
44809.78 ± 0.04	45437.48 ± 0.07	45606.31 ± 0.06
44811.98 ± 0.05	45438.47 ± 0.06	45609.86 ± 0.04
44813.11 ± 0.06	45446.07 ± 0.04	45610.98 ± 0.03
44845.77 ± 0.04	45449.28 ± 0.04	45614.52 ± 0.06
44851.53 ± 0.06	45449.74 ± 0.05	45614.97 ± 0.07
44855.91 ± 0.06	45451.02 ± 0.06	45618.43 ± 0.07
44865.91 ± 0.05	45452.19 ± 0.11	45621.91 ± 0.06
44916.87 ± 0.06	45459.03 ± 0.06	45624.70 ± 0.04
44941.20 ± 0.06	45465.77 ± 0.07	45625.34 ± 0.05
44945.51 ± 0.03	45466.14 ± 0.04	45625.92 ± 0.10
44959.29 ± 0.04	45466.83 ± 0.05	45626.97 ± 0.06
44984.76 ± 0.06	45476.13 ± 0.05	45628.79 ± 0.07
44986.54 ± 0.06	45476.49 ± 0.18	45631.01 ± 0.04
44994.25 ± 0.05	45477.29 ± 0.07	45631.89 ± 0.06
45005.21 ± 0.04	45477.49 ± 0.07	45634.97 ± 0.06
45043.91 ± 0.11	45481.67 ± 0.06	45636.71 ± 0.04
45044.51 ± 0.16	45482.64 ± 0.06	45637.41 ± 0.09
45050.39 ± 0.06	45483.48 ± 0.07	45637.93 ± 0.08
45063.74 ± 0.03	45484.83 ± 0.05	45640.64 ± 0.06
45081.75 ± 0.06	45485.45 ± 0.10	45642.05 ± 0.04
45082.87 ± 0.06	45490.45 ± 0.06	45642.83 ± 0.23
45085.11 ± 0.06	45499.50 ± 0.04	45643.13 ± 0.07
45105.06 ± 0.07	45500.39 ± 0.06	45643.55 ± 0.06
45106.25 ± 0.04	45500.90 ± 0.04	45645.81 ± 0.06
45113.91 ± 0.04	45501.86 ± 0.10	45647.08 ± 0.04
45116.96 ± 1.39	45503.33 ± 0.06	45648.33 ± 0.07
45120.92 ± 0.03	45504.71 ± 0.12	45648.49 ± 0.05
45140.41 ± 0.04	45507.13 ± 0.05	45650.59 ± 0.06
45144.01 ± 0.06	45512.03 ± 0.06	45651.72 ± 0.04
45148.79 ± 0.03	45519.70 ± 0.10	45652.72 ± 0.07
45154.38 ± 0.06	45520.48 ± 0.04	45653.09 ± 0.09

45188.38 ± 0.06	45520.91 ± 0.04	45654.99 ± 0.06
45190.39 ± 0.04	45521.49 ± 0.06	45656.05 ± 0.05
45192.50 ± 0.06	45526.45 ± 0.07	45656.95 ± 0.04
45192.71 ± 0.05	45527.98 ± 0.04	45657.39 ± 0.07
45202.70 ± 0.05	45530.78 ± 0.06	45659.06 ± 0.06
45206.16 ± 0.03	45531.07 ± 0.07	45660.05 ± 0.06
45207.47 ± 1.71	45536.26 ± 0.04	45661.20 ± 0.03
45208.18 ± 0.06	45537.93 ± 0.06	45662.27 ± 0.43
45223.34 ± 0.06	45540.00 ± 0.06	45662.84 ± 0.06
45225.52 ± 0.03	45540.43 ± 0.03	45663.69 ± 0.07
45226.84 ± 0.06	45543.46 ± 0.06	45665.16 ± 0.08
45244.78 ± 0.05	45547.33 ± 0.06	45665.59 ± 0.55
45258.95 ± 0.05	45550.82 ± 0.04	45666.33 ± 0.06
45259.51 ± 0.04	45552.51 ± 0.04	45667.10 ± 0.09
45260.06 ± 0.04	45553.39 ± 0.06	45668.51 ± 0.11
45262.13 ± 0.04	45554.60 ± 0.04	45669.57 ± 0.06
45263.60 ± 0.04	45554.97 ± 0.06	45670.36 ± 0.06
45264.03 ± 0.06	45558.50 ± 0.07	45671.45 ± 0.06
45273.33 ± 0.05	45561.87 ± 0.06	45672.59 ± 0.06
45274.78 ± 0.04	45564.22 ± 0.06	45673.47 ± 0.00
45275.10 ± 0.06	45565.89 ± 0.06	45675.28 ± 0.06
45284.96 ± 0.03	45567.30 ± 0.07	45677.21 ± 0.08
45285.11 ± 0.10	45567.74 ± 0.04	45678.00 ± 0.06
45288.13 ± 0.06	45568.41 ± 0.06	45679.65 ± 0.05
45304.12 ± 0.05	45568.92 ± 0.06	45680.47 ± 0.06
45305.23 ± 0.06	45571.79 ± 0.04	45681.95 ± 0.05
45315.25 ± 0.04	45574.86 ± 0.06	45682.76 ± 0.07
45315.89 ± 0.07	45575.11 ± 0.08	45684.18 ± 0.06
45316.61 ± 0.05	45576.22 ± 0.06	45684.96 ± 0.07
45322.26 ± 0.06	45576.41 ± 0.11	45686.99 ± 0.06
45337.12 ± 0.03	45577.84 ± 0.04	45688.02 ± 0.05
45340.08 ± 0.03	45579.67 ± 0.08	45688.65 ± 0.06
45353.35 ± 0.04	45580.05 ± 0.05	45689.01 ± 0.06
45359.18 ± 0.04	45580.71 ± 0.06	45689.78 ± 0.08
45361.17 ± 0.03	45583.35 ± 0.05	45690.52 ± 0.08
45362.67 ± 0.04	45584.27 ± 0.04	45690.90 ± 0.06
45363.85 ± 0.04	45586.13 ± 0.04	45691.58 ± 0.08
45380.96 ± 0.04	45586.35 ± 0.06	45692.42 ± 0.09
45382.80 ± 0.53	45586.47 ± 0.05	45692.87 ± 0.25
45383.41 ± 0.06	45587.46 ± 0.06	45693.55 ± 0.10
45394.61 ± 0.04	45587.95 ± 0.04	45694.07 ± 0.07
45398.99 ± 0.04	45588.68 ± 0.04	45694.49 ± 0.12
45399.54 ± 0.07	45589.09 ± 0.12	45695.83 ± 0.07
45403.34 ± 0.04	45590.59 ± 0.05	45697.18 ± 0.04

45403.76 ± 0.06	45591.31 ± 0.07	45698.49 ± 0.05
45404.09 ± 0.06	45591.60 ± 0.04	45699.42 ± 0.17
45414.41 ± 0.06	45591.87 ± 0.04	

Table 8.3: *The table shows all Rydberg states that were found and used for the analysis.*

Series 1

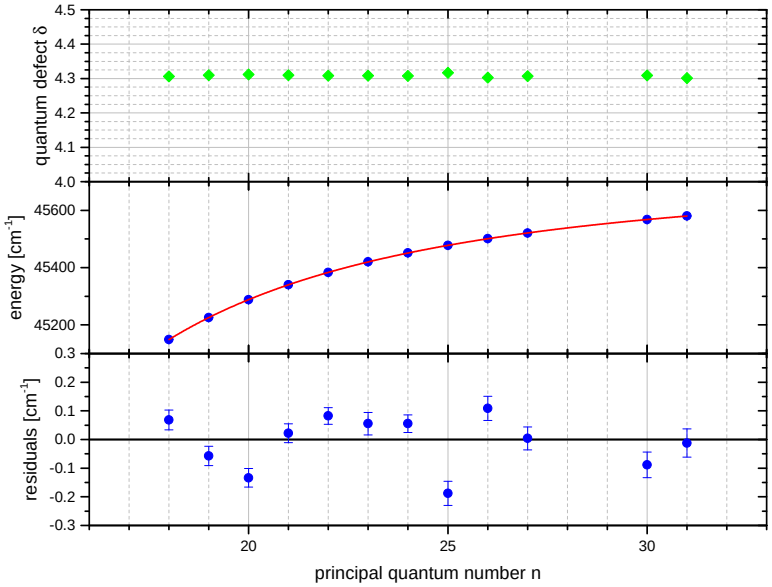

Figure 8.10: *Series 1,* $IP_{fit} = 45734.24(14)\, cm^{-1}$

Series 2

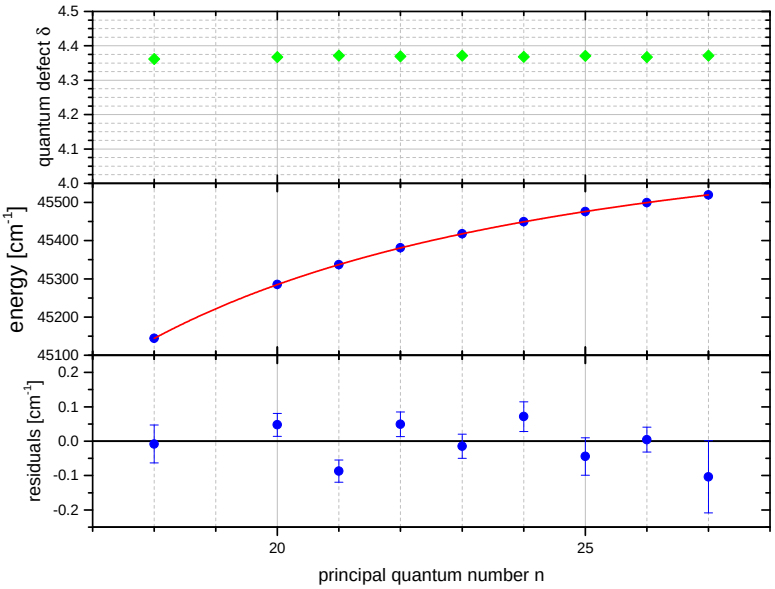

Figure 8.11: *Series 2,* $IP_{fit} = 45734.51(16)\ cm^{-1}$

Series 3

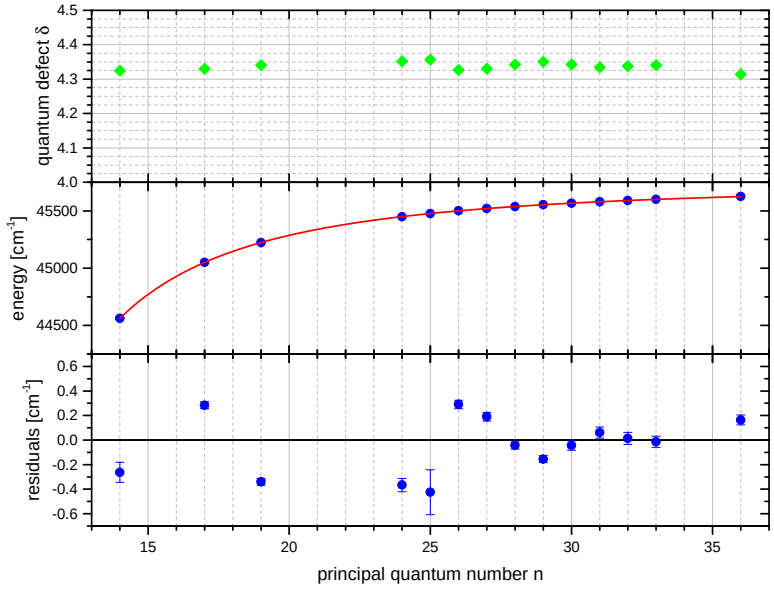

Figure 8.12: *Series 3,* $IP_{fit} = 45734.05(12)\ cm^{-1}$

Series 4

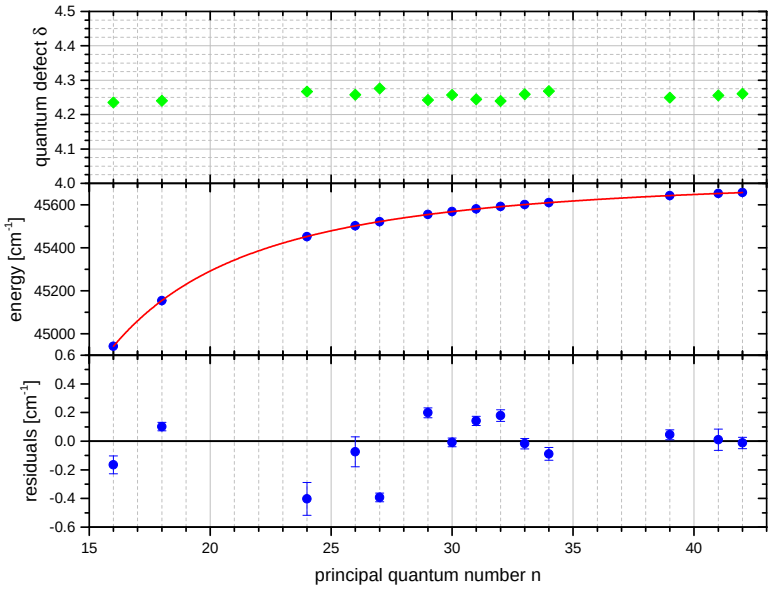

Figure 8.13: *Series 4*, $IP_{fit} = 45734.01(11)\,cm^{-1}$

Series 5

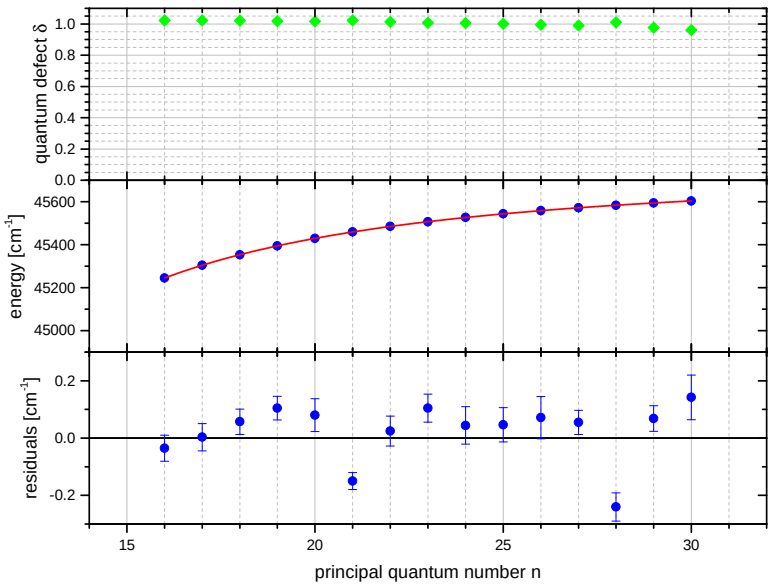

Figure 8.14: *Series 5*, $IP_{fit} = 45734.62(14)\,cm^{-1}$

Series 6

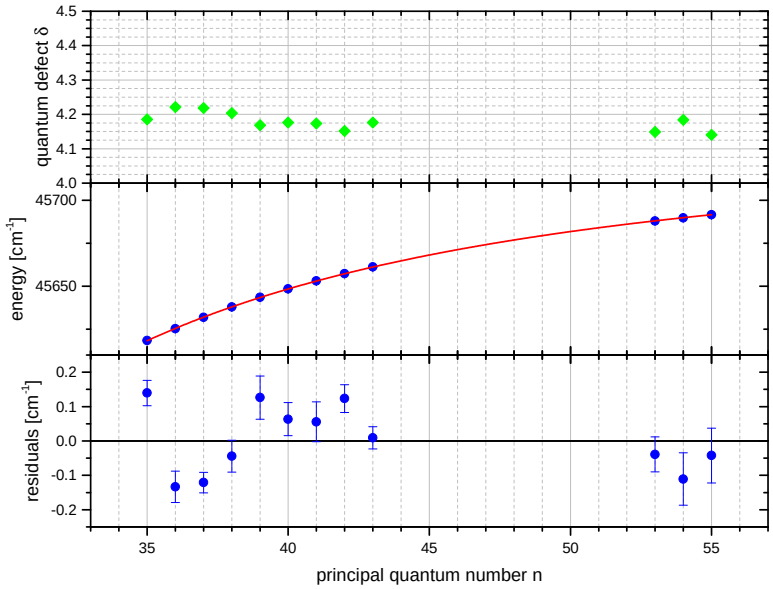

Figure 8.15: *Series 6, $IP_{fit} = 45734.19(10)\ cm^{-1}$*

Bibliography

[ABB+83] G.D. Alkhazov, A.E. Barzakh, É.I. Berlovich, V.P. Denisov, A.G. Dernyatin, V.S. Ivanov, A.N. Zherikhin, O.N. Kompanets, V.S. Letokhov, V.I. Mishin, and V.N. Fedoseev.
Measurement of isotropic variations in the charge radii of europium nuclei by the method of three-stepped laser photoionization of atoms.
JETP Lett., 37(5):274–278, 1983.

[ABB+84] G.D. Alkhazov, A.E. Barzakh, É.I. Berlovich, V.P. Denisov, A.G. Dernyatin, V.S. Ivanov, A.N. Zherikhin, O.N. Kompanets, V.S. Letokhov, V.I. Mishin, and V.N. Fedoseev.
High-resolution laser photoionization spectroscopy of radioactive europium isotopes.
Sov. Phys. JETP, 59(4):729–736, 1984.

[ABD+84] G.D. Alkhazov, A.E. Barzakh, V.P. Denisov, A.G. Dernyatin, V.S. Ivanov, A.N. Zherikhin, O.N. Kompanets, V.S. Letokhov, V.I. Mishin, and V.N. Fedoseev.
Atomic lines isotope shifts of short-lived radioactive Eu studied by high-sensitive laser resonance photoionizatoin method in "on-line" experiments with proton beams.
Optics Communications, 52(1):24–28, 1984.

[AKL71] R.V. Ambartsumyan, V.N. Kalinin, and V.S. Letokhov.
Two-step selective photoionizatoin of rubidium atoms by laser radiation.
JETP Letters, 13:217–219, March 1971.

[AN99] S.A. Ahmad and S.G. Nakhate.
Multiphoton and Multistep Laser Ionization Spectroscopy of Atoms.
Springer-Verlag, 1999.
doi:10.1007/978-1-4615-4259-9.

[BDRR03] S. Bhattacharyya, R. D'Souza, Pushpa M. Rao, and M.A.N. Razvi.
Investigation of new odd-parity autoionization Rydberg levels of neutral europium.
Spectrochimica Acta Part B: Atomic Spectroscopy, 58(3):469 – 478, 2003.
doi:http://dx.doi.org/10.1016/S0584-8547(03)00003-X.

[BFI+04] A. E. Barzakh, D. V. Fedorov, A. M. Ionan, V. S. Ivanov, F. V. Moroz, K. A. Mezilev, S. Yu. Orlov, V. N. Panteleev, and Yu M. Volkov.
Changes in the mean square charge radii of neutron-deficient europium isotopes measured by the laser ion source resonance ionization spectroscopy.

The European Physical Journal A - Hadrons and Nuclei, 22(1):69–74, 2004.
doi:10.1140/epja/i2003-10231-y.

[BNN88] W Borchers, W Neu, and R Neugart.
Status report and request for beam time: study of nuclear moments and mean square charge radil by collinear fast-beam laser spectroscopy.
Technical Report CERN-PSCC-88-3. PSCC-P-110, CERN, Geneva, 1988.
URL: http://cds.cern.ch/record/297879.

[CL88] J P Connerade and A M Lane.
Interacting resonances in atomic spectroscopy.
Reports on Progress in Physics, 51(11):1439, 1988.
URL: http://stacks.iop.org/0034-4885/51/i=11/a=002.

[Con98] Jean-Patrick Connerade.
Highly Excited Atoms.
Cambridge University Press, 1998.
Cambridge Books Online.
URL: http://dx.doi.org/10.1017/CBO9780511524516.

[Dem05] W. Demtröder.
Experimentalphysik 3: Atome, Moleküle und Festkörper.
Springer-Verlag, 3. edition, 2005.

[Dem07] W. Demtröder.
Laserspektroskopie: Grundlagen und Techniken.
Springer-Verlag, 5. edition, 2007.

[DM16] Cinzia De Melis.
The CERN accelerator complex. Complexe des accélérateurs du CERN.
Jul 2016.
General Photo.
URL: https://cds.cern.ch/record/2197559.

[Dre68] M. J. Dresser.
The Saha-Langmuir Equation and its Application.
Journal of Applied Physics, 39(1):338–339, 1968.
URL: http://dx.doi.org/10.1063/1.1655755.

[D.S20] Megh Nad Saha D.Sc.
LIII. Ionization in the solar chromosphere.
Philosophical Magazine Series 6, 40(238):472–488, 1920.
doi:10.1080/14786441008636148.

[DS91] G. W. F. Drake and R. A. Swainson.
Quantum defects and the 1/ n dependence of Rydberg energies: Second-order polarization effects.
Phys. Rev. A, 44:5448–5459, Nov 1991.
doi:10.1103/PhysRevA.44.5448.

[Egg19] J. Eggert.
Über den Dissozitaionszustand der Fixsterngase.
Physikalische Zeitschriften, 20:570–574, May 1919.

[Fan61] U. Fano.
Effects of Configuration Interaction on Intensities and Phase Shifts.
Phys. Rev., 124:1866–1878, Dec 1961.
doi:10.1103/PhysRev.124.1866.

[FRB+15] D.A. Fink, S.D. Richter, K. Blaum, R. Catherall, B. Crepieux, V.N. Fedosseev, A. Gottberg, T. Kron, B.A. Marsh, C. Mattolat, S. Raeder, R.E. Rossel, S. Rothe, F. Schwellnus, M.D. Seliverstov, M. Sjödin, T. Stora, P. Suominen, and K.D.A. Wendt.
On-line implementation and first operation of the Laser Ion Source and Trap at ISOLDE/CERN .
Nuclear Instruments and Methods in Physics Research Section B: Beam Interactions with Materials and Atoms, 344:83 – 95, 2015.
URL: http://dx.doi.org/10.1016/j.nimb.2014.12.007.

[FTD76] U. Fano, C. E. Theodosiou, and J. L. Dehmer.
Electron-optical properties of atomic fields.
Rev. Mod. Phys., 48:49–68, Jan 1976.
URL: http://link.aps.org/doi/10.1103/RevModPhys.48.49, doi:10.1103/RevModPhys.48.49.

[FY84] V.N. Fedoseev and A.K. Yusupov.
Effect of polarization of laser emission on the multistage photoionization yield of ytterbium isotopes.
Optics and Spectroscopy, 57:552–554, 1984.

[GBC+16] T. Day Goodacre, J. Billowes, R. Catherall, T.E. Cocolios, B. Crepieux, D.V. Fedorov, V.N. Fedosseev, L.P. Gaffney, T. Giles, A. Gottberg, K.M. Lynch, B.A. Marsh, T.M. Mendonça, J.P. Ramos, R.E. Rossel, S. Rothe, S. Sels, C. Sotty, T. Stora, C. Van Beveren, and M. Veinhard.
Blurring the boundaries between ion sources: The application of the RILIS inside a FEBIAD type ion source at ISOLDE.
Nuclear Instruments and Methods in Physics Research Section B: Beam Interactions with Materials and Atoms, 376:39 – 45, 2016.
Proceedings of the XVIIth International Conference on Electromagnetic Isotope Separators and Related Topics (EMIS2015), Grand Rapids, MI, U.S.A., 11-15 May 2015.
URL: http://dx.doi.org/10.1016/j.nimb.2016.03.005.

[GBD+14] L. Gastaldo, K. Blaum, A. Doerr, Ch. E. Düllmann, K. Eberhardt, S. Eliseev, C. Enss, Amand Faessler, A. Fleischmann, S. Kempf, M. Krivoruchenko, S. Lahiri, M. Maiti, Yu. N. Novikov, P. C.-O. Ranitzsch, F. Simkovic, Z. Szusc, and M. Wegner.
The Electron Capture ^{163}Ho Experiment ECHo.

Journal of Low Temperature Physics, 176(5):876–884, 2014.
doi:10.1007/s10909-014-1187-4.

[iso] http://isolde.web.cern.ch/isolde-logos-layouts-and-templates# downloaded on the 28.07.2016.

[J.-92] J.-P. Connerade.
The benefits of high resolution spectroscopy in the VUV.
J. Phys. II France, 2(4):757–772, 1992.
doi:10.1051/jp2:1992164.

[KL23] K. H. Kingdon and Irving Langmuir.
The Removal of Thorium from the Surface of a Thoriated Tungsten Filament by Positive Ion Bombardment.
Phys. Rev., 22:148–160, Aug 1923.
doi:10.1103/PhysRev.22.148.

[Klu86] H.-J. Kluge.
Isolde user's guide.
CERN, Genève, Switzerland, 1986.

[KR99] U Köster and H L Ravn.
Yields and spectroscopy of radioactive isotopes at LOHENGRIN and ISOLDE. Ausbeuten und Spektroskopie radioaktiver Isotope bei LOHENGRIN und ISOLDE.
PhD thesis, Munich, Tech. U., Geneva, 1999.
Presented on 30 Dec 1999.
URL: https://cds.cern.ch/record/494272.

[Kro11] Tobias Kron.
Konzeption, Aufbau und Test einer Referenzzelle für die resonante Laserionisation.
Diploma thesis, Johannes Gutenberg-Universität Mainz, 2011.

[KS48] Robert Karplus and Julian Schwinger.
A Note on Saturation in Microwave Spectroscopy.
Phys. Rev., 73:1020–1026, May 1948.
doi:10.1103/PhysRev.73.1020.

[kur] Kurucz Database.
URL: http://www.pmp.uni-hannover.de/cgi-bin/ssi/test/kurucz/sekur.html.

[KYRa15] A. Kramida, Yu. Ralchenko, J. Reader, and and NIST ASD Team.
NIST Atomic Spectra Database (ver. 5.3), [Online]. Available: http://physics.nist.gov/asd [2016, August 5]. National Institute of Standards and Technology, Gaithersburg, MD., 2015.

[Leo94] William R. Leo.
Techniques for Nuclear and Particle Physics Experiments.
Springer-Verlag, 2. edition, 1994.

[Let87] V.S. Letokhov.
Laser Photionization Spectroscopy.
Acadamic Press, Inc., 1. edition, 1987.

[LMS+92] V S Letokhov, V I Mishin, S K Sekatsky, V N Fedoseyev, G D Alkhazov, A E Barzakh, V P Denisov, and V E Starodubsky.
Laser spectroscopic studies of nuclei with neutron number N<82 (Eu, Sm and Nd isotopes).
Journal of Physics G: Nuclear and Particle Physics, 18(7):1177, 1992.
URL: http://stacks.iop.org/0954-3899/18/i=7/a=008.

[log] Logbook entry ISOLDE GPS 25.05.2015.
URL: http://ab-dep-op-elogbook.web.cern.ch/ab-dep-op-elogbook/elogbook/eLogbook.php?lgbk=110&date=20150525&shift=1.

[LTG+12] B. Lauritzen, N. Timoney, N. Gisin, M. Afzelius, H. de Riedmatten, Y. Sun, R. M. Macfarlane, and R. L. Cone.
Spectroscopic investigations of Eu^{3+}:Y_2SiO_5 for quantum memory applications.
Phys. Rev. B, 85:115111, Mar 2012.
URL: http://link.aps.org/doi/10.1103/PhysRevB.85.115111, doi:10.1103/PhysRevB.85.115111.

[MAA+13] B.A. Marsh, B. Andel, A.N. Andreyev, S. Antalic, D. Atanasov, A.E. Barzakh, B. Bastin, Ch. Borgmann, L. Capponi, T.E. Cocolios, T. Day Goodacre, M. Dehairs, X. Derkx, H. De Witte, D.V. Fedorov, V.N. Fedosseev, G.J. Focker, D.A. Fink, K.T. Flanagan, S. Franchoo, L. Ghys, M. Huyse, N. Imai, Z. Kalaninova, U. Köster, S. Kreim, N. Kesteloot, Yu. Kudryavtsev, J. Lane, N. Lecesne, V. Liberati, D. Lunney, K.M. Lynch, V. Manea, P.L. Molkanov, T. Nicol, D. Pauwels, L. Popescu, D. Radulov, E. Rapisarda, M. Rosenbusch, R.E. Rossel, S. Rothe, L. Schweikhard, M.D. Seliverstov, S. Sels, A.M. Sjödin, V. Truesdale, C. Van Beveren, P. Van Duppen, K. Wendt, F. Wienholtz, R.N. Wolf, and S.G. Zemlyanoy.
New developments of the in-source spectroscopy method at RILIS/ISOLDE.
Nuclear Instruments and Methods in Physics Research Section B: Beam Interactions with Materials and Atoms, 317, Part B:550 – 556, 2013.
{XVIth} International Conference on ElectroMagnetic Isotope Separators and Techniques Related to their Applications, December 2–7, 2012 at Matsue, Japan .
doi:10.1016/j.nimb.2013.07.070.

[Mar13] B.A. Marsh.
Resonance Ionisation Laser Ion Sources.
pages 203–263, 2013.
contribution to the CAS-CERN Accelerator School: Ion Sources, Senec, Slovakia, 29 May - 8 June 2012, edited by R. Bailey.

doi:10.5170/CERN-2013-007.203.

[MBF07] Bruce Marsh, Jonathan Billowes, and Valentin Feddosseev.
In-Source Laser Resonance Ionization at ISOL Facilities.
PhD thesis, Manchester U., Feb 2007.
Presented 14 Mar 2007.
URL: https://cds.cern.ch/record/1519194.

[MBF+10] B. A. Marsh, L.-E. Berg, D. V. Fedorov, V. N. Fedosseev, O. J. Launila, M. Lindroos, R. Losito, F. K. Österdahl, T. Pauchard, I. T. Pohjalainen, U. Sassenberg, M. D. Seliverstov, A. M. Sjödin, and G. Tranströmer.
The ISOLDE RILIS pump laser upgrade and the LARIS Laboratory.
Hyperfine Interactions, 196(1):129–141, 2010.
doi:10.1007/s10751-010-0168-5.

[Mes10] D. Meschede.
Gerthsen Physik.
Springer-Verlag, 24. edition, 2010.

[MMM09] V. I. Mishin, A. L. Malinovsky, and D. V. Mishin.
Resonant Ionization Laser Ion Source (RILIS) With Improved Selectivity Achieved By Ion Pulse Compression Using In-Source-Time-of-Flight Technique.
AIP Conference Proceedings, 1104(1):207–212, 2009.
URL: http://dx.doi.org/10.1063/1.3115604.

[Nau14] Pascal Naubereit.
Weiterentwicklung eines weitabstimmbaren Titan:Saphir-Lasers und sein Einsatz zur Spektroskopie hochliegender Resonanzen in Holmium, 2014.

[Neu85] R. Neugart.
Collinear laser spectroscopy on unstable isotopes—a tool of nuclear physics.
Hyperfine Interactions, 24(1):159–180, 1985.
doi:10.1007/BF02354810.

[NRBA96] S G Nakhate, M A N Razvi, G L Bhale, and S A Ahmad.
New odd-parity high-lying energy levels of the europium atom by resonance ionization spectroscopy.
Journal of Physics B: Atomic, Molecular and Optical Physics, 29(8):1439, 1996.

[NRCA00] S.G. Nakhate, M.A.N. Razvi, J.P. Connerade, and S.A. Ahmad.
Investigation of Rydberg states of the europium atom using resonance ionization spectroscopy.
Journal of Physics B: Atomic, Molecular and Optical Physics, 33(22):5191, 2000.
URL: http://stacks.iop.org/0953-4075/33/i=22/a=319, doi:10.1088/0953-4075/33/22/319.

[Ott89] Ernst W. Otten.

Nuclear Radii and Moments of Unstable Isotopes, pages 517–638. Springer US, Boston, MA, 1989. doi:10.1007/978-1-4613-0713-6_7.

[Rae10] Sebastian Raeder. Spurenanalyse von Aktiniden in der Umwelt mittels Resonanzoinisations-Massenspektrometrie, 2010.

[RDH+13] Sebastian Raeder, Marik Dombsky, Henning Heggen, Jens Lassen, Thomas Quenzel, Marica Sjödin, Andrea Teigelhöfer, and Klaus Wendt. In-source laser spectroscopy developments at trilis—towards spectroscopy on actinium and scandium. *Hyperfine Interactions*, 216(1):33–39, 2013. doi:10.1007/s10751-013-0832-7.

[RGF+16] S. Rothe, T. Day Goodacre, D.V. Fedorov, V.N. Fedosseev, B.A. Marsh, P.L. Molkanov, R.E. Rossel, M.D. Seliverstov, M. Veinhard, and K.D.A. Wendt. Laser ion beam production at CERN-ISOLDE: New features – More possibilities. *Nuclear Instruments and Methods in Physics Research Section B: Beam Interactions with Materials and Atoms*, 376:91 – 96, 2016. Proceedings of the {XVIIth} International Conference on Electromagnetic Isotope Separators and Related Topics (EMIS2015), Grand Rapids, MI, U.S.A., 11-15 May 2015. doi:10.1016/j.nimb.2016.02.024.

[Rit03] Walter Ritz. Zur Theorie der Serienspektren. *Annalen der Physik*, 317(10):264–310, 1903. doi:10.1002/andp.19033171003.

[RMK+12] M. Reponen, I. D. Moore, T. Kessler, I. Pohjalainen, S. Rothe, and V. Sonnenschein. Laser developments and resonance ionization spectroscopy at IGISOL. *The European Physical Journal A*, 48(4):1–15, 2012. doi:10.1140/epja/i2012-12045-2.

[Rot11] S. Rothe. Improvement of the precision and efficiency of the ISOLDE laser ion source RILIS. Technical Report CERN-EDMS-1721870 v.1, CERN, Geneva, March 2011. URL: https://edms.cern.ch/document/1721870/1.

[RRWR11] Ralf Erik Rossel, D Richter, K Wendt, and S Rothe. *Programming of the Wavelength Stabilization for a Titanium:Sapphire Laser using LabVIEW and Implementation into the CERN ISOLDE RILIS Measurement System*. PhD thesis, Mainz U., Dec 2011.

Presented 15 Feb 2012.
URL: https://cds.cern.ch/record/1523721.

[RS95] K.J. Ross and B. Sonntag.
High temperature metal atom beam sources.
Rev. Sci. Instrum., 66(9):4409–4433, 1995.
doi:10.1063/1.1145337.

[RWN12] Sebastian Rothe, K D A Wendt, and W Nörtershäuser.
An all-solid state laser system for the laser ion source RILIS and in-source laser spectroscopy of astatine at ISOLDE, CERN.
PhD thesis, Mainz U., 2012.
Presented 24 Sep 2012.
URL: http://cds.cern.ch/record/1519189.

[SAB+15] T. K. Sato, M. Asai, A. Borschevsky, T. Stora, N. Sato, Y. Kaneya, K. Tsukada, Ch. E. Dullmann, K. Eberhardt, E. Eliav, S. Ichikawa, U. Kaldor, J. V. Kratz, S. Miyashita, Y. Nagame, K. Ooe, A. Osa, D. Renisch, J. Runke, M. Schadel, P. Thorle-Pospiech, A. Toyoshima, and N. and Trautmann.
Measurement of the first ionization potential of lawrencium, element 103.
Nature, 520:209–211, 2015.
doi:10.1038/nature14342.

[Sch16] Fabian Schneider.
First Steps of the ECHo Experiment: Penning Trap Mass Measurements of the ^{163}Ho Electron Capture process and Implantation of ultrapure Ho into Microcalorimeter Arrays.
Phd thesis, Johannes Gutenberg-Universität Mainz, 2016.

[Sea66] M J Seaton.
Quantum defect theory II. Illustrative one-channel and two-channel problems.
Proceedings of the Physical Society, 88(4):815, 1966.
URL: http://stacks.iop.org/0370-1328/88/i=4/a=303.

[SFK+92] F. Scheerer, V.N. Fedoseyev, H.-J. Kluge, V.I. Mishin, V.S. Lethokov, H.L. Ravn, Y. Shirakabe, S. Sundell, and O. Tengblad.
A chemically selective laser ion source for on-line mass separation.
Review of Scientific Instruments, 63(4):2831–2833, 1992.
URL: http://dx.doi.org/10.1063/1.1142820.

[SKZ+16] D. Serrano, J. Karlsson, L. Zheng, Y. Dong, A. Ferrier, P. Goldner, A. Walther, L. Rippe, and S. Kröll.
Satellite line mapping in Eu^{3+}–Ce^{3+} and Pr^{3+}–Ce^{3+} codoped Y_2SiO_5.
Journal of Luminescence, 170, Part 1:102 – 107, 2016.
URL: http://www.sciencedirect.com/science/article/pii/S0022231315005530.

[ST75] G. Smith and F. S. Tomkins.

Autoionization Resonances in the Eu I Absorption Spectrum and a New Determination of the Ionization Potential.
Proceedings of the Royal Society of London A: Mathematical, Physical and Engineering Sciences, 342(1628):149–156, 1975.
doi:10.1098/rspa.1975.0017.

[ST76] G. Smith and F. S. Tomkins.
The absorption spectrum of europium.
Philosophical Transactions of the Royal Society of London A: Mathematical, Physical and Engineering Sciences, 283(1313):345–365, 1976.
doi:10.1098/rsta.1976.0089.

[ST07] B.E.A. Saleh and M.C. Teich.
Fundamentals of photonics.
Wiley, 2. edition, 2007.

[ZLMF87] A.D. Zyuzikov, V.S. Letokhov, V.I. Mishin, and V.N. Fedoseev.
Laser resonance photoionization spectrocopy of excited and autoionization atomic states of rare-earth elements. 1: Europium.
Opt. Spektrosk., 63:973–982, 1987.

Acknowledgments

I would like to thank my reviewers Klaus Wendt and Valentin Fedosseev for their support and time during this project and for making my stay at CERN possible. I hope this is not the last thesis of mine you'll get to read.
I greatly enjoyed my stay at CERN, mostly because of the superb RILIS team. Many great working hours passed with me barley taking notice as well as evenings with 'cultural' events, that I wouldn't want to miss! I hope we will continue like this in the months (or years) to come (at least if don't all die in a paragliding accident). I would like to thank my two supervisors, Bruce Marsh and Sebastian Rothe, for their continuous help and their constructive suggestions during my time here. I'd also like to thank Tom Day Goodacre for being supportive in the lab as well as in the office, answering the many questions I've been pestering him with.

Thanks also go to my (old) group LARISSA in Mainz. Thanks for all the nice company, support and discussions (and for letting me play Kicker during my visit, although I really suck at it). I'd like to specially thank Tobias Kron, who was always supportive and open for questions. I'd also like to thank Dominik Studer for being a great help with the Rydberg data analysis and making my life a bit easier in that regard.

Ich bin alleine groß, aber...: Ich möchte an dieser Stelle natürlich auch meiner Familie, insbesondere meinen Eltern, danken. Vielen Dank für die jahrelange Unterstützung und all das, was ihr mir ermöglicht habt. Ohne euch wäre ich sicherlich nicht hier. Und, auch wenn ich ja jetzt schon ein bisschen auf eigenen Beinen stand, es gibt nichts besseres, als in verzweifelten Situationen zu Hause anzurufen und gesagt zu bekommen, dass alles ok wird. Danke auch an Niko und Philipp und die vielen, vielen Diskussionen (nicht Streitereien, wie ja manche sagen), die sicherlich dazu beigetragen haben, dass ich hier sehr gut zurecht kam.
Der letzte Dank geht an Paul. Du hast die beste Zeit ausgesucht, um hier zu sein. Du bist der beste Diskussionspartner, Aufmunterer und auch Koch und Einkäufer, den man sich wünschen kann. Ohne dich wären die letzten Monate sicherlich um einiges anstrengender geworden.

"Του μέλλοντος η μέρες στέκοντ' εμπροστά μας
σα μια σειρά κεράκια αναμένα —
χρυσά, ζεστά, και ζωηρά κεράκια. [...]"

by K.P. Kavafis